UNIVERSITÀ DEGLI STUDI DI PADOVA

Dipartimento di Fisica e Astronomia "Galileo Galilei"

Master Degree in Astrophysics and Cosmology

Final Dissertation

Investigation and Analysis of the Ingot Wavefront Sensor Response to Varying Na-LGS profiles

Supervisor:

Prof. Roberto Ragazzoni

Co-Supervisor:

Dr. Maria Bergomi

Tania Sofia Gomes Machado

Candidate:

Dheeraj Malik

Academic Year 2023-2024

To my Family,
And my boy Viraj.

Acknowledgments

I would like to express my deepest gratitude to Prof. Roberto Ragazzoni for providing me with the incredible opportunity to work on this project. I am thankful for giving his time to review the work during meetings and providing with the scope of improvement.

My heartfelt thanks go to my co-supervisors, Maria and Tania, whose expertise and guidance have been invaluable in shaping this work. Their unwavering support, both in the lab and beyond, has encouraged me to persevere through difficulties and stay focused on my work. Their thorough insights have helped improve the quality of the work to a great extent.

I am especially grateful to Elisa for her ideas, reviews and suggestions regarding various sections of this work.
A special thanks to Kalyan, Simone, Davide, Alessandro, Federico, Carmelo, and Demetrio for going above and beyond to help me. Their suggestions and valuable input during meetings have been critical in approaching the tests performed in the lab and analysis of data.

I would also acknowledge my family, everyone from Viraj to Roshni Devi, this would not be possible without your support. The motivation you all have given me to achieve my goals is beyond words. Special thanks to Fra for being by my side during all the highs and lows and extending full support always.

A big thanks to my colleagues and friends who kept me high on energy. I appreciate all our shared experiences during the last two years.

Finally, I extend my appreciation to all those who, in one way or another, contributed to the success of this project. Your support has made this achievement possible.

Abstract

The upcoming extremely large aperture telescopes like the Extremely Large Telescope (ELT) will have Adaptive Optics (AO) systems that use Sodium Laser Guide Stars (Na-LGSs) along with Natural Guide Stars (NGS) to correct for the atmospheric distortions and allow a high sky coverage. Na-LGSs are extended sources due to the thickness of sodium layer in the atmosphere. Moreover, on such large aperture telescopes, the image of the Na-LGS appears elongated, specially on the subapertures farther away from the laser launcher. To utilize the entire 3D volume of Na-LGS, a novel idea of Wavefront Sensor (WFS), called Ingot-Wavefront Sensor (I-WFS), was proposed by Roberto Ragazzoni. The idea has been realised as a roof-shaped extended prism by the AO group at INAF-OAPd, where currently a test bench simulating ELT characteristics has been setup to test the I-WFS performance.

My work on I-WFS focused on introducing on the test bench, testing and characterizing a new OLED screen, which is used to reproduce the Na-LGS variability using the sodium density profile collected using LIDAR. The work also focuses on characterizing and optimizing the I-WFS response to varying Na-profiles and conditions.

Keywords:

Adaptive Optics, Wavefront Sensor, Laser Guide Star, Extremely Large Telescope

Contents

Acronyms

2D Two Dimensions.

3D Three Dimensions.

AO Adaptive optics.

CCD Charge-Coupled Device.

DL Deformable Lens.

DM Deformable Mirror.

dof Degrees of freedom.

ELT Extremely Large Telescope.

ELTs Extremely large telescopes.

ESO European Southern Observatory.

NIR Near Infrared

FoV Field of View.

FWHM Full Width at Half Maximum.

INAF-OAPd Istituto Nazionale di Astrofisica-Osservatorio Astronomico di Padova

ORCAS Orbiting Configurable Artificial Star

GLAO Ground Layer Adaptive Optics.

VLT Very Large Telescope

NA-LGS Sodium Laser Guide Star

HST Hubble Space Telescope.

IR Infrared.

I-WFS Ingot Wavefront Sensor.

LGS Laser Guide Star.

LIDAR Laser Imaging Detection and Ranging.

LLT Laser Launcher Telescope.

LTAO Laser Tomography Adaptive Optics.

MCAO Multi-Conjugated Adaptive Optics.

NGS Natural Guide Star.

NIR Near-Infrared.

OLED Organic Light-Emitting Diode.

PSF Point Spread Function.

P-WFS Pyramid Wavefront Sensor.

RTC Real Time Computer.

SCAO Single Conjugated Adaptive Optics.

SCIDAR SCIntillation Detection And Ranging.

SH-WFS Shack-Hartmann Wavefront Sensor.

SNR Signal-to-Noise Ratio.

SR Strehl Ratio.

UV Ultraviolet.

WFS Wavefront Sensor.

XAO eXtreme Adaptive Optics.

1 Introduction

> "Over and over in the history of astronomy, a new instrument finds things we never expected to see."
>
> — Rainer Weiss

It is often said that necessity is the mother of all inventions, but in the field of astronomy, curiosity serves as the faithful driving force. Many of us have childhood memories of gazing up at the night sky, our minds brimming with endless questions about the stars and the Moon. Some individuals took these questions seriously and dedicated their lives to uncovering the answers to their curiosities. In this process, they developed tools that have laid the foundation of our understanding of astronomy. One of these tools, which stands out as one of the most significant, is a telescope.

It was in 1611, a Greek mathematician named Giovanni Demisiani coined the term 'telescope', with two words 'tele' meaning 'far' and 'skopein' meaning 'to look'. Prior to this incident, the first telescope was developed by Galileo Galilei by improving on the design by Hans Lippershey. It was a very simple reflecting telescope, which provided a resolution of about 10 - 15 arcsec[1]. With this limited resolving power, he made detailed observations of the phases of Venus, the valleys and mountains of the Moon, the four largest Jovian satellites[2] and drawing of sun with sunspots[3].

Another significant advancement in telescope technology occurred when Isaac Newton developed the reflecting telescope[4]. Over the next two centuries, many notable people such as James Gilbert Baker, Sir William Herschel, William Parsons, and others contributed greatly to improving the capabilities of telescope. During this period, substantial developments were also made in the materials and technologies used in telescope components. For example, borosilicate glass, commonly known as Pyrex, was utilized in the 60-inch Astrometric Reflector of the U.S. Naval Observatory [5]. Other important advancements in technologies included the development of cameras for observatories to capture images of celestial objects and the introduction of spectrographs to analyze their light[6]. These instruments have certainly improved the capabilities of telescopes, but only up to a certain point. Beyond this, the Earth's atmosphere interferes with the light wavefronts coming from celestial objects, limiting the effectiveness of these improvements and pushed scientists to find some innovative way to counter the effects of the atmosphere on wavefront. Dr. Horace Babcock came up with a solution that is called Adaptive Optics

(AO).

At the Mount Wilson Observatory, Babcock was working on several topics including the photoelectric guider for telescope[7], the turbulence in atmosphere and the effect of atmosphere on the wavelength of the light[8]. With his detailed studies and in the quest to find solution to the atmospheric distortion, he published his design of an AO system that was composed of a seeing sensor and a wavefront corrector[9].

The advancement in AO systems uncovered major limitations like the lack of sufficiently bright reference stars or NGS near the targets under observation and efficient deformable mirrors. This lack of nearby NGS hindered the effectiveness of AO in correcting atmospheric distortions in star-poor regions of sky and achieving optimal imaging quality for many celestial objects. It was not until the first laser light was operated in 1960 by Theodore Maiman at Hughes Research Laboratory[10], that astronomers saw another ray of hope to enhance the technology in AO for the regions with absence of NGS. Even after the invention, it took more than 2 decades to use this technology at the telescope facilities. Its use in the astronomical field has helped mature the AO technology to a greater extent and this in-turn has helped different fields within astronomy to reach better detailing and precision.

Laser is used to create Laser Guide Star (LGS) to reduce the impact of atmospheric seeing[11]. This idea of integrating a laser with the telescope was first given by Linnik [12], it was only in recent decades that astronomers have integrated lasers on the telescopes. For example, ESO installed its first laser guide star on the telescope 4 of Very Large Telescope (VLT) Unit in 2013[13]. The LGS provided with a much higher sky coverage and probability of correction on the astronomical targets at optical and Near Infrared (NIR) wavelengths. The improved AO with laser has become an important part of almost all the observatories that host a 4m or larger class of telescope.
There are two main types of LGS: Rayleigh Scattering and Sodium. Around late 20^{th} century, the Rayleigh Scattering LGS has been the most commonly used, but its effectiveness is limited due to its lower altitude. Since early 21^{st} century, Sodium (Na) LGS has been preferred over Rayleigh LGS, although it presents its own challenges. First, Na-LGS are extended sources because of the thickness of sodium layer in the atmosphere, and second, their brightness varies along their length over time, complicating their use as refernece sources. This poses a significant problem for upcoming large telescopes, such as the Extremely Large Telescope (ELT) with its 39-meter aperture. The elongation of Na-LGS, when a laser is launched from the side, is not negligible with such a large aperture, and the small focal depth of currently used WFS compared to the length of Na-LGS leads to defocused astronomical images.[14]. As a result, astronomers worldwide are working to fully harness these extended sources to improve the correction for atmospheric distortions and achieve high Strehl Ratios.

In this thesis, we will focus on a new class of WFS that is a tailor-made solution for the elongated LGS. The novel idea of the innovative WFS, called Ingot Wavefront Sensor (I-WFS), was put forth by [15], to further optimize the performance of AO on the next generation of extremely large telescopes. In its current design, it is a 3-Dimensional extended prism design which is similar to the elongated shape of the LGS. The I-WFS is

currently under testing at a bench located at INAF-OAPd.

The work discussed in this thesis is based on the tests performed to improve the Ingot test bench and its automated scripts, used to operate different components on Ingot bench, in order to provide a solid validation for the I-WFS into realistic conditions, focusing in particular in its response to the NaLGS variability.

In chapter 2, we will discuss in detail about the atmospheric distortion and the different parameters that affect the imaging of the telescopes despite huge diameter size and advance in technologies. We will discuss about the adaptive optics as a solution against the effects of atmosphere on astronomy. We will also discuss about the different components that make up the AO system.

In chapter 3, we will discuss about various wavefront sensors that are actively being used at various telescope facilities and we will compare these actively used WFS with the I-WFS to better understand the capabilities and advantages of this innovative tool.

In chapter 4, we will talk about the ELT and its main first-light instruments. We will mainly focus on the Multi-Conjugate Adaptive Optics (MCAO) unit of the telescope called Multiconjugate Adaptive Optics Relay for ELT Observation (MORFEO). Following this, we will also go through the key science cases for the major areas of astronomy on which the ELT will focus. Finally, we will also understand the need for LGSs in astronomy with the help of some simulation results and discuss about the advantages of having an I-WFS on the ELT.

Finally, in chapter 5, we will present in detail the Ingot test bench. We will discuss about the alignment and calibration procedures, including the parameters to be satisfied for alignment of the I-WFS with respect to the simulated LGS source. We will talk about the various tests conducted for a thorough comparison between the OLED screens used on the Ingot test bench to replicate the Na-LGS. We will also see how the defined procedures perform in order to keep the I-WFS aligned to the Na-LGS source during movements of the source. This chapter will also cover the process of simulating the time varying Na-LGS on the OLED screen and investigate the results of alignment of I-WFS with different Na profiles. Finally, we will assess the sensitivity of the I-WFS to small changes in the intensity of Na profiles. Through these tests, we will infer key characteristics and properties of the I-WFS and the Ingot test bench. We will conclude the chapter with the foreseen upgrades and next steps in the consolidation of the I-WFS.

2 Adaptive Optics

"A man that looks on glass,
On it may stay his eye;
Or if he pleaseth, through it pass,
And then the heaven espy. "

— George Herbert

In this chapter we will have a detailed introduction on atmosphere and how atmospheric properties like absorption, dispersion and turbulence, limit our ability to use the huge Earth based telescope to their full potential. We will then explore AO as a solution to these limitations. A significant portion of this discussion will focus on the components of AO and their limitations. Specifically, we will examine the reference sources used in AO, highlighting their advantages and drawbacks, especially in the context of future large telescopes. We will also review the most commonly used AO techniques, discussing the scenarios in which each technique is most effective.

2.1 Diffraction and Airy Disk

During the observation of a target in the sky, we see it because its light wavefront reaches our telescope. As the wavefront passes through the aperture of the telescope, it is focused onto detectors positioned at the focal plane, enabling us to capture the image of the target object.
In the absence of atmospheric interference, geometrically, one expect the image of a point source to appear as a point when seen through a telescope but this is not the case in reality. When the wavefront from a distant point source, such as a star, travels through space and reaches the telescope, it is a smooth, undisturbed and planar wavefront as shown in fig.2.1(a). As this wavefront encounters the aperture of the telescope, it acts as an obstacle to the wavefront. This interaction of the wavefront with the aperture disrupts the wavefront, resulting in a diffraction pattern on the focal plane, instead of a sharp point. This is explained according to Huygens' principle, which states that each point on this wavefront acts as a source of secondary wavelets that spread out and interfere with each other.
This enlargement of the point source image can be further understood with the Heisenberg's uncertainty principle. According to the principle, when the wavefront passes through the aperture of the telescope, it introduces an uncertainty in the direction of motion of photons within the wavefront. The observed image typically consists of a bright central spot surrounded by concentric rings with alternative bright and dark cir-

cles. This pattern is known as the Airy pattern, as shown in fig.2.1(b), named after the distinguished astronomer and mathematician George B. Airy, who first provided its mathematical description in 1835[16]. The radius of the bright central spot is given by:

$$\theta_{\text{Airy}} = 1.22\frac{\lambda}{D} \tag{2.1}$$

where:

- λ represents the wavelength of the light, and
- D represents the diameter of the telescope.

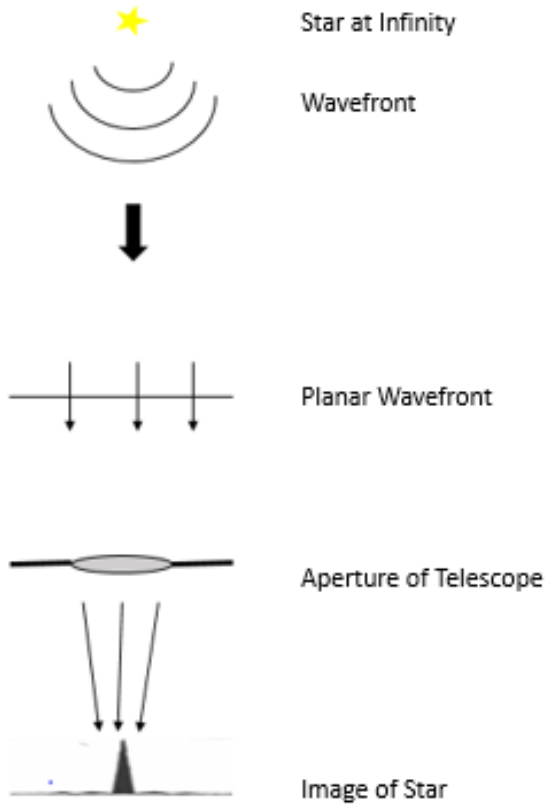

((a)) ((b))

Figure 2.1: The fig 2.1(a) shows a wavefront from a star, considered as a point source, at infinity reaching the aperture of the telescope in absence of atmosphere. The wavefront is focused on detector producing an image of the point source. This image is seen as an airy disk on the detector. Fig.2.1(b) shows the airy disk produced by a point source. The airy disk image is taken from [17].

The phenomenon, diffraction, is inherent to the wave nature of light and limits the ability of the telescope to resolve the point source as a true point. A telescope limited by diffraction is called diffraction limited. The equation 2.1 gives the resolution of a diffraction limited telescope, it means two sources are said to be resolved by a diffraction limited

telescope if the central peak of airy disk by the second source lies at the first minimum of the airy disk by first source or the separation between the two peaks is equal to θ_{Airy} given by the telescope.

In real world conditions, telescope aperture is not the only obstacle for the wavefront. Atmosphere also plays a crucial role. Starting right from the edge of the atmosphere until the wavefront reaches the telescope, it faces several changes in direction due to changes in refractive index of media and turbulence at different altitudes and that is why aberrations are introduced on the wavefront. It is important to understand the effects of atmosphere on the electromagnetic radiation before trying to figure out the solutions. In the next section we will understand how distortions are introduced to the wavefront by the atmosphere of the Earth.

2.2 Atmosphere and Astronomy

The atmosphere is composed of various atoms, gas molecules, and dust particles that are essential for sustaining life on Earth and providing the necessary conditions for millions of organisms to thrive. For astronomers and to astronomical observations, the atmosphere stands as a huge challenge. The same components that make the atmosphere vital for life such as oxygen, nitrogen, and water vapor, are also cause of three major characteristics which distort and diminish the clarity of images captured by ground based telescopes. These three characteristics are:

1. **Scattering:** During the day and on moonlit nights, scattered sunlight is the main source of sky radiation, making it difficult to observe faint celestial objects. The airglow on moonless nights makes for most of the atmospheric radiation between 0.5 µm and 2.5 µm, which is caused by emissions from hydroxyl (OH) molecules in the upper atmosphere. The presence of this background radiation sets a practical limit for us to detect faint objects from Earth's surface, as it introduces a lot of noise that competes with the weak signals from distant celestial sources[1].

2. **Absorption:** The composition of atmosphere makes it really hard to understand the interactions of atoms and molecules. All these atoms and molecules have specific wavelengths that they can absorb but sometimes it occurs at broader range of wavelengths due to higher degrees of freedom like rotational and vibrational. This absorption makes the atmosphere opaque to certain wavelengths and transparent to others across the whole spectrum, as shown in fig.2.2.

3. **Turbulence:** As the Earth revolves around the Sun, the surface and the atmosphere heats up during the day and cools down at night. During this heating and cooling cycle, there is energy transfer between the layers of atmosphere, giving rise to smaller scale turbulent air masses at different altitude in the atmosphere. These turbulent air masses differ from each other in properties like size, temperature, pressure and density. This also affects their respective refractive indices. When the wavefront passes through these air-masses with different refractive indices, it faces a change in the direction of propagation. As the whole wavefront passes through the different air-masses, the changes in the direction of propagation are different and so the wavefront is distorted, as shown in fig 2.3(a) and produces speckle patterns as shown

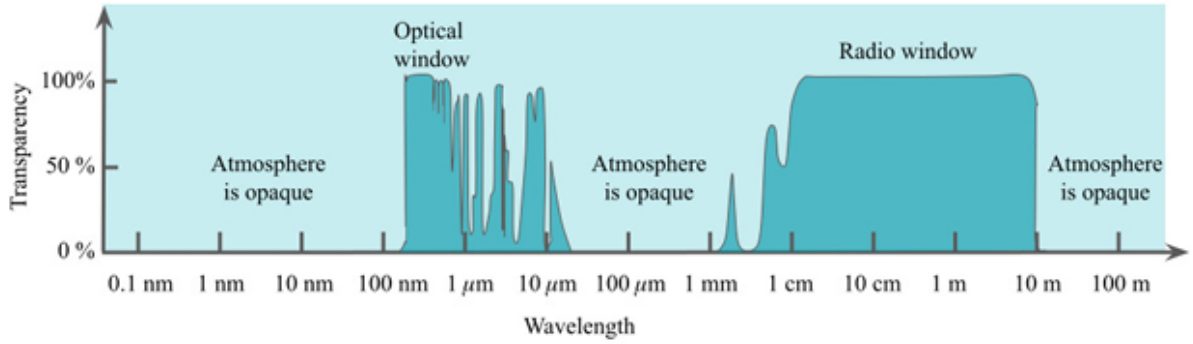

Figure 2.2: The image shows the opacity of atmosphere as a function of wavelength. Image is taken from [18].

in fig 2.3(b). This phenomenon can be well explained using Snell's Law [19], which was given by Willebrord Snell in 1621. According to Snell's Law, when a light ray transitions from one medium to another, its direction of propagation changes. This change in direction is proportional to the ratio of the refractive indices of the two media, as expressed in the equation 2.2.

$$n_1 \sin\theta_1 = n_2 \sin\theta_2 \tag{2.2}$$

where:

- n_1 is the refractive index of the medium one,
- n_2 is the refractive index of the medium two,
- θ_1 is the angle of incidence, measured between the normal and the incident ray at the boundary between the two media,
- θ_2 is the angle of refraction, measured between the normal and the refracted ray at the boundary between the two media.

The refractive index in vacuum, n_{vacuum} is 1 and that in the atmosphere close to the surface of the Earth, n_{air} is 1.0003. As discussed earlier, the air-masses in the atmosphere have different properties and thus have different refractive indices. The refractive index of these air-masses with different properties can be determined by using Cauchy-Lorentz Law, which is given by equation 2.3,

$$n \simeq 1 - \frac{77.6 \times 10^{-6}}{T}\left(1 + 7.52 \times 10^{-3}\lambda^{-2}\right)\left(P + \frac{1810 P_{H_2O}}{T}\right) \tag{2.3}$$

where:

- n is the refractive index of the medium,
- T is the temperature in Kelvin,
- λ is the wavelength of the light in nm,
- P is the atmospheric pressure in millibar,

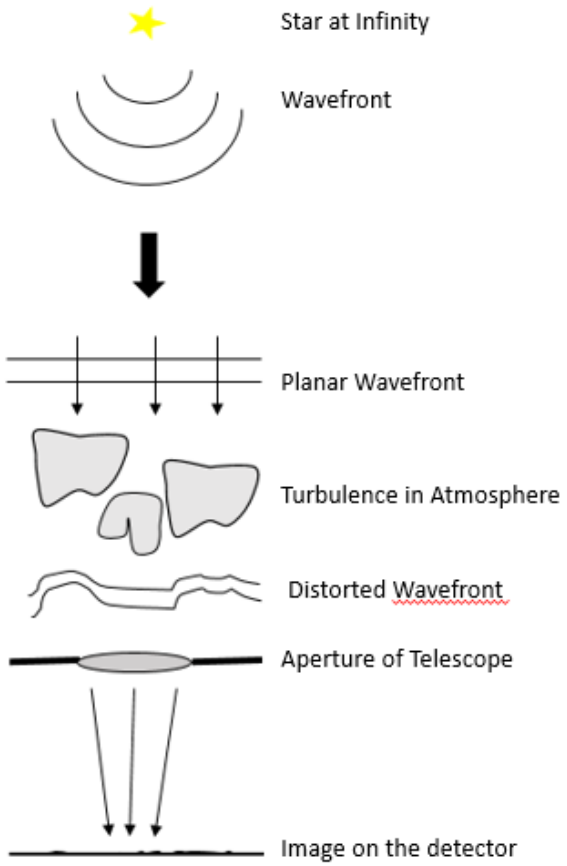

((a)) ((b))

Figure 2.3: The fig 2.3(a) is a representation of the impact of atmospheric turbulence on starlight as it passes through the atmosphere. The planar wavefront from a distant star become distorted due to atmospheric turbulence. This distortion due to the atmosphere and the telescope result in an image with bright and dark spots known as speckles. A speckle pattern captured during a lab experiment is depicted in fig.2.3(b).

- P_{H_2O} is the pressure of water vapor.

The simplified version of Cauchy-Lorentz Law is computed by eliminating the negligible factor of P_{H_2O}, the expression so computed is called Gladston's Law. It is given by the equation 2.4.

$$n - 1 \approx 77.6 \times 10^{-6} \frac{P}{T} \tag{2.4}$$

As discussed earlier, Earth has a thick atmosphere composed of many layers and each one with its own properties. Considering this challenging structure of the atmosphere where the temperature, density and pressure vary not only vertically with the height but also horizontally in the same layer. Given this complexity, it is insufficient to assume the atmosphere as a simple, smooth gradient for astronomical purposes. So to understand better the turbulence in different layers of atmosphere, it is important to consider statistical approach. Though there are several theories to understand and describe the atmospheric turbulence like Kolmogorov theory, Richardson's theory [20], Obukhov-Corrsin theory [21]

and many others, in the thesis we will focus on Kolmogorov theory of turbulence because it is one of the most widely used theory of turbulence that gives good explanation about energy cascade and also serves as a foundational basis for many other turbulence theories.

2.2.1 Kolmogorov Theory of Turbulence

We always consider the atmosphere as a wrap of gas around the Earth. According to classic studies, the motion of a fluid medium can be divided in two regimes, which are:

1. **Laminar:** In this kind of flow, the different layers of the fluid flow over each other with different speeds without mixing up or breaking the flow of the medium.
2. **Turbulent:** In this flow, the particles in the medium show an irregular flow with no defined layers.

The type of flow of a medium is defined by Reynolds' number. It was first given by Osborne Reynolds in 1883, explaining the conditions under which the laminar flow of water would change to turbulent flow in a pipe [19]. The Reynolds' number is given by the equation 2.5,

$$\mathrm{Re} = \frac{\rho u L}{\mu} \tag{2.5}$$

where:

- Re is the Reynolds number. It is a dimensionless quantity,
- ρ is the fluid density in kg/m^3,
- u is the flow velocity in m/s,
- L is the characteristic length in m,
- μ is the dynamic viscosity of the fluid in N·s/m^2.

In case of atmosphere we neglect the fluid density ρ, so the equation 2.5 becomes,

$$\mathrm{Re} = \frac{u L}{\mu} \tag{2.6}$$

The type of flow of a liquid is determined by the value of Reynolds' number. When the value Re < 500, in that case the flow is a laminar flow and the flow is dominated by the viscosity of the medium. In case when Re > 2000, the flow is termed as the turbulent flow [22]. The turbulent flow is characterized by increased mixing of the medium, high dissipation energy and formation of eddies and vortices.
When we insert the average values of u, L and μ as per the conditions in the atmosphere, we can find the nature of flow of the atmosphere. The typical values of u, L and μ are 10 m/s, 15 m and 15 x $10^{-6} m^2/s$ respectively. We obtain the value of Reynolds' number $\approx 10^7$. This is much higher the critical value of Reynolds' number, 2000, giving us solid results that the atmosphere is highly turbulent.

To understand atmospheric turbulence, A.N. Kolmogorov gave a model in 1941 to describe the energy spectrum distribution within the atmosphere [23]. He stated that the

large scale motions or eddies, also called outer scale, L_0, are induced in the atmosphere by convection. These large scale motions have very high Reynolds number compared to the critical value and thus they are very unstable. Due to instability, kinetic energy from these large scale motions is transferred to smaller scales through an energy transfer process known as energy cascade process. The small scale structures, also called inner scale, l_0, so generated are statistically homogeneous and isotropic, also their behaviour is independent of the large scale structures [24]. As the spatial scale reduces in size, the Reynolds number also gets smaller with each transfer of energy. The typical value of l_0 is less than 10 mm [25] while the size of L_0 is of few tens of meters [26]. When the value of $Re < Re_{critical}$, the kinetic energy is converted into thermal energy and the cascade transfer of energy comes to a halt. Fig. 2.4 depicts a thematic representation of this scale to scale energy transfer.

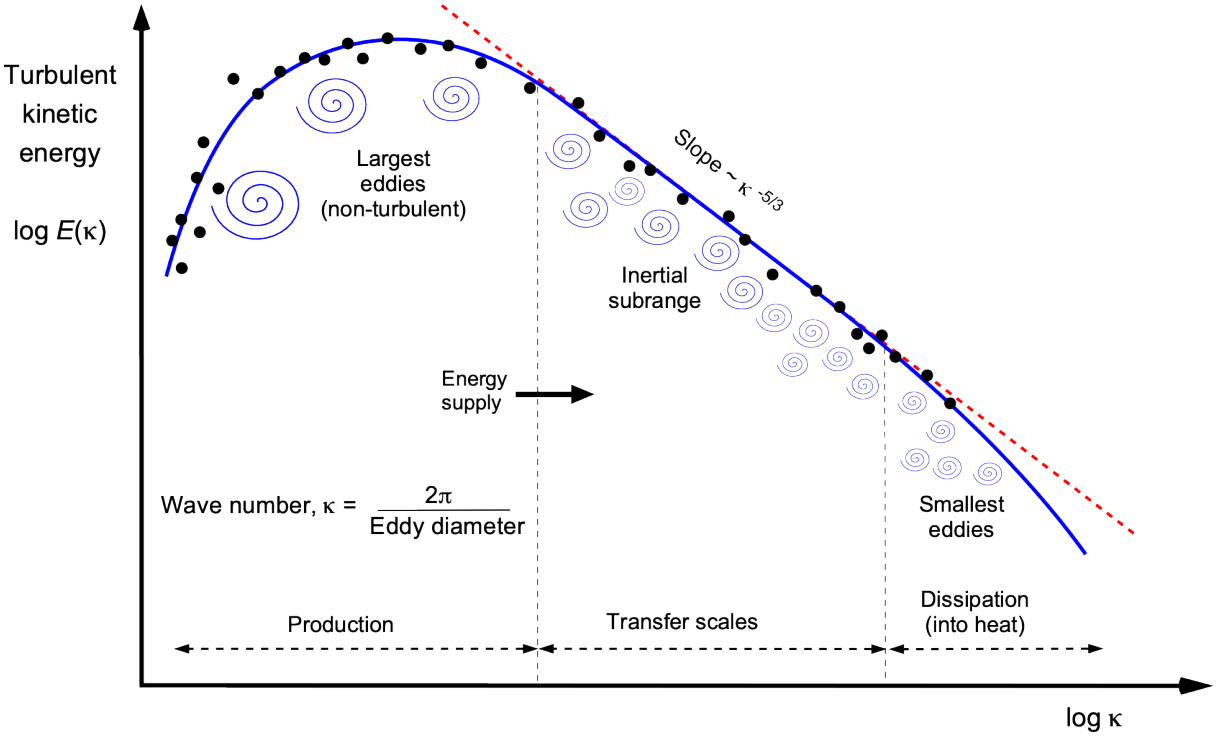

Figure 2.4: This plot shows the one-dimensional energy cascade in turbulent flow. Showing a relation between turbulent kinetic energy, E_k and the wave number, k. It illustrates the transition of eddies from production to dissipation, focusing on the inertial subrange where energy is transferred from large scale motions to small scale motions without any loss. The slope of -5/3 in this subrange is characteristic of the Kolmogorov spectrum, representing the distribution of energy across different scales of eddies. The plot is taken from [27].

Apart from the size of scales, the energy spectrum also depends on two other parameters, they are: the rate of energy dissipation per unit mass, and the kinematic viscosity. In the inertial subrange, $l_0 << L << L_0$, the effects of viscosity are negligible, and the turbulence structure is mainly governed by the energy per unit mass.
The energy spectrum for the eddies in inertial subrange can be derived through dimensional analysis. When the wave number $k = 2\pi/L$, the one-dimensional energy spectrum is given by,

$$E_k \propto k^{-5/3} \tag{2.7}$$

When it is integrated over three spatial coordinates, we have the three-dimensional energy spectrum $E_k \propto k^{-11/3}$.

Using the Kolmogorov theory of turbulence, Tatarski in 1961 gave a statistical model of wavefront distortion by the turbulent atmosphere [28]. He applied structure functions to Kolmogorov theory to describe the variation of refractive index. Originally, the expressions for velocity structure functions were derived but the atmospheric aberrations are affected by the refractive index and the temperature. The structure function for temperature and refractive index are given as equation 2.8 and 2.9, respectively.

$$D_T(\mathbf{r}_1, \mathbf{r}_2) = C_T^2 |\mathbf{r}_1 - \mathbf{r}_2|^{2/3} \tag{2.8}$$

$$D_n(\mathbf{r}_1, \mathbf{r}_2) = C_n^2 |\mathbf{r}_1 - \mathbf{r}_2|^{2/3} \tag{2.9}$$

where:

- $|\mathbf{r}_1 - \mathbf{r}_2|$ denotes the distance between the two points $\mathbf{r}_1$ and $\mathbf{r}_2$,
- C_T^2 is the temperature structure function constant,
- C_n^2 is the refractive index structure function constant.

To describe the statistics of wavefront aberrations, the power spectral density (PSD) is used. It is denoted as $\Psi(\kappa)$. The PSD is a measure that shows how much different spatial frequencies contribute to the overall distortion of the wavefront [29]. In the context of the Kolmogorov model, it helps us understand how these distortions are distributed. It is given by the equation 2.10.

$$\Psi(\kappa) = 0.033 C_N^2 \kappa^{-11/3} \tag{2.10}$$

In the atmosphere, the parameter C_N^2 influence the distortions in wavefront. These distortions generally decreases as one goes higher from the ground except for the regions that show strong wind shear or sharp temperature changes. An example of C_N^2 profile variation with height can be seen in fig 2.5.

Depending on the behavior of the parameter C_N^2 the atmosphere can be divided into three distinct layers. The first layer extends only a few tens of meters from the ground. The turbulence in this region is most intense and strongly affected by daily temperature variations. The second layer reaches up to about 1,000 meters and also experiences daily temperature influences but with much less intensity than the first turbulence layer. The third layer stretches up to approximately 20,000 meters. At this stage, the air density is lower and turbulence is mostly influenced by seasonal cycles rather than daily fluctuations. These are the three regions where the atmospheric turbulence is high and this caused high fluctuations in the refractive index.

The observations and the results from the Kolmogorov theory show consistency with

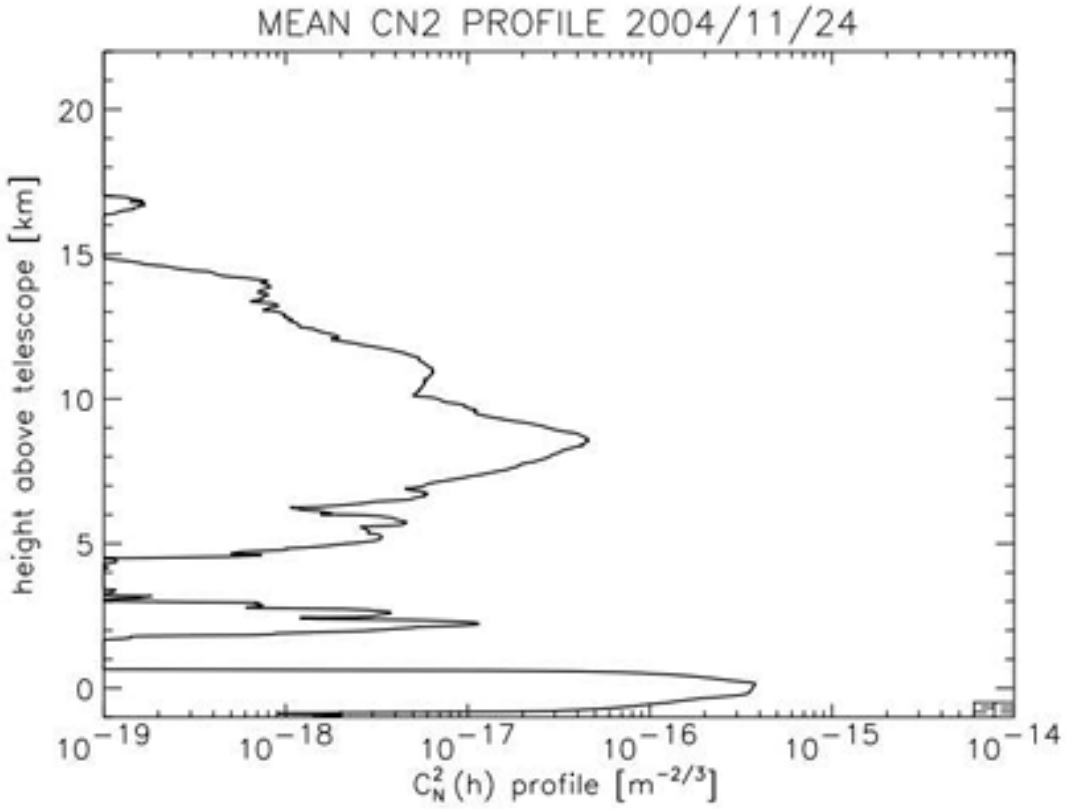

Figure 2.5: The plot shows a C_N^2 profile as a function of height. It is based on data taken at Mt. Graham with (SCIntilation Detection And Ranging) SCIDAR on 24^{th} November, 2004. The plot is taken from [29].

their results [30], so using Kolmogorov theory, we can know the effects caused by the atmospheric turbulence on seeing. We will talk about seeing and its parameters briefly in section 2.2.2.

2.2.2 Seeing Parameters

Until now we learned that the atmospheric turbulence affects the image quality. But it becomes more important to figure out and relate the parameters affecting the image quality with the results from Kolmogorov theory of turbulence.

The effects of the atmospheric turbulence on the astronomical images are expressed using **seeing**. Seeing can be refereed to the quality of the night sky. It is given by the Full Width at Half Maximum (FWHM) of the point spread function (PSF) of a celestial body. The main parameters that affect the seeing are:

1. **Fried Radius:** This parameter was first introduced by D.L. Fried in 1966 [31]. This parameter can be defined as volume of the atmosphere over which the wavefront can be considered unperturbed. The fried radius, r_0 - shown in fig 2.6, is expressed in the terms of C_n^2, as shown in equation 2.11.

$$r_0 = \left[0.424\pi^2\lambda^2(\cos\Phi)^{-1}\int_0^\infty C_n^2(h)\,dz\right]^{-3/5} \text{ m} \tag{2.11}$$

where:

- λ is the wavelength of the observed light,
- Φ is the zenith angle,
- C_n^2 is the refractive index structure constant from Kolmogorov theory of turbulence,
- z is the height above the telescope.

If the aperture of the telescope is smaller or equal in size to r_0, in that case the telescope captures a clear image as for the telescope of such a small aperture, the wavefront will be planar. But for a telescope with an aperture larger than r_0 and no adaptive optics, in those cases the resolution of telescope is limited to λ/r_0. The value of fried radius depends on the wavelength of the light observed. Usually the values are around 15 cm for V band and 40 cm for K band.

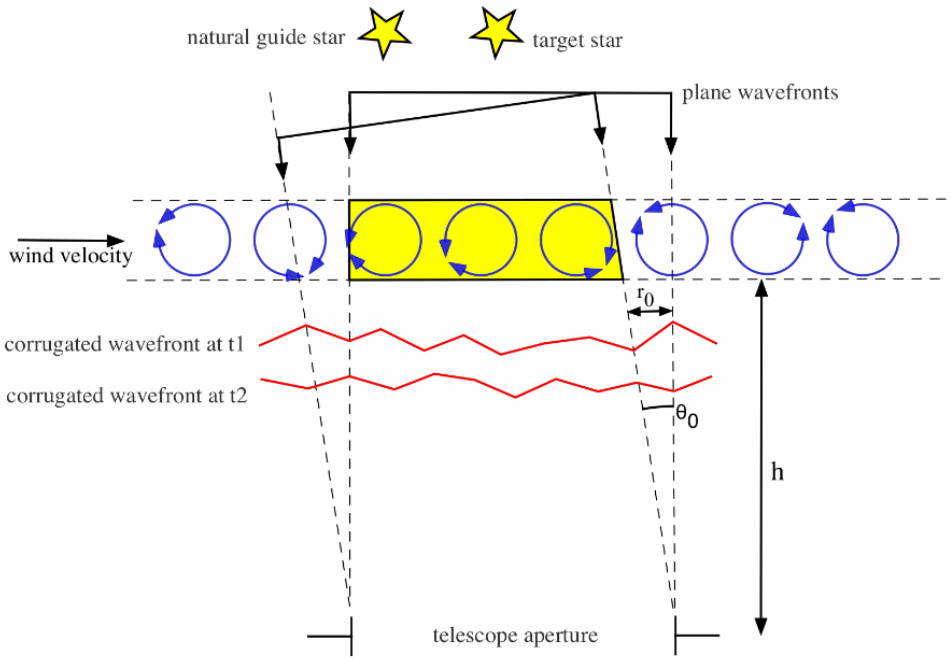

Figure 2.6: The plot schematically explains the Fried Radius, r_0 and the isoplanatic angle, θ_0. These are the parameters that affect the image quality [32].

2. **Isoplanatic Angle:** Isoplanatic angle, θ_0, is defined as the angular separation between two sources in which the distortion in the wavefront is less than one radian [33]. Within this angle, the wavefront affected by the atmospheric turbulence is similar that allows for effective correction. The Isoplanatic angle shown in image 2.6 is given by the equation 2.13 [34].

$$\theta_0 = 0.314\left(\frac{\lambda^2}{\int_0^\infty C_n^2(h)\,h^{5/3}\,dh}\right)^{3/5} \tag{2.12}$$

or in simple terms it can be given as:

$$\theta_0 = 0.314\frac{r_0}{H} \tag{2.13}$$

where, H is average turbulence height

Typically the value of θ_0 is a few arcsecs.

3. **Coherence Time:** The coherence time, τ_0, is the time period during which the atmospheric distortion is considered constant. It is given by:

$$\tau_0 = \frac{r_0}{v_{\text{wind}}} \tag{2.14}$$

where:

- r_0 is the Fried parameter and,
- v_{wind} is the wind speed in the turbulence layers.

Coherence time is usually of the order of milliseconds in IR regime and heavily depends on the altitude and atmospheric conditions. The inverse of τ_0 gives the **greenwood frequency**, f_G.

In addition to the parameters that influence seeing, there are several metrics used to measure image quality and clarity. Two of the most widely used metrics are discussed below:

1. **Strehl Ratio:** It is defined as the ratio between the peak intensity of current seeing of the PSF and that of the only diffraction limited instrument, shown in Fig 2.7. It is given by the equation

$$\text{Strehl Ratio, SR} = \frac{PSF_{seeing}(0,0)}{PSF_{dl}(0,0)} \tag{2.15}$$

where:

- PSF_{seeing} is the peak value of observed PSF and,
- PSF_{dl} is the peak value of PSF in ideal conditions.

The ideal value of SR is 1. It varies between 0 an 1, anything less than 1 indicates the poorer quality of the image.

2. **Signal to Noise Ratio (SNR):** The SNR refers to the strength of signal received by the detector compared to the noise. This parameter is dependent on the quality of the instrument. It is calculated using the formula 2.16

$$\text{SNR} = \frac{S}{\sqrt{S+N}} \tag{2.16}$$

where:

- S is the total signal detected. It is measured in photon counts.

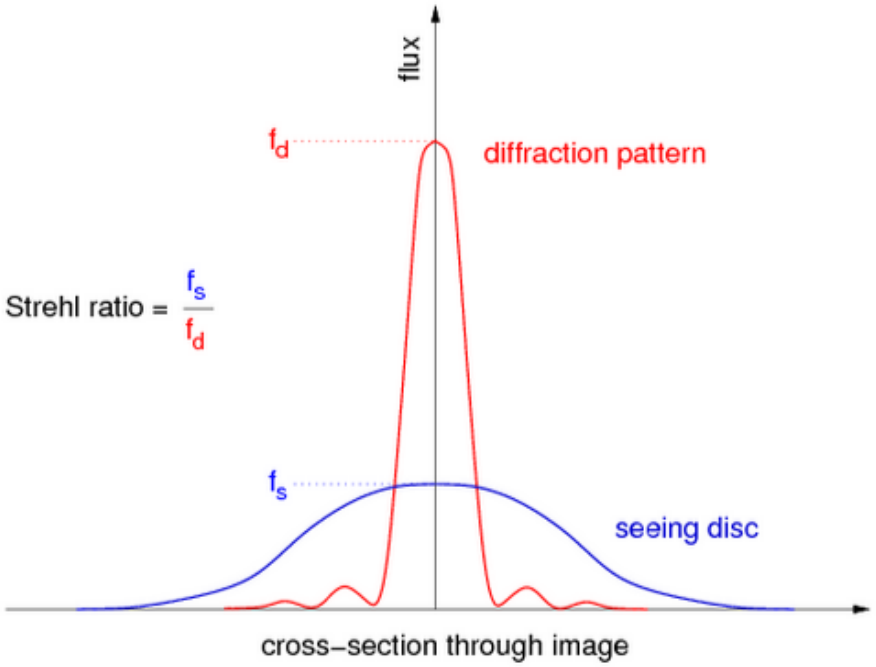

Figure 2.7: The plot shows a comparison between the diffraction pattern and the seeing disk of a source. This gives us Strehl Ratio [32].

- N is the total noise. It includes contributions from various sources such as sky background, dark current, and readout noise.

We will see in detail how to calculate SNR in section 5.3.4.3.

Now having knowledge of the factors that affect the wavefront, we can now discuss the idea of AO in the next section and show AO has revolutionized the imaging at telescopes with large aperture.

2.3 Adaptive Optics as a Solution

As we learned in previous sections, the image quality of a telescope depends on its aperture and the atmospheric conditions. Ideally, a diffraction-limited telescope should achieve a resolution of $\theta \sim \lambda/D$, but the atmospheric turbulence degrades this resolution to $\theta \sim \lambda/r_0$, making the telescope seeing-limited. A larger aperture captures more light, enabling it to collect more photons and therefore increase the SNR. However, it does not guarantee better resolution due to the impact of atmospheric distortions.

To exploit the capabilities of large aperture telescopes we need AO. AO is the technique to read the distortions in an incoming wavefront and correct them in real time. The idea of AO was first put by Babcock in 1953 [9] when he used guider instruments to solve for the shift of a star image. During his experiments he found two major limitations, that are requirement of a reference source and size-limited field of view (FoV). The idea to use AO took over two decades before it was put to use on a telescope [35] and now it is being

used at most of the telescopes with a large aperture. One example of how AO corrections improves the quality of astronomical imaging is shown in fig 2.8.

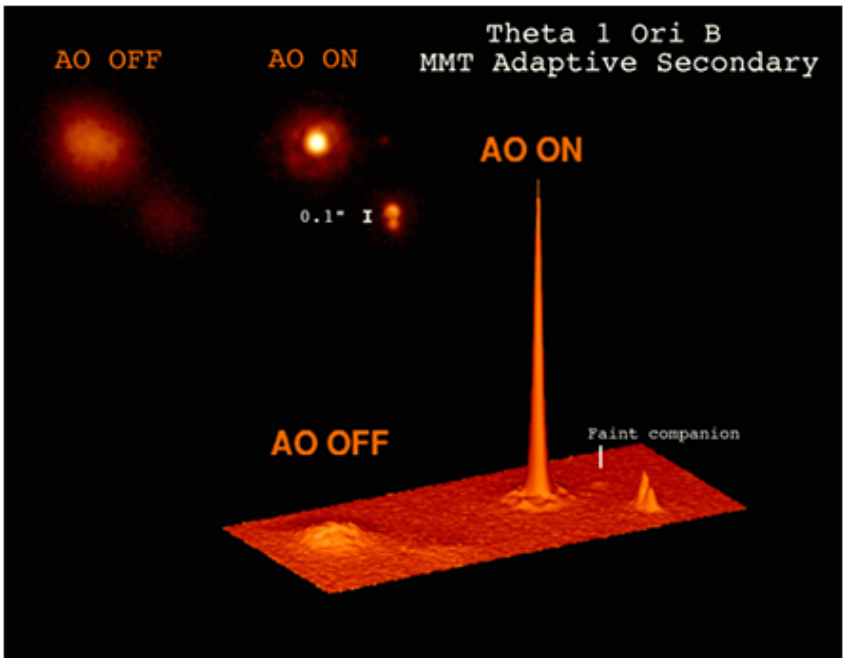

Figure 2.8: This plot shows how AO can be useful to improve the image quality. It can be clearly seen that with **No AO** on the telescope, only two stars appear in the image. On the other side when AO is used, a total of 4 stars can be seen [36].

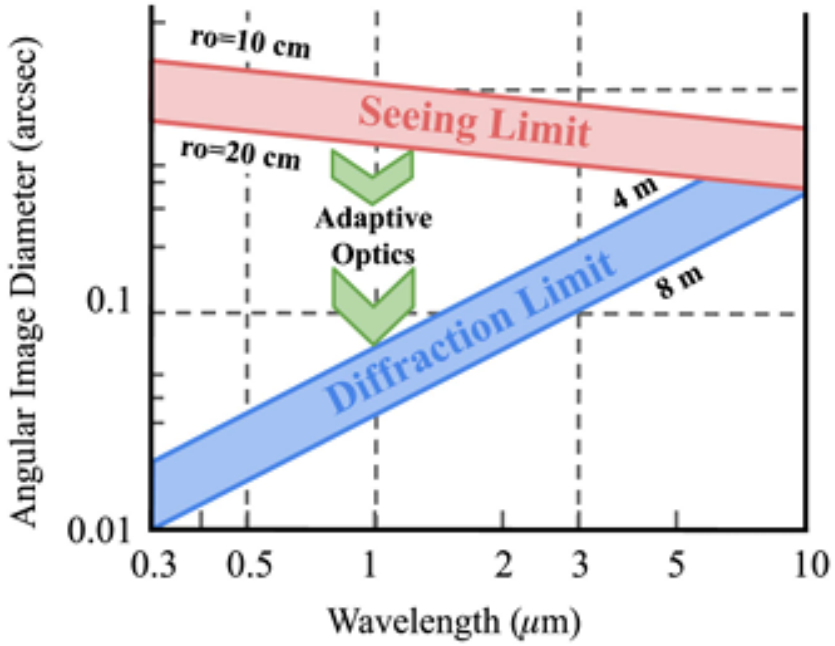

Figure 2.9: This plot shows an exemplar comparison between the seeing limit and diffraction limit as a function of wavelength. The red band represent the seeing limit for different values of the Fried parameter, r_0, and the blue band shows the diffraction limit for telescopes with apertures from 4m to 8 m [18].

The visible wavelengths are more influenced by the diffraction limit of the telescope, which restricts its resolution. AO tries to fill this gap and pushes a seeing-limited telescope to a diffraction-limited telescope, as shown in fig 2.9, which is immensely useful for shorter wavelengths.

The AO is composed of several independent technologies put together. We will understand better about the components that make up the AO in next section.

2.3.1 Main Components of Adaptive Optics

The correction of the wavefront by using AO is a complex task as it is required to be done in real-time, which is of the order of milliseconds. AO uses distortion as a tool to reduce distortions from the wavefront. It is possible by using component that introduces equal but opposite distortion to generate a planar wavefront. To do so, the aberrations are first calculated using a real-time computer and then the signals are sent to the wavefront corrector that corrects the aberrations in the incoming wavefront. This correction has to be introduced to the wavefront in time equivalent or less than the coherence time, τ_0. The wavefront when enters the telescope is first corrected and then it reaches the telescope scientific camera, as shown in fig 2.10.

The components that make up the AO are:

- **Wavefront Sensor:** The Wavefront Sensor (WFS) plays a crucial role in an AO system by detecting distortions in the incoming light wavefront caused by atmospheric turbulence. It measures the phase variations, where these distortions appear as deviations from the ideal wavefront shape. This information is then used for real-time correction to restore image quality. Several types of WFS have been developed over time, each designed for different sensing needs, such as the Shack-Hartmann [38] and Curvature WFS [39], which are commonly used to address both low- and high-order aberrations. More detailed descriptions of these sensors will be provided in section **??**.

- **Real-Time Computer:** Real-time computers are named so for their speed to process the wavefront read by the WFS. These computers analyze incoming wavefront distortions in real-time and adjust deformable mirrors within milliseconds to counteract atmospheric turbulence [40].

  There are two main ways to reconstruct a wavefront:

  - Zonal Reconstruction: In zonal reconstruction, the pupil of telescope is divided into several smaller regions and then the wavefront is measured separately for each of these regions. Then all the local wavefronts are combined to reconstruct the final wavefront.

  - Modal Reconstruction: The modal reconstruction uses mathematical functions to describe the entire wavefront as sum of coefficients. One example of such a mathematical function is Zernike polynomials [41].

    In modal mode, the wavefront is treated as functions which are given by the equation 2.17,

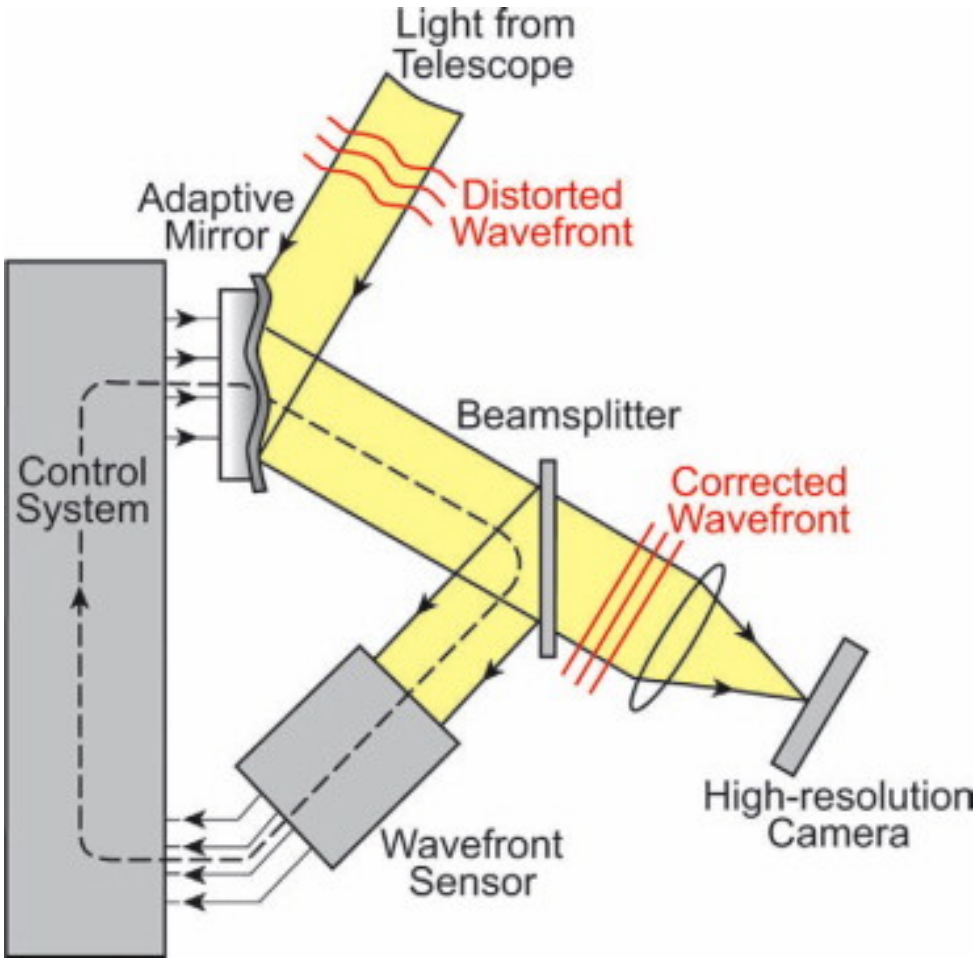

Figure 2.10: This shows a schematic diagram of an adaptive optics system. Distorted wavefront from a distance source enters the telescope. When the wavefront reaches the beam-splitter, it directs a part of the signal to a wavefront sensor. The wavefront sensor then analyzes the distortions and sends feedback to a wavefront reconstructor or real-time computer. This system send signal to adjust the shape of the deformable mirror in real time. The shape of deformable mirror corrects the wavefront, so compensating for atmospheric aberrations. The corrected wavefront is then sent to the high-resolution scientific camera. The image is taken from [37].

$$W(x,y) = \sum_n C_n P_n(x,y) \tag{2.17}$$

where:

* $W(x,y)$ represents the reconstructed wavefront,
* C_n are the linear combination coefficient for each mode,
* $P_n(x,y)$ are the polynomial terms representing the wavefront for a single mode.

Equation 2.17 is more of a general equation for the wavefront reconstruction. A more detailed explanation of the wavefront reconstruction function was given by Noll in 1976 using the aberrations from Kolmogorov theory of turbulence where the term P_n are the Zernike polynomials. Zernike polynomials, first introduced by Frits Zernike in 1935 [42], are a set of polynomials defined on a unit circle [43]. It is given by the equation 2.18.

$$W(\rho,\theta) = \sum_n C_{nm} Z_{nm}(\rho,\theta) \tag{2.18}$$

$$Z_n m(\rho,\theta) = \rho^n \cos(m\theta) \tag{2.19}$$

where

* $Z_{nm}(\rho,\theta)$ represents the Zernike polynomials,
* n represent the radial order of Zernike polynomials
* m represents the azimuthal frequency.

The modal wavefront reconstruction is one of the most used methods for its properties like error propagation and computational time.

Once the wavefront is measured by the RTC, it calculates the necessary corrections and directs these adjustments to wavefront corrector.

- **Wavefront Corrector:** A wavefront corrector which is usually a deformable mirror (DM), adjusts high-order or just low-order aberrations in the wavefront based on the number of actuators it has. These actuators are located behind the reflective surface of the mirror and defines the degrees of freedom (DoF) for the DM. Higher number of actuators helps the mirror to finely shape itself for precise wavefront correction. The actuators can be thought as tiny pistons that push or pull on the mirror's thin reflective sheet, altering its shape in real time based on the signal received from real-time computer.

  Apart from the piston actuators, there are some other technologies that are used in DMs, such as Piezoelectric actuators [44], Electrostrictive materials [45], Liquid crystal arrays [46], voice-coil actuators [47].

- **Reference Source:** Reference star or guide star are the bright sources of light which are used to correct for the atmospheric distortions. There are two types of reference stars: Natural Guide Stars (NGS) and Laser Guide Stars (LGS). The reason why the target source itself is not used as the reference is that many astronomical objects are too faint or extended which makes it difficult to accurately measure wavefront distortions. So a bright reference stars provide a reliable source for wavefront sensing and correction. A detailed discussion on reference stars will be provided in section2.3.3.

2.3.2 Limitations of Adaptive Optics

AO was developed to mitigate the shortcomings with the atmospheric turbulence and to a large extent astronomers have been successfully able to achieve it. As it has been said that every technology has both pros and cons, AO has its own cons that affect the wavefront distortion or do not completely reduce the effects of atmospheric turbulence from the wavefront. Some of the shortcomings of AO are:

- **Time Lag in Corrections:** The wavefront reconstructor is a real-time computer but still there is some time lag seen between the measurement of the wavefront distortion and sending signal corrections to deformable mirror [48].
- **Cone Effect (Focal Anisoplanatism):** During the wavefront correction with a LGS, the wavefront from the LGS samples only a cone rather than a full cylinder of turbulence. Due to this cone effect, some part of the atmosphere is not corrected for atmospheric distortion, as shown in fig 2.11, specially for large telescopes and this reduces the performance of AO.
- **Limited Sky Coverage:** Due to anisoplanatism, shown in fig 2.12, we only have a limited sky coverage . AO and the LGS drastically reduces this effect..

2.3.3 Reference Sources

To correct for the atmospheric distortion, an AO system needs bright guide stars. During the introduction phase of AO to astronomy, Natural Guide Stars (NGS) were mostly used to serve the purpose but due to limitations, a new class of guide stars, Laser guide star was born. We will discuss about both in detail in following section. We will also discuss about another class of guide star which is currently being explored in section 2.3.3.3.

2.3.3.1 Natural Guide Star

A NGS is a natural star, which is used by the AO system to mitigate the effects of atmospheric distortions. In order to be used as a reference star, the star has to be bright enough to be detected by the wavefront sensor. For the MORFEO system at the Extremely Large Telescope (ELT), the typical limiting magnitude for natural guide stars in the V-band is around 16-17 [50]. These constraints limit the sky coverage of a telescope. Sky coverage changes from one point on sky to another drastically. The number of the presence of NGS varies from a maximum in the galactic plane to the minimum at galactic poles. We will also discuss about the distribution of NGS in details in chapter 4.

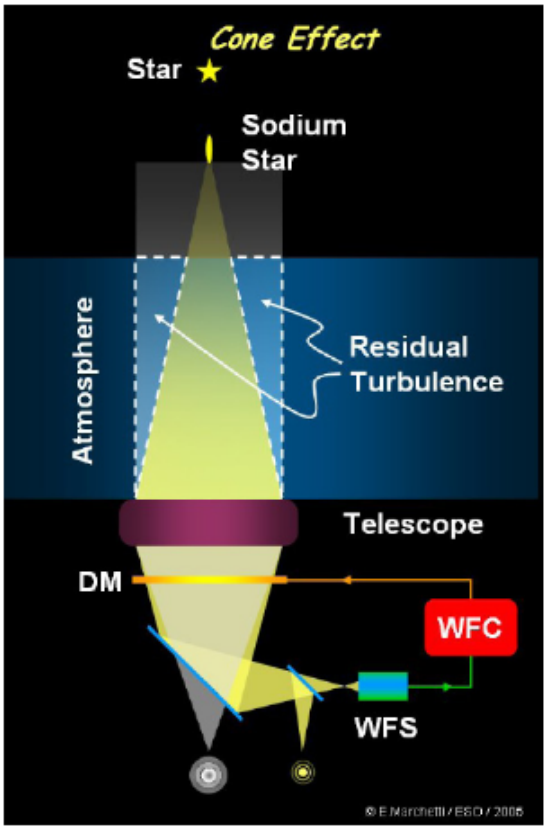

Figure 2.11: This figure shows the cone effect, where a Na-LGS only corrects a part of the atmosphere. Therefore some turbulence remains uncorrected for the actual star that is being observed. This partial correction reduce the accuracy of adaptive optics [49].

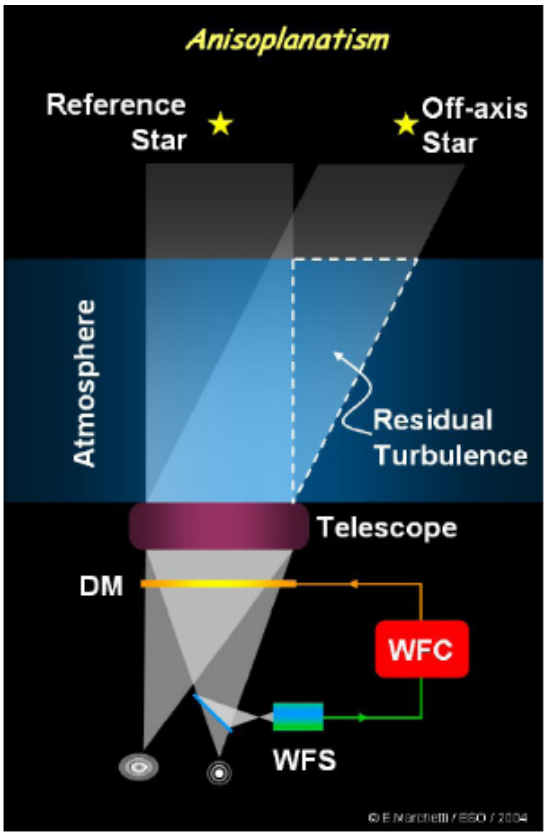

Figure 2.12: The image shows how the atmosphere affects stars differently depending on their position in the sky. Only a part of the wavefront coming from the off-axis star can be corrected for atmospheric distortion [49].

Figure 2.13: Two figures depicting the limitations of Adaptive Optics.

Because of the limited sky coverage of the NGS, we need to look for other sources that can help AO systems achieve their true potential. For the same, a new guide star, LGS, made its way to the telescopes.

2.3.3.2 Laser Guide Star

The first use of LGS was done by the US Military [51]. Later on astronomers also got access to this technology. The LGS are created by firing a laser, positioned close to the telescope, to the sky. The laser fired, excites the atoms in the atmosphere, creating a LGS. Currently there are two types of LGS in use: Rayleigh scattering and Sodium LGS.

Rayleigh Scattering In Rayleigh Scattering, the LGS is created at a height 10-20 Km from the ground [52]. The LGS is obtained as light back-scattering effect due to fluctuations in air density. The Rayleigh scattering is more efficient at short wavelengths. This kind of LGS gets fainter with increase in the altitude as the atmosphere gets more and more thinner.

Rayleigh scattering has been found to be inefficient for correcting atmospheric turbulence due to its low altitude [53]. This only allows for partial correction of distortions and the higher-altitude layers of the atmosphere remain uncorrected. The cone effect associated with Rayleigh scattering results in a narrower sampling of region. This leads to incomplete wavefront sampling and limits the accuracy of adaptive optics corrections.

Sodium Laser Guide Star The sodium LGS or Na-LGS is created by exciting the sodium atoms using a laser of 589 nm wavelength which corresponds to the D2 sodium transition, this causes the atoms to emit light and form a Na-LGS. The layer of sodium atoms, which is present in the mesosphere at an altitude of about 89 - 92 km, is a result of ablation of meteorites. Due to disintegration, the sodium atoms are distributed at this altitude. The thickness, which is about 10-15 km, and density of sodium layer varies with time which can fluctuate due to variation in meteoroid activity, atmospheric dynamics and also depends on seasonal variations [54].

Flux of Na-LGS depends on sodium column density which varies with time from about 2 x $10^{13} ph/s/m^2$ to 20 x $10^{13} ph/s/m^2$. The flux shows over 10-20% fluctuations over few minutes of time . The variation in ground return flux is shown in fig 2.14, the results are from a simulation conducted on the data taken on october 23, 2006 at Starfire Optical Range (SOR, located at 35^oN, 160^oW) [55].

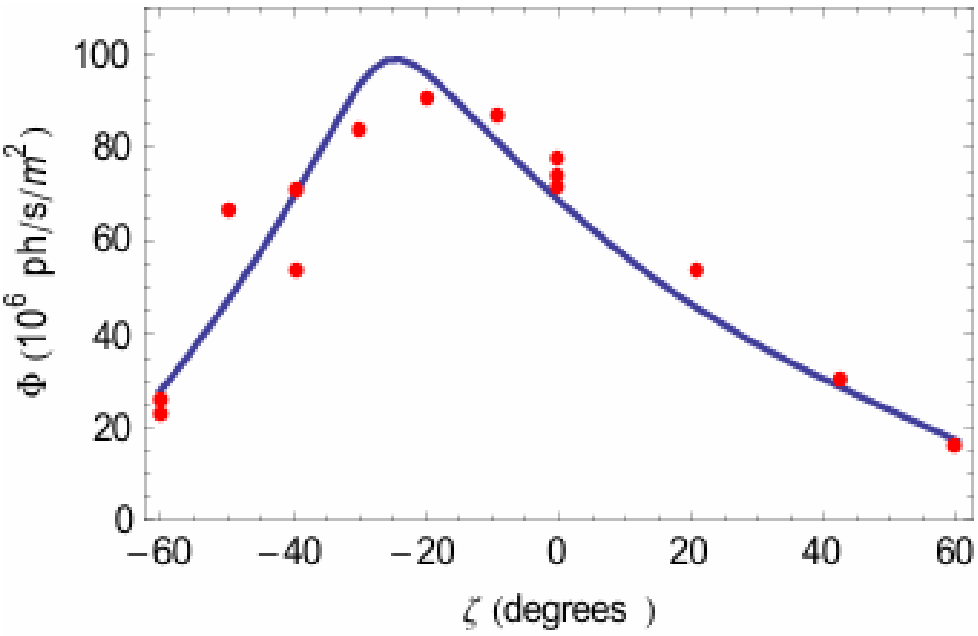

Figure 2.14: The plot shows variation in the ground return flux Φ along the South-North meridian. X-axis shows telescope's angular deviation from the zenith ζ and y-axis shows the flux received. Image taken from [55].

Though Na-LGS are extremely potential reference sources, it still has several shortcomings for astronomical purposes, which are:

- The turbulence of the atmospheric layers above the LGS can not be corrected.

- The cone effect also exist with the Na-LGS.
- Na-LGS also does not allow to determine the tip-tilt because the beam travels twice through the same atmospheric layers in a time smaller than the coherence time, bringing the tip-tilt correction to a value closer to zero [56] [57].
- The Na profile in the atmosphere is under constant change within the night.
- Due to the finite distance of LGS, a static aberration is introduced as the telescopes are designed to focus at infinity.
- Another big problem with Na-LGS is its elongation. Because the thickness of sodium layer in the atmosphere varies between 10-15 km, the LGS appears as a elongated source and not a point source for which most of the wavefront sensors are designed [58].

2.3.3.3 Orbiting Configurable Artificial Star

ORbiting Configurable Artificial Star or ORCAS is a concept for next generation of artificial guide star. In this, a satellite or a source could be placed in the orbit of the Earth. This source would be able to generate artificial stars at all the wavelengths, providing better correction even for the thinnest layer of the atmosphere. The most important property of this kind of artificial source will be that it would provide a stable and consistent reference point for future AO systems [59].

2.3.4 Adaptive Optics Techniques

AO systems help us improve the imaging quality. A single AO system called SCAO [60] can only correct for a limited FoV as it measures distortions using a single guide star which can only provide corrections for a small volume of atmosphere. To increase the FoV, several techniques have been devised over time. Some of them are Ground-layer AO (GLAO) [61], Multi-Conjugate AO (MCAO) [62], Laser Tomography AO (LTAO) [63] and so on several others. For the purpose of this thesis we will focus on SCAO and MCAO, these are explained in sections 2.3.4.1 and 2.3.4.2 respectively.

2.3.4.1 Single-Conjugate Adaptive Optics

Single Conjugate Adaptive Optics (SCAO) is the most basic form of adaptive optics used in ground-based telescopes to correct for atmospheric turbulence in real-time, as shown in fig 2.15. It employs a single DM, this DM is conjugated to a specific altitude in the atmosphere, where corrections are applied to restore the wavefront closer to its undistorted state [34].

SCAO is highly effective in producing high-resolution images for small FoV but it is a highly time consuming process to observe each of the target in the sky individually. Also the effectiveness of SCAO is limited by the size of the isoplanatic angle which is typically around 10-20 arcseconds. It means that only objects within this narrow field of view near the guide star can be corrected for the distortions. SCAO has the advantage of delivering a high SR, $> 70\%$ in best seeing conditions [64],but only for a small FoV, until

the effect of cone effect start impacting the AO performaces. These limitations have led to the rise of other AO techniques such as MCAO.

2.3.4.2 Multi-Conjugate Adaptive Optics

The Multi-conjugated Adaptive Optics or MCAO technique was first introduced by Beckers in 1988, [65] to overcome the shortcomings of SCAO. This technique uses multiple reference stars to correct for aberrations over a large FoV. Also to correct for multiple guide star, multiple DMs is used on the telescope. The whole system relies on use of a combination of both NGS and LGS as planned for ELT. As MCAO uses multiple targets and DMs, it also has the capabilities to effectively reduce anisoplanatism [66]. Depending on what is being focused by each DM, MCAO can be divided into two. They are:

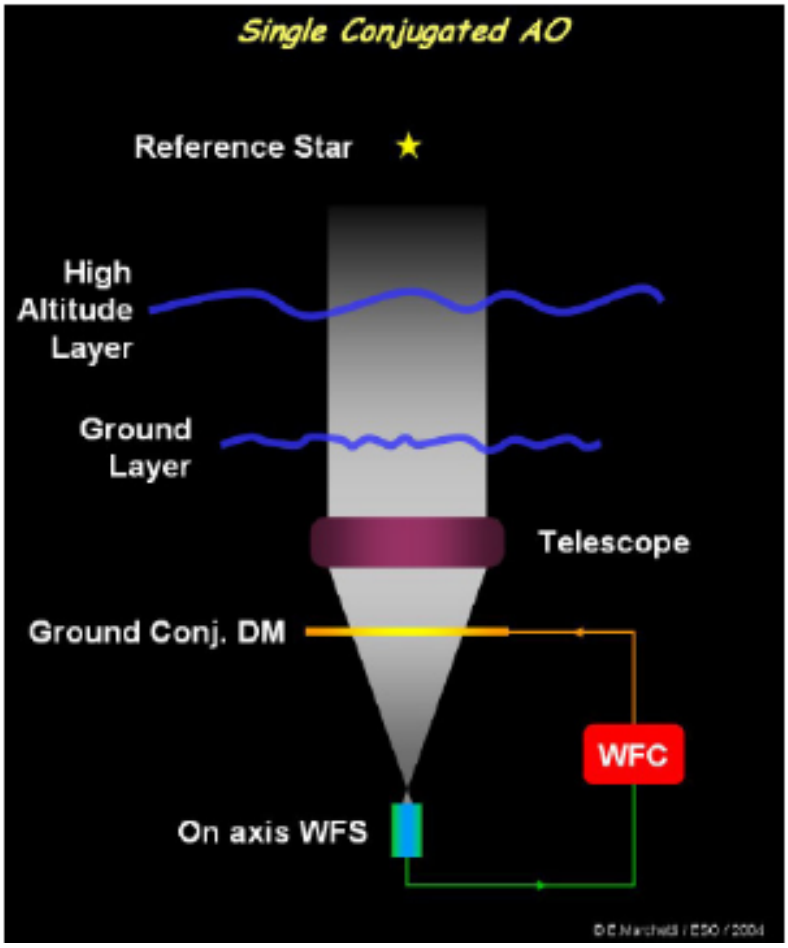

Figure 2.15: This figure is the representation of Single-Conjugated Adaptive Optics (SCAO). The image is taken from ESO website [49].

Star Oriented MCAO In Star-Oriented MCAO, each guide star is treated independently by a WFS. Each WFS measures the wavefront distortions caused by the atmosphere along the line of sight to its respective guide star. These measurements are then combined using tomographic reconstruction techniques to estimate the 3D distribution of turbulence at different altitudes [67].

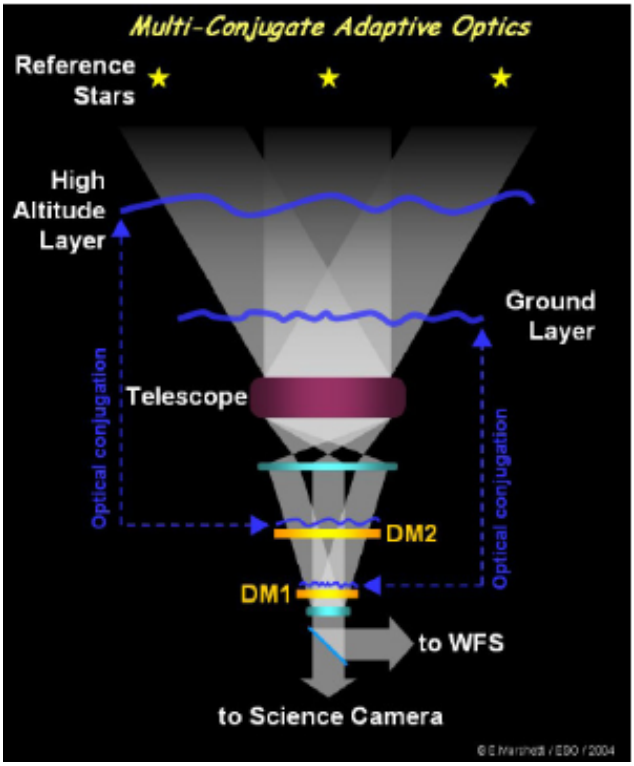

Figure 2.16: This figure is a simple representation of Multi-Conjugated Adaptive Optics (MCAO). The image is taken from ESO website [49]

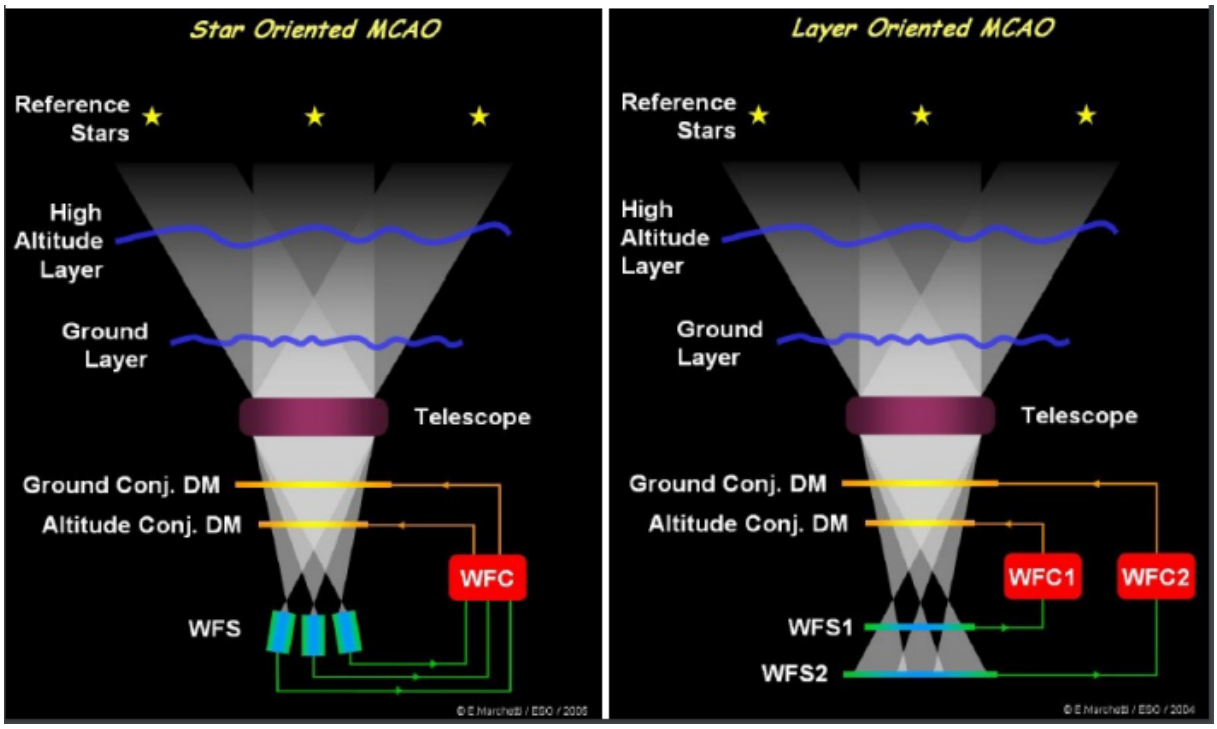

Figure 2.17: In this figure, star-oriented MCAO is shown in the image on left and layer-oriented MCAO is shown in the image on right. The images are taken from ESO's website [49].

Since the WFS collects data from multiple stars, star-oriented MCAO provides a complete picture of atmospheric distortions. This method allows corrections over a broader area of the sky and can effectively expand the corrected FoV to several arcminutes.

Layer Oriented MCAO: Layer-Oriented MCAO system focus on the atmospheric layers rather than each individual star. In this approach, multiple guide stars contribute their wavefront signals to common WFS for each atmospheric layer. The system gathers wavefront data from several stars simultaneously to focus on correcting turbulence in specific atmospheric layers. In layer-oriented MCAO each layer corresponds to one DM that compensates for the distortions at that altitude.

Layer-Oriented MCAO systems are more efficient than star-oriented ones, as they reduce the complexity by collecting the data for each layer. This method also allows for a more effective use of faint guide stars, eventually broadening the coverage of the sky but its accuracy with the correction might be less as the guide star can not fully sample the entire volume of atmospheric turbulence.

Though currently most of the telescopes use SCAO, MCAO is specifically beneficial for large telescopes, for example MACAO for VLTI and Gemini[68]. Currently the MCAO system for ELT, MORFEO, is in development phase, we will discuss more about the system and its capabilities in chapter 4.

3 Wavefront Sensors

Wavefront sensors (WFS) are essential tools that measure the shape and phase of an optical wavefront after it travels through the turbulent layers of Earth's atmosphere. By detecting and measuring the effect of atmospheric distortions in real time, WFS enable precise operation of AO systems, significantly reducing the blurring effects caused by atmospheric turbulence. They allow ground-based telescopes to reach high-resolution imaging levels similar to those of space-based telescopes. By repeatedly making the necessary measurements to the wavefront, they allow to continuously adjust mirror shapes to compensate for atmospheric turbulence, which by producing small scale distortions can degrade image quality.
In this we will chapter explore various types of wavefront sensors most commonly used at telescopes, examining their characteristics and limitations, particularly when a laser is launched from the side of the telescope. Finally, we will introduce a novel wavefront sensor currently in the testing phase, which has the potential to advance atmospheric correction techniques and improve the overall performance of AO systems using Na-LGS technology.

3.1 Wavefront Sensors in Use

Several types of wavefront sensors are currently being used in modern adaptive optics systems. Each one of them has a specific method of measuring and reconstructing the shape of the wavefront. Depending on the telescope, the type of aberration to be corrected and the application, different sensor are opted. The simplest WFS is a Quad-Cell WFS and the most commonly used WFS include the Curvature WFS, Shack-Hartmann WFS, and Pyramid WFS which we will discuss in the following sections.

3.1.1 Quad Cell Wavefront Sensor

The Quad-Cell Wavefront Sensor is a simple design used to evaluate the tip-tilt of an incoming wavefront. It works by splitting the light into four beams using detectors arranged in a square grid, as shown in fig 3.1. These detectors are placed in the telescope's focal plane, where the diffraction-limited PSF would ideally focus without any aberrations. By measuring the intensity of light in each of the four sections, the sensor can track spot movements which are directly proportional to the first derivative of the shape of the wavefront. This allows the system to estimate the overall tilt or deviation of the wavefront by measuring the signal along x, S_X, and y, S_Y, direction, they are given by the equation

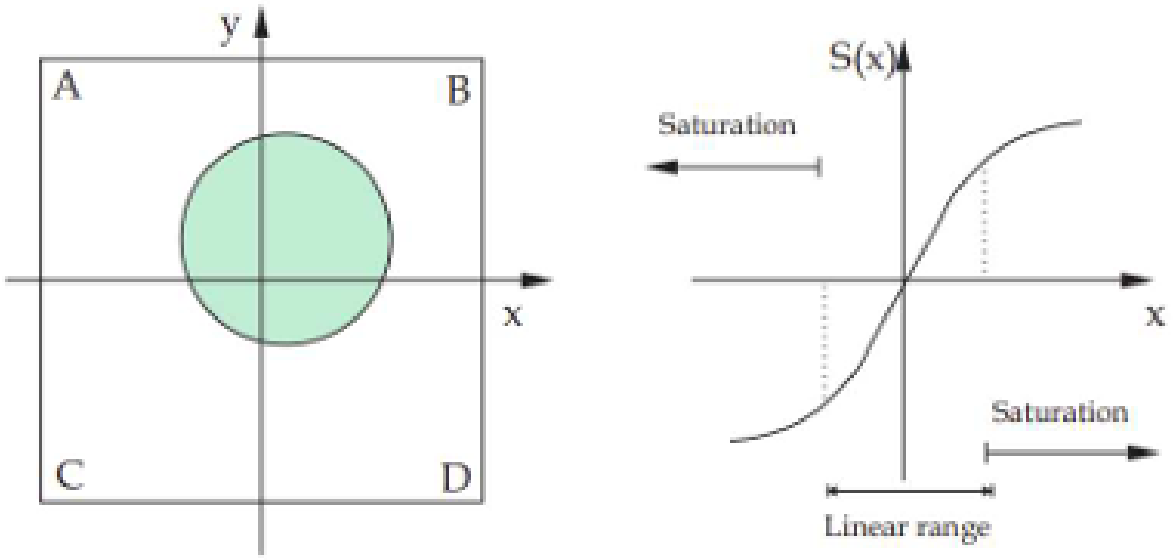

Figure 3.1: The plot shows the working principle of a Quad-Cell WFS, with light spot distribution across A, B, C and D quadrants and on the right, the resulting response curve S_X, showing the linear range and saturation points. The image is taken from Maria Bergomi's PhD Thesis[69].

$$S_x = \frac{(B+C)-(A+D)}{A+B+C+D} \tag{3.1}$$

$$S_y = \frac{(A+B)-(C+D)}{A+B+C+D} \tag{3.2}$$

where A, B, C and D are the intensities in the quadrants as shown in fig 3.1.

While Quad-Cell sensors provide coarse measurements, making them less effective in environments with very high atmospheric turbulence. So the technology is mostly used for basic optical alignment tasks and used in Shack-Hartmann WFS and Pyramid WFS.

3.1.2 Shack-Hartmann Wavefront Sensor

The Shack-Hartmann Wavefront Sensor (SH-WFS) is based on Quad-Cell WFS concept and known for its ability to detect both low- and high-order aberrations by applying it across multiple subapertures. It works by dividing the incoming wavefront into smaller sections using an array of lenslets which focus each portion onto a detector. Each spot reflects the local tilt of the wavefront that enables high-precision measurements. If the wavefront is undistorted, the focused spots align perfectly with the grid, as shown in fig 3.2. Any kind of distortions in the wavefront can cause the spots to shift. This shift in the wavefront allows the sensor to determine the local wavefront slope and reconstruct the overall wavefront for correction.

Major challenge with SH-WFS arises when using fainter stars as reference sources as the lenslet array results in significant loss of light radiation. This problem can be solved by utilizing the LGS technology, but LGS comes with their own cons. As Na-LGS are

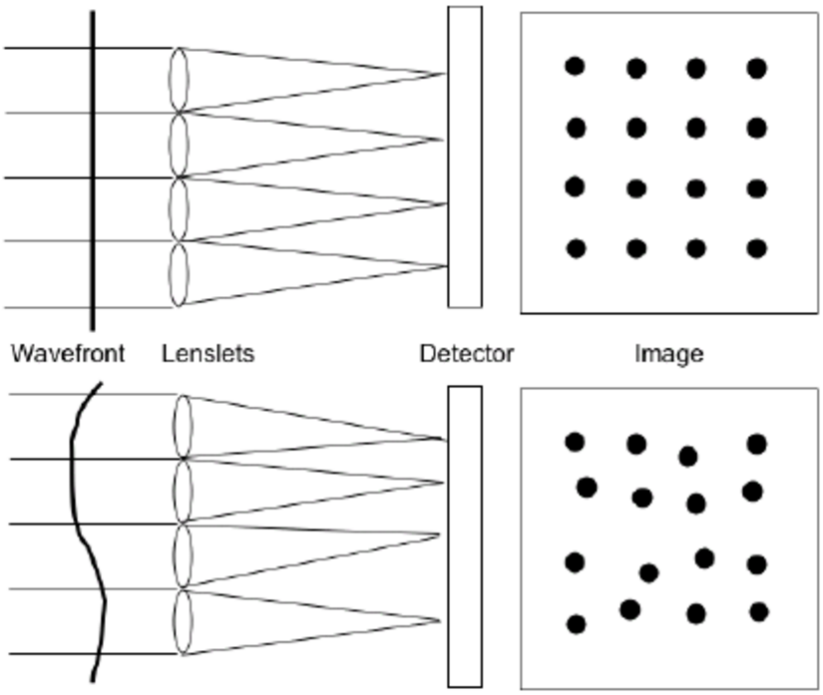

Figure 3.2: The figure on the top shows a flat wavefront forms a regular grid of focused spots on the detector while a distorted wavefront causes the spots to shift from their ideal positions, indicating local wavefront slopes is depicted by the image on the bottom. The image is taken from Vallerga et. al 2005 [70].

extended sources with some orientation based on the sky region with respect to the telescope. The problem is even more pronounced in case of large telescopes where Na-LGS is being used or planned to use. The LGS appears elongated in the subapertures positioned far from the laser launch site at the edge of the pupil. This elongation results in reduced sensitivity when measuring the first-order derivative of the local wavefront. The degree of spot elongation depends on the position of the subaperture within the pupil and the orientation of the LGS [71]. As the subapertures move farther from the laser source, the elongation becomes more pronounced, leading to variability in sensitivity across the pupil. This differential elongation is shown in fig 3.3

For example, for a 40-meter diameter telescope, with an average sodium layer height of $H = 92$ km and a thickness variation of $\Delta H = 10$ km, the spot elongation can reach 6.5 arcsec when the LGS is launched from the center of the telescope aperture. Whereas, if the laser is projected from the edge of the telescope aperture, the elongation can increase to double that value [73]. In the most extreme case, when observing from the subaperture farthest from the laser launcher, the elongation ratio between the long and short axes of the spot becomes significantly large. This leads to a photon noise variance approximately 600 times greater along the long axis, causing a substantial reduction in the SNR [18].

3.1.3 Curvature Wavefront Sensor

The Curvature Wavefront Sensor was first introduced by Roddier in 1987 [74]. It stands out from other types of wavefront sensors due to its ability to detect the second derivatives of the wavefront. Its unique design, shown in fig 3.4, consists of two detectors—one placed

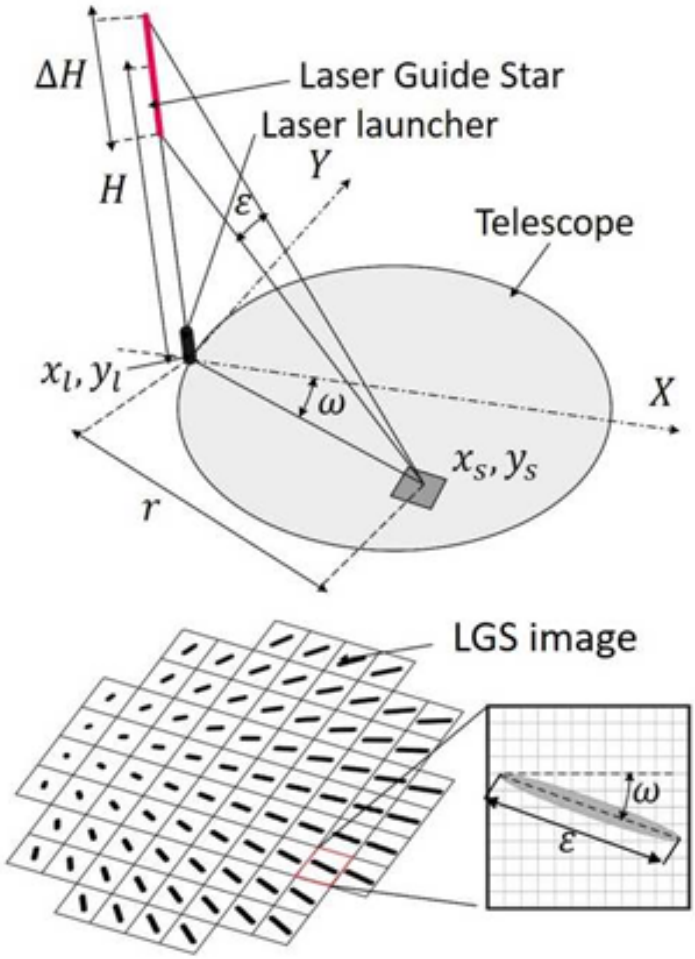

Figure 3.3: This is a schematic diagram of the Shack-Hartmann WFS with Na-LGS. It shows the spot elongation effect in the Na-LGS image caused by the height difference, ΔH, and orientation of the laser with respect to the telescope. The lower image highlights the resulting elongated spots on the WFS, which are used to measure wavefront distortions. The image is taken from Lombini et al. 2021 [72].

before the telescope's focal plane and the other after it. In this configuration, the sensor captures the light distribution at both the intrafocal and extrafocal planes. Based on the geometric approximation, a wavefront with positive curvature[1] forms an image in the intrafocal plane, while a negative curvature[2] wavefront produces the opposite effect, creating the image in the extrafocal plane [34]. This configuration allows the Curvature WFS to provide a different approach to measuring wavefront distortions, setting it apart from more conventional methods.

[1]Positive curvature refers to a wavefront that converges before the focal plane. It focuses the light inwards resulting in a brighter image at the intrafocal plane.

[2]Negative curvature refers to a wavefront that diverges beyond the focal plane, focusing light outward. It results in a spread-out image at the extrafocal plane.

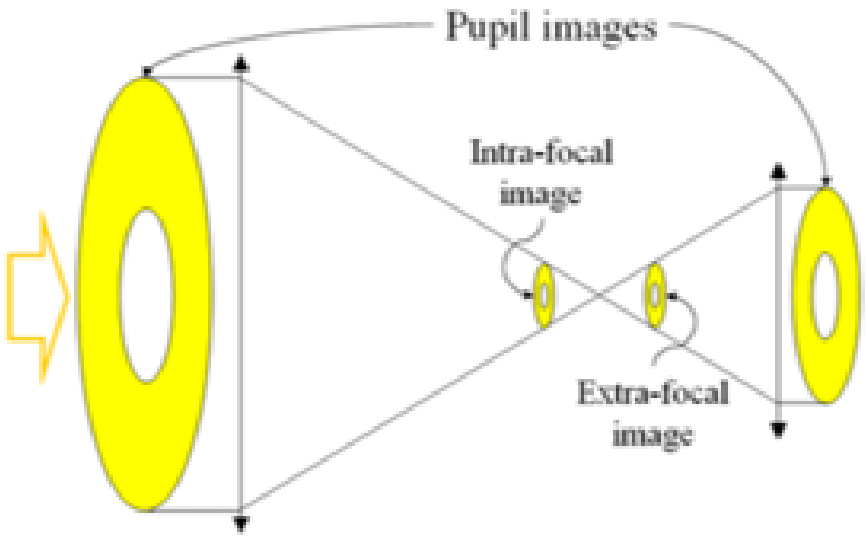

Figure 3.4: This figure depicts a curvature WFS. The image is taken from Simone Di Filippo's PhD thesis [75].

3.1.4 Pyramid Wavefront Sensor

The pyramid wavefront sensor (P-WFS) was invented by Roberto Ragazzoni in 1996 [76]. It is made of a pyramid-shaped prism placed at the focal plane of the optical system. The incoming light is divided into four separate beams by this pyramid, and each beam is directed onto different regions of a detector. This produces four different images of the telescope pupil. The intensity of each of the four images is proportional to the number of photons that reach each face of the pyramid. The distance between the centers of the pupils is determined by the focal length of the collimator and the vertex angle of pyramid, as shown in fig 3.5, and is given by the equation 3.3.

$$d_{\text{centers}} = \beta(n-1)f_{\text{ob}} \tag{3.3}$$

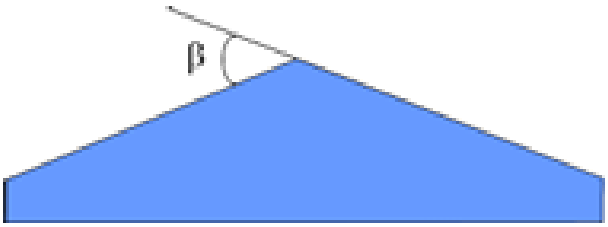

Figure 3.5: The diagram of the Pyramid Wavefront Sensor (P-WFS), showing the pyramid-shaped prism with an angle β at the tip. This prism splits the incoming light into four beams, which are directed towards different areas of a detector to measure wavefront distortions. The image is taken from Simone Di Filippo's PhD thesis [75].

The principle of the P-WFS is based on splitting the wavefront into multiple parts and measuring the differences in light intensity across the four beams for each sub-aperture.

When the wavefront is flat, the P-WFS splits the incoming light into four beams, with equal amounts of light directed to each corresponding sub-aperture. This gives uniform distribution of light across the pupil. When aberrations are present in the wavefront, the PSF at the tip of the pyramid changes, this alter the distribution of light among the sub-aperture in the four pupils observed on the detector. In the case of a simple wavefront tilt, the light focus shifts toward one facet of the pyramid. As a result, intensity of each beam becomes proportional to the number of photons hitting its respective pyramid face. This variation in light distribution allows the sensor to measure wavefront distortions by analyzing the differences in intensity between the beams [77].

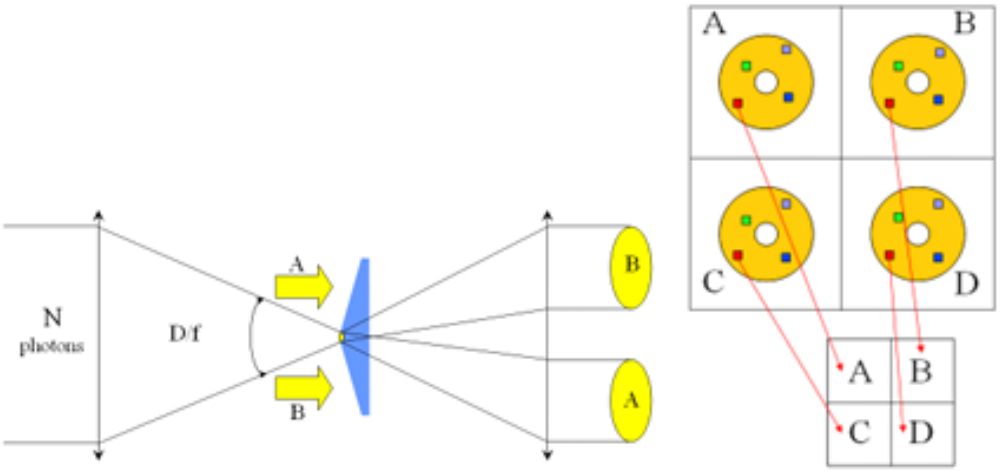

3.2 Ingot-WFS as Future Alternative

We have learned in sec 2.3.3.2 that Na-LGS is not a point reference star but it is a long time-varying cylindrical source. These Na-LGS will make up an important component of AO systems of the upcoming telescopes . With existing WFSs we face some shortcomings in handling the Na-LGS properly and utilize their full potential, for example we have seen in the previous sections how using SH-WFS and P-WFS have reduced sensitivity to first-order derivative of local wavefront. The reduction is dependent on the position of sub-aperture on the pupil and the LGS elongation.

One of the concepts behind I-WFS is the Scheimpflug Principle, describing the relation between the object plane, lens plane and the image plane. It was introduced by Carpentier in 1901 [78]. This principle describes the geometric relationship between the object plane, the lens plane, and the image plane in an optical system. It is extremely useful when the object plane is tilted or not parallel to the lens plane. This principle ensures that despite the angular misalignment, the planes can intersect along a common line, allowing for optimal placement of a detector along a plane where the entire image is in focus.

This is specially important to understand the Na-LGS system in large telescopes. The Na-LGS is formed in the mesosphere at around 80-100 km of altitude [13] and usually in large telescopes the laser is launched from a position either near the edge or center of the telescope aperture. The Scheimpflug principle becomes relevant due to the non-perpendicular angle at which the laser beam is launched into the sky. Because of this

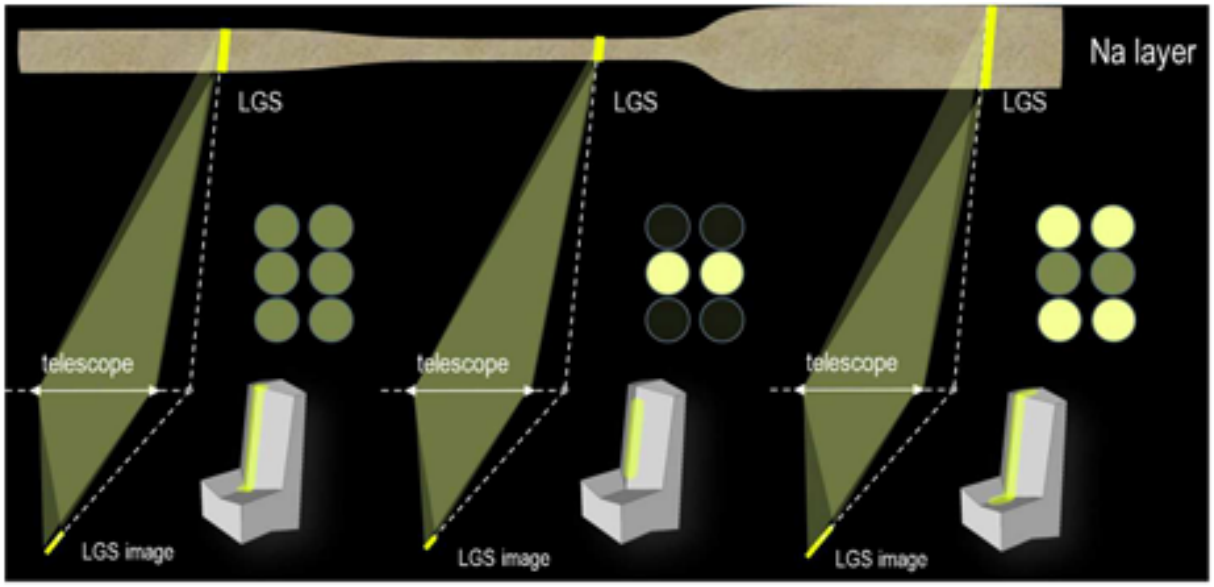

Figure 3.6: This is the initial six-face design of the I-WFS. This figure also shows how the intensity of light varies in pupils with varying thickness of sodium profile. The image is taken from [79]

geometry, the image plane of the LGS and the typical focus plane of objects at infinity are not perfectly aligned.

Understanding the Scheimpflug principle helps to solve this by ensuring that the wavefront sensor can be placed correctly on the effective focal plane of the Na-LGS image. The system can effectively correct for the elongation and distortions in the laser guide star image. This allows the adaptive optics system to capture sharp, well-defined wavefronts from the elongated Na-LGS.

Utilizing this geometrical approach tailored for Na-LGS, a new WFS was proposed by Roberto Ragazzoni in 2017 [15]. The original WFS consisted of reflective and refractive surfaces in an elongated prismatic shape, it is called the Ingot wavefront sensor (I-WFS). The shape of the I-WFS is such that it receives the light from every portion of the LGS and directs it on the detector. Initially the I-WFS was designed as a six-faced prism, as shown in fig 3.6, where each face was supposed to focus on the light from specific portion of the LGS and then guide it to the detector forming six corresponding pupils. This design had its own drawbacks related to the thickness of the LGS. The actual size of LGS varies with its thickness and due to this variation, the six-faced I-WFS might not be able to accommodate the length of the source.

To overcome the issue of length accommodation of source on WFS, another improved design was proposed by Ragazzoni in 2019 [80]. The design of I-WFS is based on evolution of the P-WFS. The new design of I-WFS, shown in fig 3.8, consists of a reflecting roof, giving it 3 faces. The roof-shaped ingot prism splits the Na-LGS into three different regions, two are reflected off from the top roof and the third region reaches the detector unperturbed by the prism, *i.e.* transmitted [81]. The three beams are then re-imaged to form three pupil images. These three pupils are called A, B and C of which A is

transmitted pupil and B and C are reflected pupils from the roof of the Ingot prism.

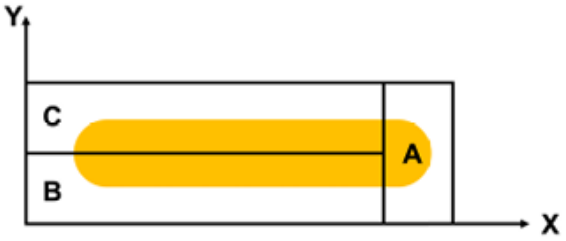

Figure 3.7: The image shows the divide of each pupil on the Na-LGS as seen on the I-WFS. The image is taken from [82].

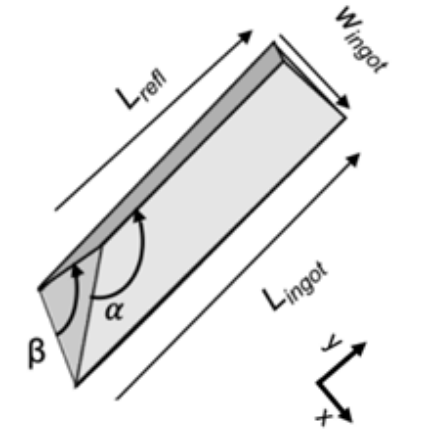

Figure 3.8: This is a schematic representation of I-WFS. Image is taken from Portaluri et al. 2020 [81].

The main advantage of this design is that it is adaptable to the time-variable size variation of the Na-LGS. To accommodate the elongated LGS, we just need a roof prism of adequate length to match the full extent of the LGS image [83]. The ratio between the flux in the transmitted pupil and that in the reflected pupils can be adjusted by moving the prism along the direction of the edge between the reflective faces, as shown in fig 3.9.

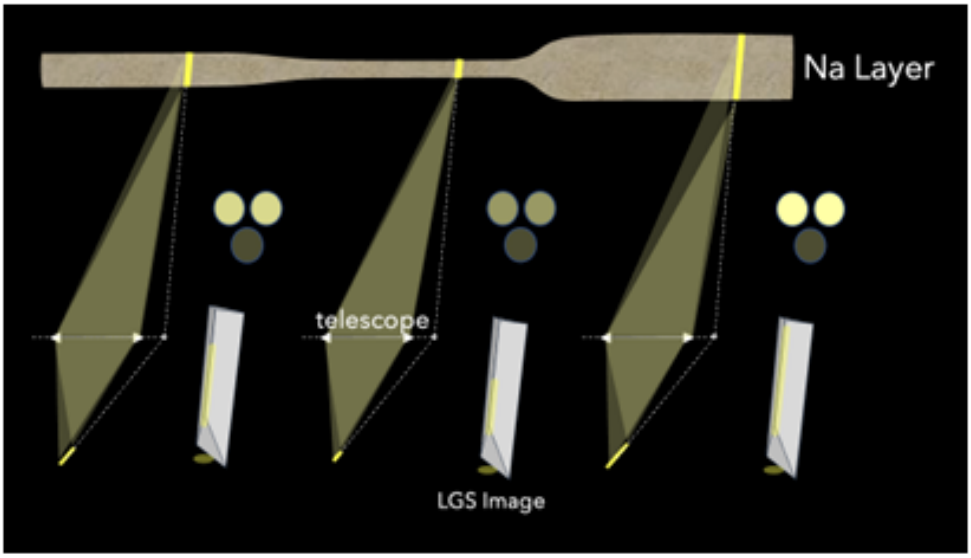

Figure 3.9: This image depicts the response of three-face I-WFS to varying sodium profile. The image is taken from Simone Di Filippo's PhD thesis.

Since the design of I-WFS is inspired by P-WFS, the process to calculate the signals is similar. The signals S_x and S_y, are defined along the x and y directions, respectively, where x represents movements perpendicular to the elongation direction and y represents movements along the elongation direction. They are given by the equations 3.4 and 3.5.

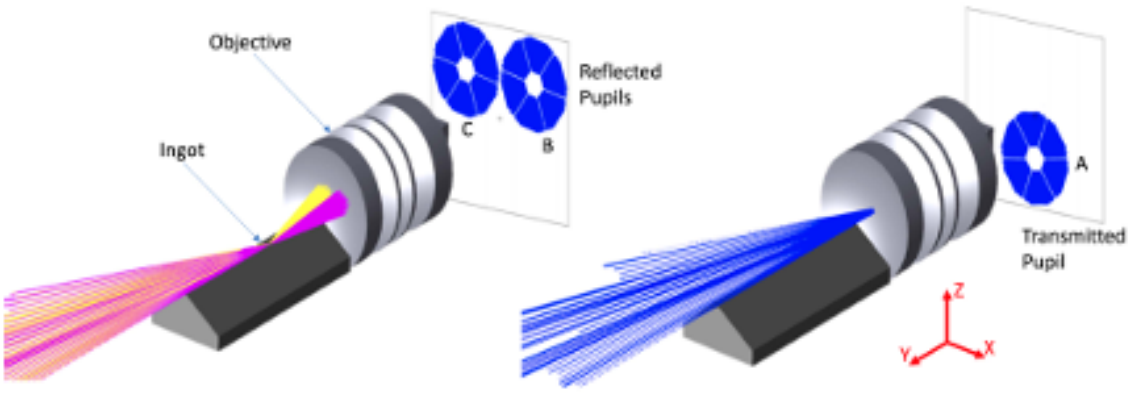

Figure 3.10: The figure depicts the ingot prism setup showing the reflected pupils, B and C, and the transmitted pupil, A captured by the detector. The image is taken from [84].

$$S_x = \frac{B - C}{A + B + C} - \frac{B_{\text{ref}} - C_{\text{ref}}}{A_{\text{ref}} + B_{\text{ref}} + C_{\text{ref}}} \tag{3.4}$$

$$S_y = \frac{A}{A + B + C} - \frac{A_{\text{ref}}}{A_{\text{ref}} + B_{\text{ref}} + C_{\text{ref}}} \tag{3.5}$$

The signals are calculated for each pixel. It is to be noted that in order to calculate the signal we subtract the reference signal calculated at the calibration position of the I-WFS [85].

In chapter 5, we will discuss about I-WFS and the bench setup in details.

4 Impact on Astronomy

As discussed earlier, currently the AO systems are being used at almost every telescope with a larger aperture than 4 m to improve their imaging capabilities [17]. Similarly the upcoming large telescopes like ELT, GMT and TMT will need advanced AO systems to correct for large FoV. In this chapter we will focus on ELT and different instruments that will be used for the first light of the telescope. We will also discuss about the fact why we need LGSs on MCAO module, specifically discussing the ELT case.

4.1 ELT: A Step Forward

The Extremely Large Telescope or ELT is currently under construction at Cerro Armazones in Chile's Atacama Desert. Situated at an elevation of 3,046 m above the sea level, it offers optimal atmospheric and climatic conditions for astronomical research. Cerro Armazones' high transparency of atmosphere and low levels of water vapor make it one of the best locations in the world for ELT like infrared and optical observation telescope [86].

The optical system of ELT is designed to deliver very high resolution and sensitivity. The primary mirror (M1) which has a 39 m diameter is composed of 798 hexagonal segments each measuring 1.5 m across and 5 cm thick. This design enables the mirror to maintain its shape under varying gravitational forces and temperatures. In addition to the primary mirror, the ELT optical design includes three other mirrors: the 4.25 m diameter secondary mirror (M2), the 3.7 m tertiary mirror (M3), and the 2.4 m adaptive optics mirror (M4). When the light radiation reaches the primary mirror, it is directed onto the convex M2 mirror, which reflects it onto the M3 mirror. Then from M3, the light passes to M4, which can adjust its shape in order to correct atmospheric distortions and telescope vibration. From here the corrected wavefront reaches the scientific instruments [87].

The ELT is equipped with several highly advanced scientific instruments each designed to perform specific tasks. Some of them are shown in fig 4.1. The main scientific instruments are:

- **MICADO:** MICADO or Multi-AO Imaging Camera for Deep Observations, is the ELT first light near-infrared imaging camera designed to work in conjunction with the adaptive optics system of the telescope. It will provide diffraction-limited imaging in standard, astrometric, and coronagraphic modes and long-slit spectroscopy at near-infrared wavelengths [89]. It will image a field of view of nearly 1 arcminute at the diffraction limit of ELT [90]. With this high-resolution, it will be capable of

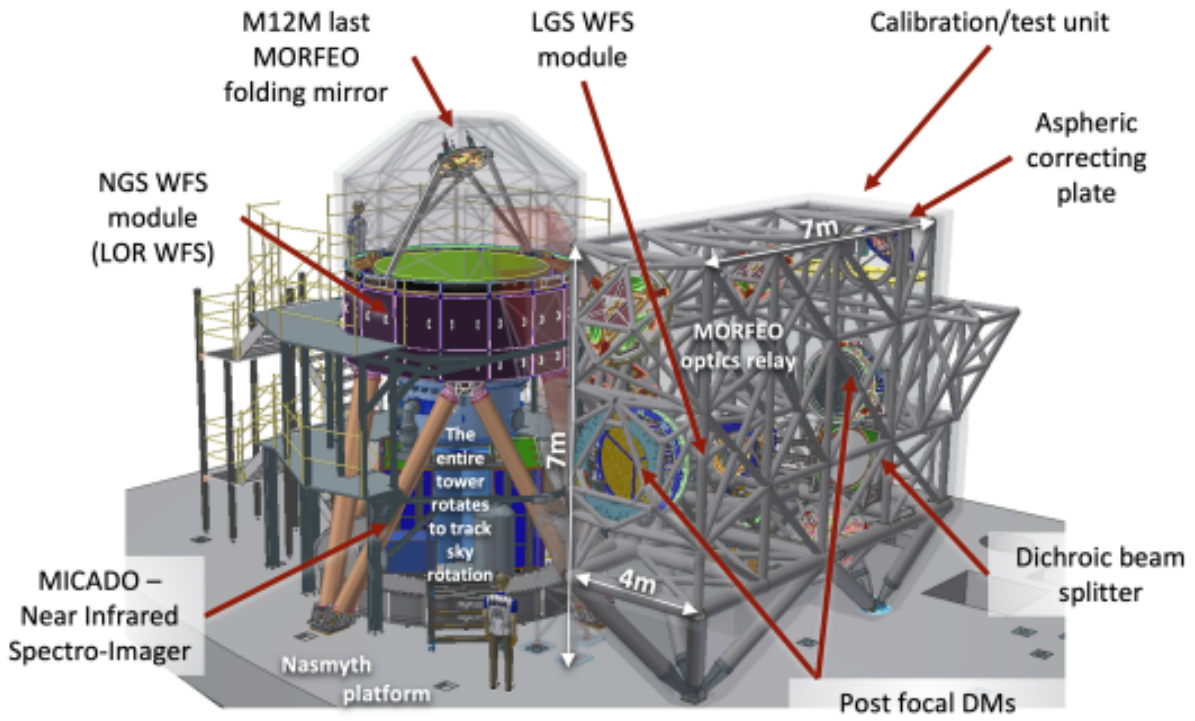

Figure 4.1: The figure shows a 3D model of the ELT Nasmyth B platform with MORFEO and MICADO. The image is taken from Busoni et al. 2023 [88].

capturing faint objects that were previously out of reach for ground-based observatories. MICADO will be the first instrument to be installed at ELT and will operate in SCAO mode, focusing on limited scientific cases. After that, it will be coupled with MORFEO enabling the MCAO correction and exploiting its capability in all the scientific topics.

- **HARMONI:** High Angular Resolution Monolithic Optical and Near-infrared Integral field spectrograph or HARMONI is an instrument that combines imaging and spectroscopy capabilities covering a wide range of wavelengths from 470nm to 2450nm with resolving powers from 3300 to 18000 [91]. It will provide detailed spectral information for every pixel in the field of view, making it ideal for studying the dynamics and chemical composition of stars, galaxies, and nebulae.
- **ANDES:** Armazones High Dispersion Echelle Spectrograph or ANDES which was formely known as HIRES is designed as a modular spectrograph with two separate sections—one for visible light and the other for near-infrared. It can capture light from a wide range of wavelengths from 0.35 to 2.4 μm at a very high resolution R 100,000 [92].
- **METIS:** Mid-infrared ELT Imager and Spectrograph or METIS, is a mid-infrared instrument capable of imaging, coronagraphy, and high-resolution spectroscopy. It can image in the L/M band (3–5 μm) using medium-resolution slit spectroscopy and has a coronagraph for high-contrast imaging. For the N band (7.5–13.5 μm), it offers low-resolution slit spectroscopy and high-contrast imaging using the coronagraph. It also has a high-resolution spectroscopy mode in the L/M band (R $\approx$ 100,000) using an integral field unit (IFU), which can cover a wider range of wavelengths with the

help of a coronagraph placed in front of it. The instrument's main science focus is on the detection and characterization of young exoplanets and proto-planetary disks [93].

We can understand the capabilities of ELT from the fact that the ELT will gather 15 times more light than the Gran Telescopio Canarias and combined with AO, it will be able to produce images with much higher resolution. The advanced optical system of ELT and collection of scientific instruments are designed to provide a clearer and deeper view of the universe than ever before. Together the above mentioned instruments make the ELT an instrument that will help to answer important questions about our cosmos and lead to new discoveries. We will discuss some of these scientific cases in section 4.3.

4.2 MORFEO

Like other telescopes, the ELT is also affected by Earth's atmosphere, which distorts the light entering the telescope. To overcome this challenge, the ELT is equipped with an advanced AO system that compensates for atmospheric turbulence, allowing it to achieve near-perfect image resolution. The AO system on ELT is called MORFEO (Multi-conjugate adaptive Optics Relay For ELT Observations) [94].

A key component of this system is the ELT's M4 mirror which is the largest adaptive mirror ever built with over 5,000 actuators that can reshape it thousands of times per second. In addition to the M4 mirror, MORFEO is equipped with two more deformable mirrors (928 mm and 1225 mm diameter) that work together with M4 to correct atmospheric turbulence at different altitudes. This system, combined with the MICADO camera, enables the ELT to capture extremely detailed images of celestial objects, even in areas of the sky where there is no natural guide star to be used for correcting the atmospheric distortion with the SCAO system. MORFEO will use a combination of 6 LGSs and 3 NGSs to give a uniform correction over large FoV providing the corrected beam to MICADO. It is required to provide a uniform correction over a 1-arcmin field of view, with a Strehl Ratio of 30% (goal 50% in best conditions) in K band under ESO's median atmospheric conditions and with 50% sky coverage, allowing MICADO to exploit the full resolution potential of the ELT in 0.8 - 2.4 μm wavelength coverage [88].

4.3 Science Cases of MORFEO

ELT with its large aperture of 39 m and highly advanced instruments is expected to achieve an angular resolution of approximately 8 mas in the J-band and 14 mas in the K-band when operating at its diffraction limit [87]. This kind of high resolution will enhance the scope of new discoveries in various fields of astronomy. The main science areas that the ELT will focus on includes planets and planetary systems in the Solar System and outside, first generation stars, black holes specially focusing on Sagittarius A, galaxies and cosmology and dark matter. Some of these cases are discussed in detail below, using the White Book of MORFEO [95] as a reference.

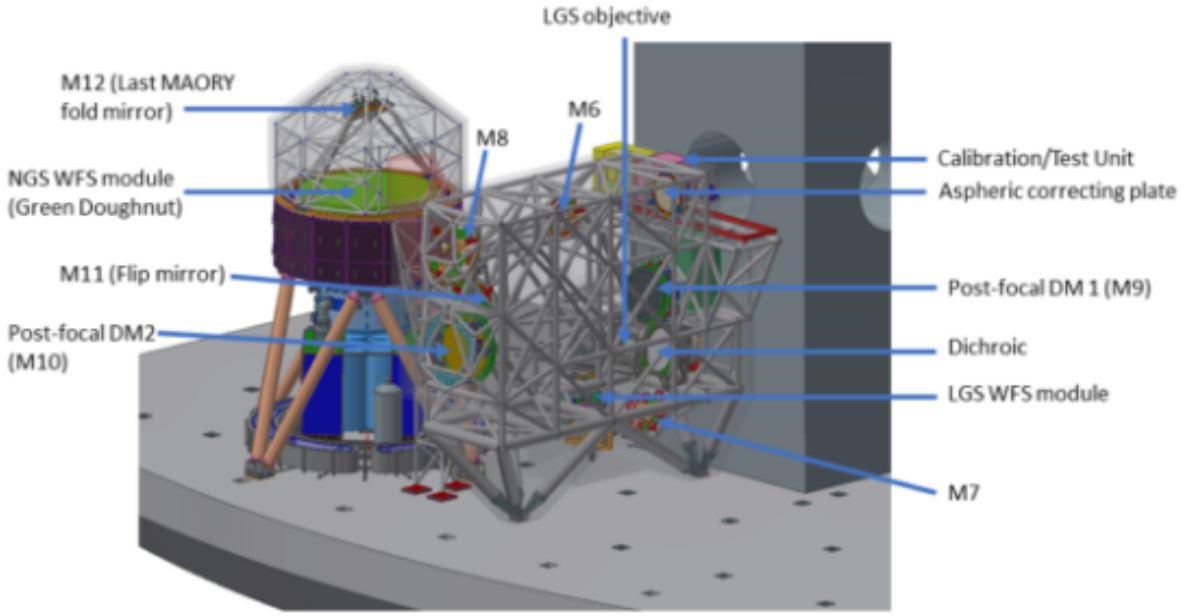

Figure 4.2: The image is a schematic representation of MOREFEO. The main components of MORFEO are a NGS WFS module to correct the aberrations with NGS, LGS WFS module that utilize 6 Na-LGS and 3 deformable mirrors. It will work in conjunction with MICADO, the camera. The image is taken from [94].

- **Bodies in Solar System**
  The ELT, equipped with MCAO, will be able to resolve and study around 950 asteroids larger than 40 km in size, analyzing their shapes and compositions. It will also be used for resolving faint asteroids and Kuiper belt object with magnitudes below 15 in the H band. Another key target in this list will be Pluto, whose unexpected geological activity at low temperatures raises questions about its internal processes.

- **Massive Planets in Young Protoplanetary Disks**
  The combined capabilities of MORFEO and MICADO will enable the ELT to search for protoplanets around young stars, even those with magnitudes as low as 13-14 in the visible range. MCAO will also enable high-contrast imaging in regions as close as 10-50 AU from the central star, providing an opportunity to investigate planet formation processes at distances where the development of gas giants and other planetary bodies is usually expected.

- **Population-III Stars**
  A more detailed study of old stellar populations can be done with ELT. The strength of He-II in galaxies observed at redshift > 3 could confirm the presence of population-III stars.

- **Astrometry**
  Astrometry will prove to be a highly useful tool to characterize the physical and orbital properties of astroids in the Solar System. It will eventually help astronomers understand the Solar System better. Also when the high quality imaging by MORFEO + MICADO is used with astrometry and radial velocity, it will deliver unique results to understand the giant planet population.

- **Young Stellar Population**
  Young stellar populations in the Magellanic clouds can be well studied with ELT with narrow band filters. This can be eventually used to derive the luminosity function, deriving initial mass function which can help understand the star and planet formation processes.

- **IMBH in Globular Cluser**
  MICADO and MORFEO together can achieve an astrometric precision of 0.05 mas. Globular cluster (GC) like 47 Tucanae can be the observed for detection of a Intermediate-Mass Black Hole (IMBH). Detection of IMBH in these cluster could provide answers to the formation of super massive black holes and dynamics and evolution of GC.

- **High-Redshift Galaxies and the Early Universe**
  One of the key scientific goals is to explore galaxies at redshift greater than 10, during the epoch of re-ionization. The use of near-IR filters will also facilitate the precise measurements of spectral slope and properties of high redshift galaxies.

4.4 Need of Laser Guide Star

As discussed in the previous section, MCAO at the ELT will utilize both NGSs and LGSs to achieve better correction over a large FoV. Using only NGS limits the capabilities of a telescope with large aperture.

The distribution of bright stars suitable for use as NGS is not uniform across the sky. This uneven distribution limits the use of NGS for correcting distortions, especially in the star-poor regions of the universe where fewer stars are visible.

We know MICADO on ELT will operate in both SCAO and MCAO mode, the limiting magnitude for both AO techniques are < 16 and < 22 respectively in R band. SCAO will use a single NGS while MCAO will use three NGSs and 6 LGSs. To understand how many NGSs are available for deep-field observation to both AO techniques, we used the same technique described in Portaluri et al. [96].

We focused on one of the main fields where ELT will make the difference in terms of new discoveries: the detection and analysis of the high-redshift universe. We all know that to "see" new galaxies (i.e. far/faint), we need to exploit the AO system in all its potentiality, pointing in very dark regions of the sky. This could be a limit for the applicability of the AO correction, so in order to have the idea of accessibility of deep-fields, we investigated 8 famous surveys, reported in the table 4.1, selecting those that would be visible from the ELT coordinates by using STAROBS [1].
Therefore, we performed a simulation using TRILEGAL [97], a population synthesis code that simulates the stellar photometry of our Galaxy, giving as input parameters, the information about the coordinates in the sky (RA and dec), the MORFEO technical field of view (120 arcsec) and the photometric band used by the ELT AO sytem (R band). We looked for how many stars could be available in those area of the sky in order to under-

[1] STAROBS

stand if the SCAO is applicable (if there are object with the already discussed magnitude limit) or whether we need for the MCAO correction. The number of stars available for SCAO and MCAO for deep field observations are reported in the table 4.1.

Survey Name References (surveys)	**RA** [^{o}]	**DEC** [^{o}]	**SCAO**	**MCAO**
NDWFS-Bootes [98]	217.500	34.5000	0	8
NDWFS-Cetus [98]	31.8708	-4.7356	4	37
CDF-S [99]	53.1167	-27.8083	2	7
GOODS-S [100]	53.1250	-27.8056	1	14
SubaruDF [101]	201.1625	27.4906	4	11
COSMOS [102]	150.1167	2.2058	3	55
HUDF [103]	53.1625	-27.7914	0	2
CFHTLS-D2 [104]	150.1167	2.2083	2	50

Table 4.1: The table shows the most studies deep field surveys by GMCAO. They are mentioned with their right ascension and declination of their central pointing and column 4 and 5 gives the number of stars in the limiting magnitude for SCAO and MCAO, respectively.

From the results it is clear that the number of NGS available for deep field observations are limited for SCAO and with such small number of NGSs, astronomers can not take full advantage of ELT. We also highlight that the MCAO mode of MORFEO (using both NGS and LGS) provides clear advantage with a uniform SR over complete FoV, as shown in fig 4.3 and this would be the preferable choice for the majority of scientific investigations. With this analysis, we pointed toward the direction on the fact the performance of the MORFEO system is crucial for the ELT and our project on a new WFS that could improve the AO correction system is absolutely timely and worthily. Given also the difficulties and problems that a SH-WFS operating on an ELT will have with the Na-LGS source, as discussed in section 3.1.2, the I-WFS will be a highly suitable alternative. Further tests and simulations regarding the sensitivity and linearity of the I-WFS when dealing with aberrated wavefronts are still necessary and specially a direct comparison of the performance of the I-WFS with other sensors is still missing. However, the tests conducted on the I-WFS until now are promising in showing the abilities of this sensor in sensing the entire 3D volume of the Na-LGS.

In the next chapter we will go through some of the tests conducted on the I-WFS and based on the results understand its characteristics in response to the varying Na-LGS profiles.

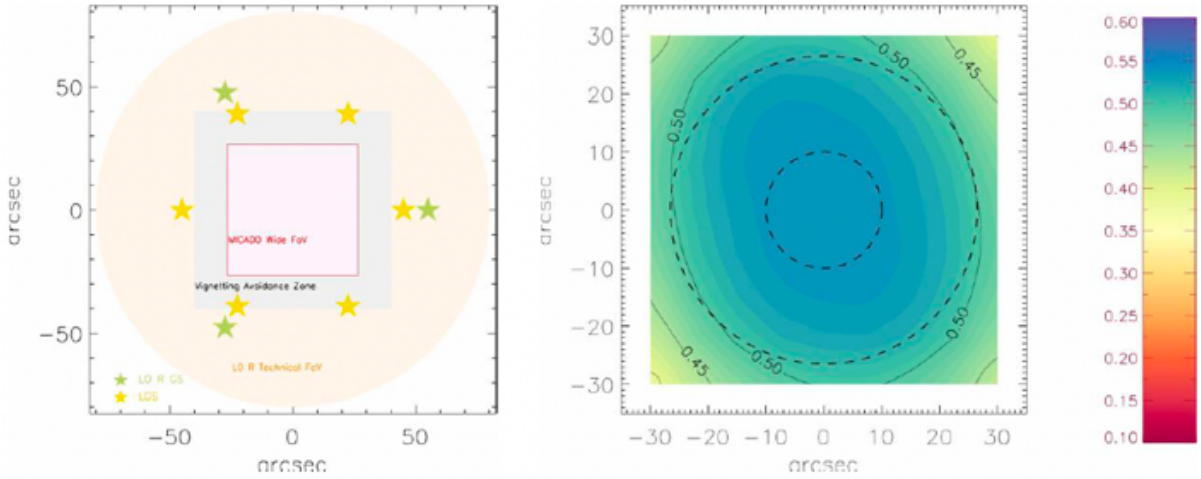

Figure 4.3: The figure on the left shows the MICADO wide FoV with a white square box, blue box represents the vignetting avoidance zone and the pink area shows the low resolution technical FoV. In the same image, yellow stars show the LGS and green represent the NGS. Using both NGS and LGS, MORFEO SR map in K band is shown in the figure at right. The image is taken from private communication.

5 Ingot Test Bench Insights

The Ingot-WFS test bench located at INAF-OAPD serves as a testing ground for Ingot in mimicking realistic parameters for and ELT telescope. In this chapter, we will provide a detailed overview of the test bench setup, highlighting the components and their roles in ensuring accurate and reliable testing. We will examine the tests conducted over the past few months, analyzing the methodologies used and the outcomes achieved. Finally, we will discuss these results and discuss their implications for future tests.

5.1 The Ingot Bench

The Ingot test bench is made by several optical and mechanical components. The setup has been organized so that the LGS can be simulated and imaged using the Ingot-WFS with a camera.

The bench, shown in the fig.5.1, is set up to closely replicate the large telescopes in the future that include:

- The ratio between the separation of the LLT and the diameter of the entrance pupil.
- The dimensions of the image on the Ingot-WFS prism.
- The telecentric nature of the image space on the Ingot-WFS prism.
- The aspect ratio of the LGS, which compares spot elongation to the Full Width at Half Maximum (FWHM).

The current optical layout, shown in fig.5.1, of the Ingot-WFS bench, is composed of the following components:

- **OLED Screen:** An OLED is used on the setup that is used to replicate the Na-profiles for testing. OLEDs have been the choice of the group because there is no emission recorded when its pixels are turned off, it is well explained in sec.5.3.4.2. The OLED is mounted on a stage that is briefly described in the sec.5.1.2.
- **Collimating Achromatic Doublets**: We use two collimating achromatic doublets, each with a focal length of 200 mm. One of the doublet is used for the incoming LGS light, and the other one is used to refocus the light onto the Ingot prism.
- **Diaphragm**: The system includes a diaphragm that serves as the aperture stop or

pupil, with a clear aperture of 25 mm. Positioned to ensure image space telecentricity, it is located at the focal point of the camera doublet.

- **Pupil Re-imager**: This component consists of a wide-aperture photographic objective with a focal length of 50 mm, used for re-imaging the pupils onto the camera.

- **Ingot Prism**: The Ingot prism is made out of a hexagonal light pipe, which is commonly used for beam homogenization. Its external surfaces are aluminized to create a reflective roof with a 120-degree apex angle, to match the pupil separation requirements of ELT.
  The Ingot prism is mounted on a H-811.I2 6-Axis Miniature Hexapod from Physik Instrumente, shown in fig.5.2(b), more about the positioning system is explained in sec.5.1.1. Hexapod is used to align the Ingot prism to the LGS.

- **Camera**: The camera in use is the Prosilica GT3300 from Allied Vision, featuring an 8-megapixel CCD sensor with 5.5 µm pixels. The exposure time for capturing frames has been configured to 1250 ms. For computational purposes, the captured frames are subjected to (2,2) binning.

- **Stray Light Suppression**: To reduce the effects of stray light, a black cover has been added over the test bench as shown in fig.5.2(c)

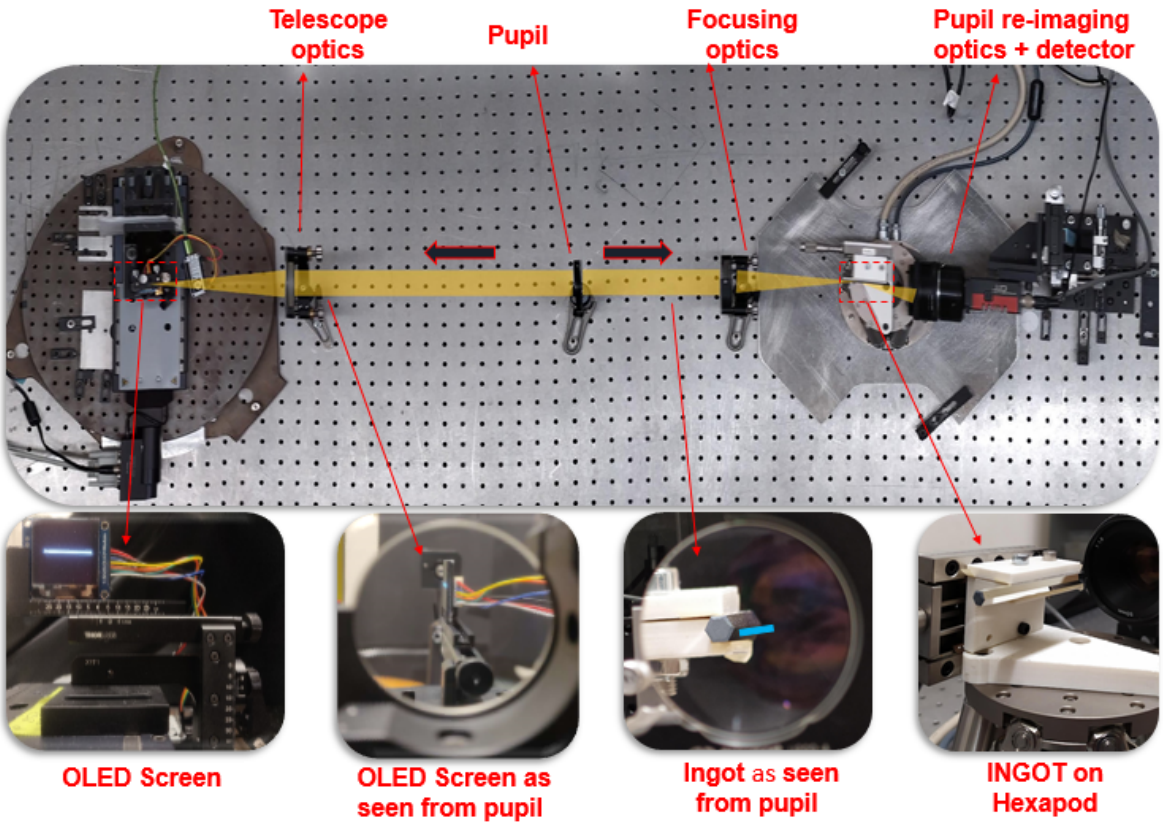

Figure 5.1: Ingot bench with the Optical Components mentioned

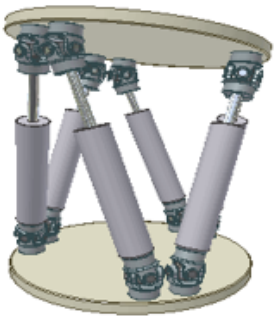

((a)) 811.I2 6-Axis Miniature Hexapod from Physik Instrumente

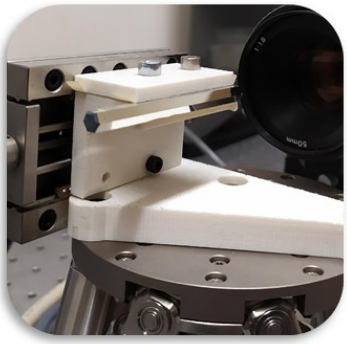

((b)) Hexapod with Ingot mounted on Top

((c)) Ingot Bench and other Reflective Surfaces Covered to avoid Stray Light

Figure 5.2: Components from the Ingot Bench

The Ingot-WFS bench is made with readily available hardware components in the lab, except for the hexapod which This optical bench is a 1:1 re-imaging relay, which means that that the source on the OLED screens is re-imaged with the same size on the Ingot prism.

5.1.1 Hexapod and Its Movements

Hexapod is one of the most important tool on the ingot bench. As discussed earlier, it is a H-811.I2 6-Axis Miniature Hexapod from Physik Instrumente on which the Ingot prism is mounted. It provides 6 degrees of freedom that are called as X, Y, Z, U, V and W, as shown in fig.5.3. The whole movement of Ingot prism depends on the hexapod's pivot point which has been set at the tip of the ingot prism and based on this pivot point, a coordinate system is defined for the movement of hexapod along the 6 degrees of freedom. X, Y and Z define the coordinates of movement and U, V and W defines the angular rotation around the coordinate axis. The movement along these axes is The ranges and resolution of hexapod [1] along all the axis are given in the table 5.1.

Table 5.1: Range and Resolution of H-811.I2 6-Axis Miniature Hexapod.

Axis	**Range**	**Resolution**
X	± 17 mm	0.2 µm
Y	± 16 mm	0.2 µm
Z	± 6.5 mm	0.08 µm
U	± 10 °	2.5 µrad
V	± 10 °	2.5 µrad
W	± 21 °	5 µrad

[1] The values have been taken from the Instrument Datasheet.

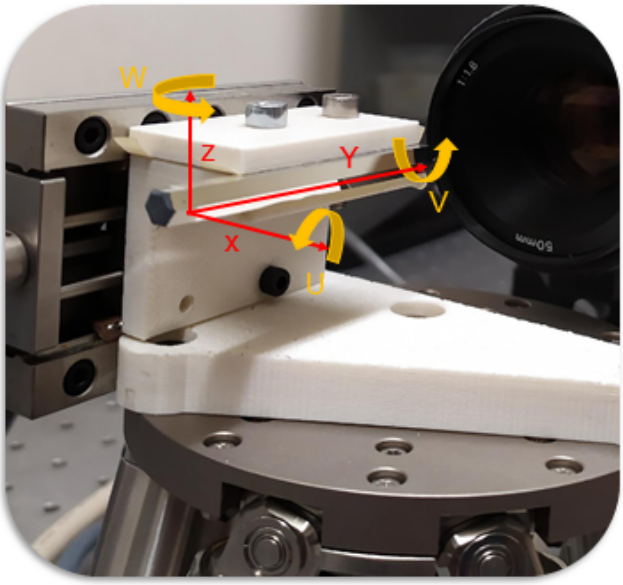

Figure 5.3: Image shows the Ingot prism mounted on the hexapod. This image also displays the movement axis X, Y and Z.

5.1.2 Stage for OLED Screen

The OLED screen is mounted on a stage designed for positioning of Na-profile to achieve ELT parameters like distance and angle. Circular rotating stage makes the base, which allows angular adjustment of the source with respect to the optical path. Currently it is set at an angle of 2°. Above the circular stage, a horizontal stage facilitates movement along the X direction of hexapod. Providing better adjustment on the setup. It is shown in fig.5.4(a).

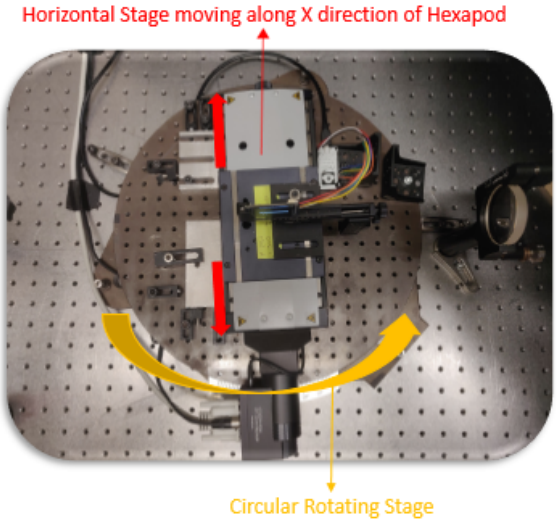

((a)) Rotatory stage used for rotation of screen and as base of other stages.

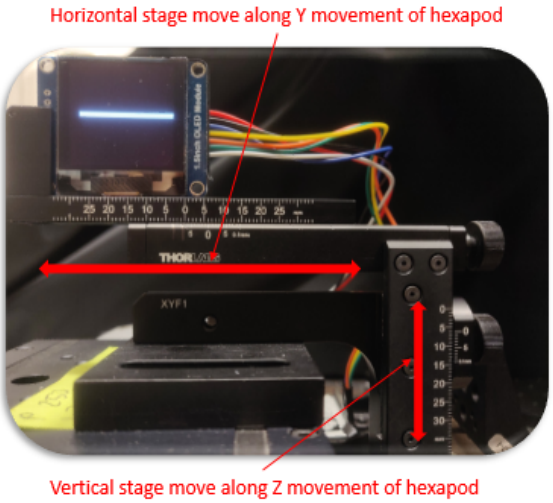

((b)) Stage from Thor labs on which OLED is mounted.

Figure 5.4: Components from the Ingot Bench

On top of the horizontal stage, there is a versatile stage from Thor Labs that enables movement in along the Y and Z directions. This stage allows the OLED screen to move horizontally towards and away from the Ingot prism, corresponding to the Y direction movement of the hexapod. The vertical movement with respect to the setup helps to set a position of Na profile in the Z direction of the hexapod. Currently both horizontal and vertical scales are set at 5.1 mm, as shown in fig.5.4(b) This multi-axis configuration ensures that the OLED screen can be precisely positioned for seamless and optimal functionality of experimental setup.

5.2 Calibration and Alignment Procedures

Before the Ingot test bench came to life several simulations were done to understand the Ingot-WFS performance and the three pupil shape. All this gave us understanding to set up the bench and develop procedures that exist today for testing of Ingot-WFS. It includes procedures like pupil analysis procedure, calibration procedure and the alignment procedure.

5.2.1 Pupil Analysis Procedure

When the light from the LGS on the OLED is directed to the Ingot prism, it is split into three distinct beams. One of these beams is transmitted straight through the Ingot prism, while the other two are reflected by the Ingot prism's sides. All three beams eventually reach the detector, where the final image is captured and then analyzed using a Python script. The image, as we know, consists of 3 pupils in round shape. When these pupils are analyzed using the python script, it takes into account the coordinates, given in number of pixels of the camera. These coordinates are used to to define the location (center: x and y coordinates) and the size (radius: r) of all the pupils and given as an array (x,y,r). Based on the pupils detected, the procedure can run in two different ways, they are:

- **Autodetection True**, used when all the three pupils are detected. It employs Canny-Edge algorithm[105] and Hough Circle Transform[106] to identify the coordinate position (in pixels) and radius of the 3 pupils.
- **Autodetection False**, uses some already defined set of coordinates for the centers and radii of all the three pupils. It is used by the python code when all the pupils are not detected by the Canny-Edge algorithm. These defined coordinates are the expected coordinates where the aligned pupils would be located. During my work the set coordinates for the pupils have been:

$$A = (431., 179., 131.)$$
$$B = (293., 419., 131.)$$
$$C = (570., 419., 131.)$$

These set coordinates can be manually defined by the user and set as preferred. Both the detection procedures are run by the same python script. It starts with Autodetection True but if it fails to detect the three pupils, the Autodetection False is used with the defined coordinates.

Once the coordinates are obtained, the pupils are extracted, rotated and flipped to compensate the rotation effect by the ingot face. Following this the three pupils are averaged. The final pupil so found are used to compute the signals at each pixel with equations defined in previous chapters. The complete procedure is explained in details in Difilippo et.al 2022 [75].

5.2.2 Calibration and Alignment Procedure

The alignment procedure and the calibration procedure are two different procedures well explained in Radhakrishnan Santhakumari et al. 2020[107], Simone Di Filippo's PhD thesis[108] and Tania Sofia Gomes Machado's thesis[18] work.

Before jumping to the alignment and calibration procedure, it is important to know that we utilize six specific parameters known as observables. These observables depend on the flux and position of the three pupils and form the basis for assessing and correcting the ingot's alignment. The six observables that help do calculations for calibration and alignment procedure and quantify the alignment are:

- **Observable 1**, is calculated by the flux difference between pupils C and B, normalized to the combined flux of all three pupils:

$$\frac{(C-B)}{(A+B+C)} \tag{5.1}$$

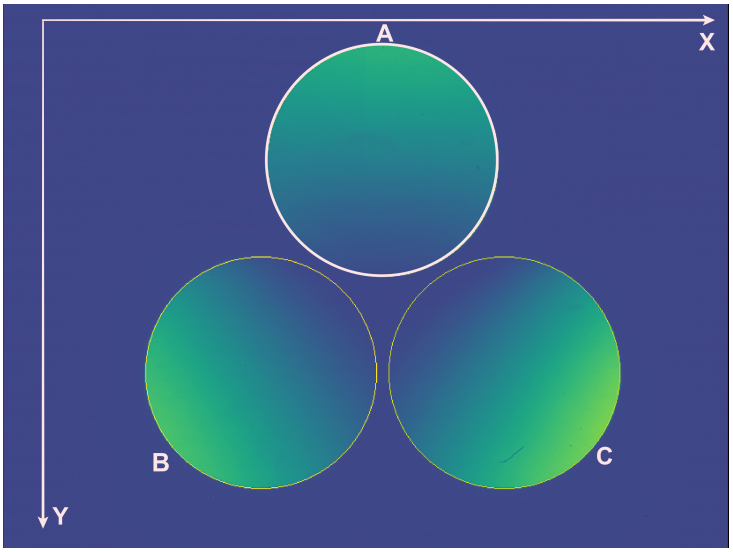

Figure 5.5: Observable 1 and Observable 2 calculated using flux of 3 pupils

- **Observable 2**, is calculated by normalizing the difference between the flux of transmitted pupil A and the combined flux of reflected pupils B and C, normalized to the combined flux of all three pupils:

$$\frac{A-(B+C)}{(A+B+C)} \tag{5.2}$$

- **Observable 3**, is calculated by the distance between the centers of pupils A and B, measured in pixels, is given by:

$$A - B = \sqrt{(X_A - X_B)^2 + (Y_A - Y_B)^2} \tag{5.3}$$

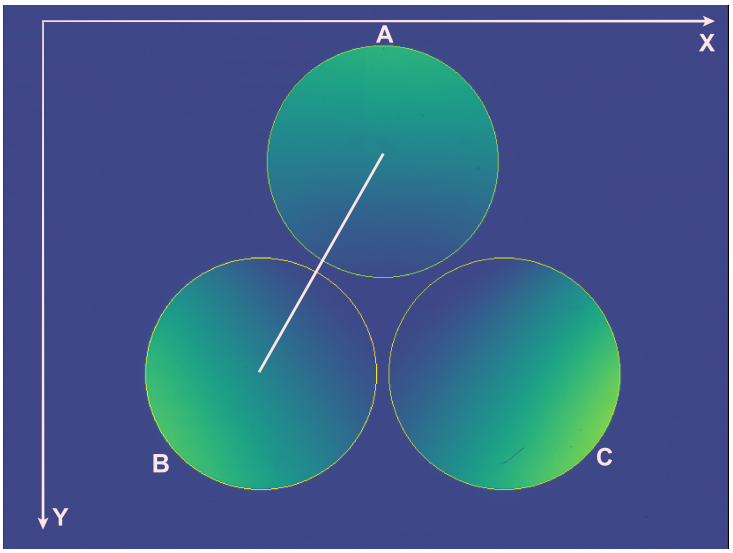

Figure 5.6: Distance between the center of Pupil A and Pupil B : Observable 3

- **Observable 4**, is calculated by the distance between the centers of pupils A and C, measured in pixels, is given by:

$$A - C = \sqrt{(X_A - X_C)^2 + (Y_A - Y_C)^2} \tag{5.4}$$

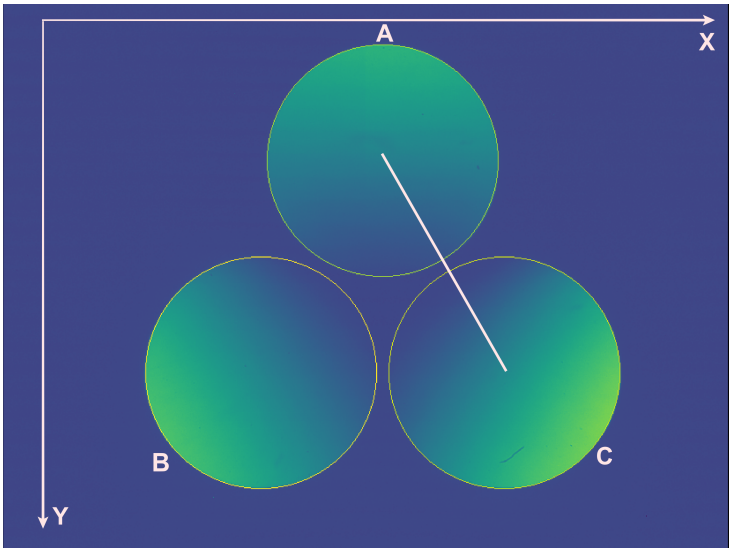

Figure 5.7: Distance between the center of Pupil A and Pupil B : Observable 4

- **Observable 5**, The vertical distance between the centers of pupils B and C, measured in pixels, is given by Y_B - Y_C.

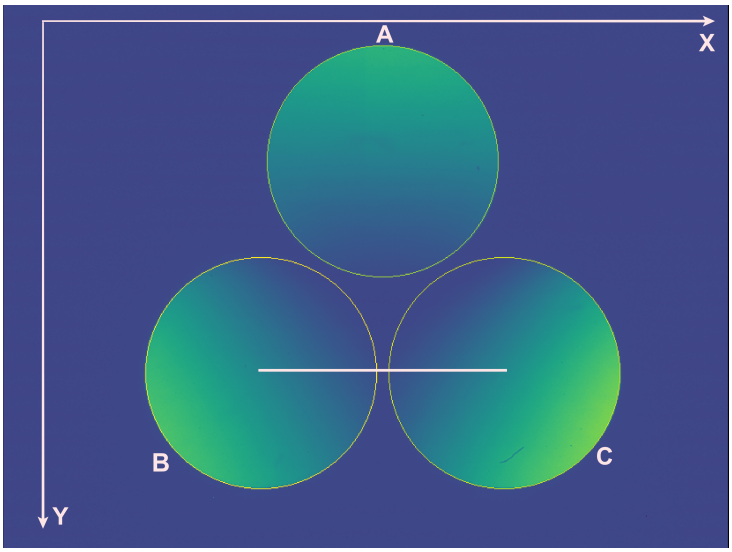

Figure 5.8: Observable 4 that checks if the centers of Pupil B and C falling on same row.

- **Observable 6**, is calculated as the difference of the sum of S_x in two regions that corresponds to the top-left (region 1) and top-right (region 2), as shown in fig.5.9.

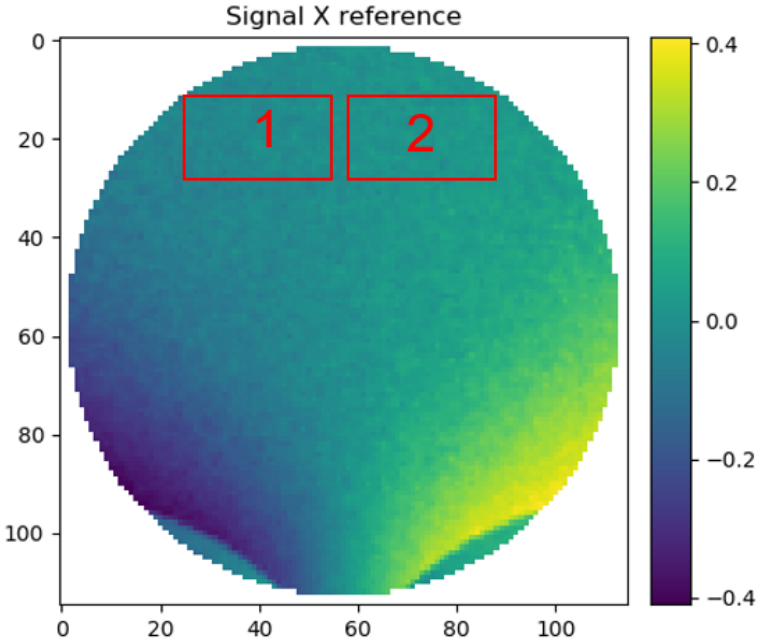

Figure 5.9: This is the S_X signal being calculated using the difference between the average of two red boxes shown here.

All these observables have target values and boundaries around the target values that have to be met for the Ingot to reach alignment. The values have been mentioned in the table 5.2.

Observables	**Target Values**	**Boundary Values**
Flux (C-B)/(A+B+C)	0%	±0.5%
Flux (A-B-C)/(A+B+C)	-33.3%	±0.4%
Distance (A - B)	277 pixels	±1 pixel
Distance (A - C)	277 pixels	±1 pixel
Vertical Distance ($Y_B - Y_C$)	0 pixels	±1 pixel
$\overline{S_{x1}} - \overline{S_{x2}}$	0	0.1%

Table 5.2: Target values and boundary values for each observable.

To perform a test, we run the calibration procedure, followed by the alignment procedure but if the parameters of tests are similar, in that case the calibration taken earlier can also be used. This is because the calibration procedure during the run creates two matrices which are called Interaction Matrix (IM) and Calibration Matrix (CM). The matrices are made to adjust the hexapod's six degrees of freedom based on discrepancies between measured observables and their target values. The creation of CM and IM employs a linear approximation which is similar to the one used in AO closed-loop systems. The two matrices are calculated in the following way:

1. To obtain the calibration we start with the hexapod in a position close to the identified aligned position to expedite the computation and have a more reliable matrix.
2. From here we calculate the six observables that are defined in the table 5.2.
3. It is followed by moving the hexapod in each of 6 degrees of freedom. The movement along each axis is a push and a pull. At every step a set of observables is calculated i.e. along each axis there will be two set of observables calculated, one during the push and other during the pull. Push is called positive degree of freedom and pull is negative degree of freedom.
4. For each degree of freedom, we calculate the difference between the observables obtained from the positive and negative degree of freedom with respect to those computed in step 2.
5. The results from step 4 are then used to construct the IM. The two IMs (one from the push and one from the pull) are combined into a single IM as the average of the two matrix, shown in fig.5.10, This final IM is pseudo-inverted to produce the CM.

We put to use this calibration to reach the alignment position. We initiate the alignment procedure with an initial movement of the hexapod, which is considered the 0^{th} iteration. From this iteration, we use an extraction algorithm that computes the observables from the three pupils of the ingot. These observables are then compared to predefined target values, as mentioned in Table 5.2. If the observables fall within the boundary values of the target observables, the system has reached an aligned position and must remain within these boundaries for two additional iterations, i.e., the ingot must stay in the aligned position for three consecutive iterations to be recognized as aligned. If this condition is satisfied, the process terminates. If not, the CM is used to calculate a new position for the hexapod, which then moves accordingly. It is to be noted that all the six axis of movement on hexapod are moved simultaneously to reach the computed aligned position.

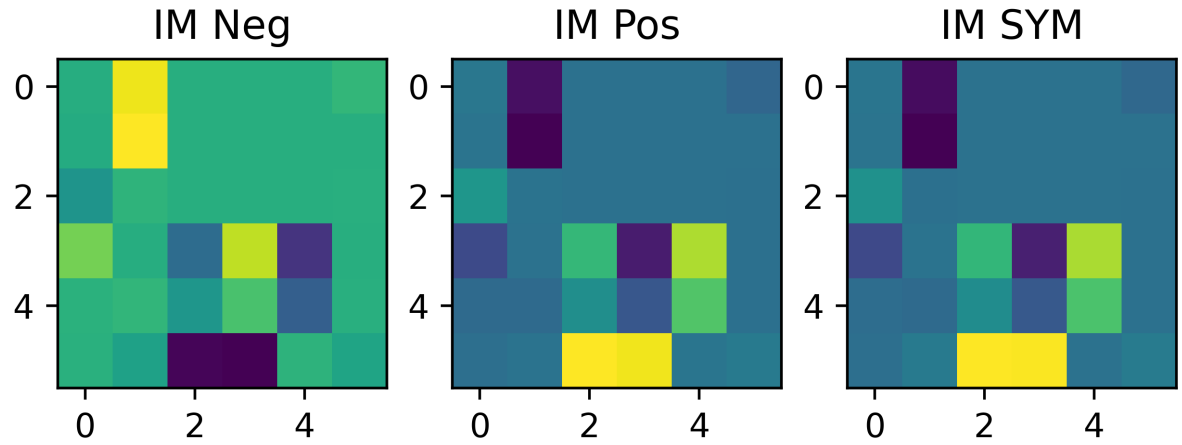

Figure 5.10: Interaction Matrix

This procedure repeats, with continuous checks against the boundaries to ensure proper alignment.

We use a python script to manage these iterations with a while loop. The script handles the iteration process, checking if the alignment criteria are met after each movement of the hexapod.

The alignment procedure goes on for 40 iterations unless the Ingot is aligned to the LGS. If the Ingot is not aligned after 40 iterations, a new calibration is automatically performed to obtain a fresh CM, using the current source displayed on the screen. This newly generated CM is temporary and used only for the ongoing alignment process. This re-calibration step is conducted only once. If an additional 40 iterations with the temporary CM still fail to achieve alignment, the system exits the loop and is flagged as misaligned.

5.3 OLED Screens

There was requirement of a screen that could replicate the Na-profiles on it. To meet the requirements the group opted for an OLED which stands for Organic Light Emitting Diode. Initially, an OLED SSD 1306, which we call Old screen, was used for initial testing of all the procedures for Ingot-WFS setup, but it could not replicate the LGS with varying contrast, which are detailed in the following subsection. So, a different OLED model, the SSD 1327, we call New screen, was acquired and installed on the Ingot test bench alongside the previously used screen. Thus, when I began my work, there were two screens on the bench, both are thoroughly described below.

5.3.1 Old Screen: SSD 1306

Old screen is an OLED with 128x64 pixels in dimensions. The size of each pixel is 0.15x0.15 mm^2 and the pitch size is 0.17x0.17 mm^2. We use a bitmap written in C#, to produce the LGS on the old screen. This bitmap is made up of a 16×64 matrix, with each entry represented in hexadecimal format. Each entry corresponds to a block of 8 adjacent pixels. Therefore, instead of having 128 entries for the 128 columns, there are

only 16 entries per row, with each entry representing a set of 8 pixels in that row.
But controlling the LGS profile on the screen by making changes in the code and uploading to Arduino takes some time. To resolve this issue, a function has been integrated with the python script. This has allowed seamless control of the old screen from the python script itself.
In the python script, the function is defined by a string **(VS, TU, TD, HS, LL, LR, #D, C)**, which sends the command directly to Arduino. The characters on the string are:

1. **Vertical Shift (VS)**: This represents the displacement of the source's center in rows, where negative values move down and positive values move up with respect to the center of the screen.
2. **Thickness Upwards (TU)**: It is the number of extra rows above the source's center.
3. **Thickness Downwards (TD)**: It is the number of extra rows below the source's center.
4. **Horizontal Shift (HS)**: Displacement of the source's center in columns, where negative values move left and positive values move right with respect to the center of the screen.
5. **Length Leftwards (LL)**: It is the number of extra columns to the left of the source's center.
6. **Length Rightwards (LR)**: It is the number of extra columns to the right of the source's center.
7. **Discontinuities (#D)**: It shows the number of random vertical column interruptions, ranging from 0 to 7.
8. **Contrast (C)**: It helps to adjust the brightness of the display, ranging from 0 to 255.

These parameters control the LGS on the screen.
On the Old Screen, we have used two different uniform sources. They are:

1. **Standard Source**: This source, on the python script, is defined by **(0, 2, 2, 0, 7, 7, 0, 255)**. It made a source a source with thickness of 5 rows and a length of 128 pixels. We call this source as *standard source old screen*.
2. **Short Source**: This source, on the python script, is defined by **(0, 4, 4, 15, 8, 0, 0, 255)**. It made a source a source with thickness of 9 rows and a length of 72 pixels. We call this source as *short source old screen*.

Although the old screen was very useful for many tests on the bench, it was not ideal for setting up contrast. Changing the contrast affected the entire screen equally, either brightening or dimming all active pixels together. As a result, it could not accurately represent the sodium atom density profiles on the screen, which needs different brightness levels for different pixels.

So a new OLED screen was looked for and placed on the stage along with the old screen, as shown in fig.5.11

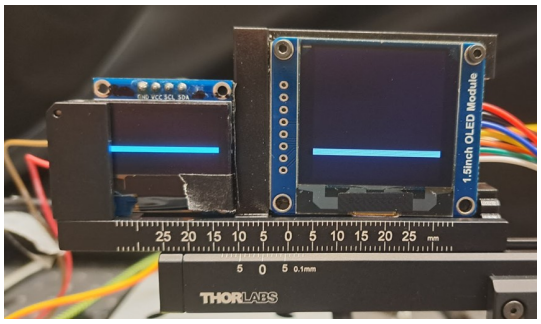

((a)) Standard source on old and new screen

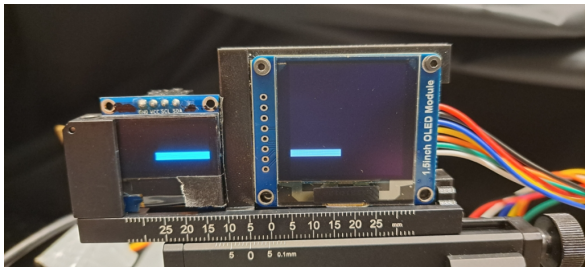

((b)) Short sources on old and new screen.

Figure 5.11: The images shows both the screens placed on the linear stage on ingot bench.

5.3.2 New Screen: SSD 1327

LGS is not a uniform source because the sodium density in the atmosphere keeps on varying and also varies with the altitude. Keeping this requirement in mind to test the Ingot, a new OLED screen, which we call New Screen was chosen with 128x128 pixels in dimensions with each pixel measuring 0.19x0.19 mm^2 and pixel pitch of 0.21x0.21 mm^2. This screen has a 16-level gray scale, which means that each pixel on the screen can be assigned with a different brightness from 0 to 15 using the python script. For this we use a bitmap written in C# to produce the LGS on the new screen. The bitmap is made up of a 128x128 matrix with each entry represented in hexadecimal format. The 128 entries are one for each pixel in a row on the screen.

Controlling the LGS on the New screen with C# code takes up a lot of space available as screen memory because every time we make change in the code it is required to upload it to the Arduino which also takes some extra time of around 40 seconds every time we use it. In order to make it efficient, the length of the source in this screen is kept fixed and the variable intensity of the pixels is used to turn some pixels off in case a shorter source is required . Rest of the features of the screen like the vertical position on the screen, thickness of the source and the uniform brightness of the source is defined by the string **(RD, TU, TD, C)**. The characters in the string are defined as:

1. **Row Decenter (RD)**: This represents the displacement of the source's center in rows, where negative values move down and positive values move up.
2. **Thickness Upwards (TU)**: It is the number of extra rows above the source's center row.
3. **Thickness Downwards (TD)**: It is the number of extra rows below the source's center row.
4. **Contrast (C)**: This parameter changes the entire intensity of the screen with values ranging from 0 to 255. The screen also has capability to lighten up each pixel with a different contrast, it is explained in sec.

With this function we have used two different uniform sources on the new screen. They are as follows:

1. **Standard Source**: We call this source *standard source new screen.*
    - The length of this source which is set from C# is 116 pixels. The length is kept 116 pixels so that the length of standard source old source is equal to standard source new screen. The 116 pixels are the first 116 starting from the right end of the screen, as shown in fig.5.11(a)
    - Other parameters of the source, on the python script, are defined by **(-37, 2, 2, 255)**. It made a source a source 37 pixels below the zero on the screen with thickness of 5 rows with brightness of 255. From now on we call this -37 pixel position as the zero position on the new screen
2. **Short Source**: We call this source *short source new screen.*
    - The length of this source which is set from C# is 58 pixels. This length of 58 pixels is equal to the length of short source old source. The 58 pixels that made this source were the first 58 pixels starting from left, as shown in fig.5.11(b) It was made so to accommodate this source at the same position as short source old screen by moving the linear stage.
    - Other parameters of the source, on the python script, are defined by **(-37,3,3,255)**. It made a source a source 37 pixels below the zero on the screen with thickness of 7 rows with brightness of 255.

For now, we have decided to keep the length fixed on the new screen. We simulate a shorter source by turning off the pixels at the ends which effectively adjusts the length without changing the code.

The above explained uniform sources were used in the initial tests to verify if the screen was good enough to be used on the bench. Once we were sure of its capabilities, we also used the sodium profiles on the screen.

5.3.3 Na Profiles on New Screen

The data that is used to replicate the sodium profiles on the new screen is the actual data of sodium density variation at different altitude in the atmosphere. The LIDAR (Laser Imaging Detection and Ranging) on the 6 meter Large Zenith Telescope in Canada was used to collect the sodium density at different altitudes[109].

The complete dataset consists of 16 datasets collected throughout July of 2010. Each of the dataset consist of 30 profiles obtained with an integration time of 10 seconds. It offers a vertical resolution of 126.5 meters. Also each dataset comprises of 198 height levels with lowest level in atmosphere corresponds to 80 km of altitude. The counts per height level varies to a maximum value that varies depending on the profile, and these counts are binned into 16 levels to ensure compatibility with the new screen gray scale settings.

In order to replicate the sodium profiles on the new screen we binned the 198 height

levels to 116 levels and maximum counts to 16 level gray scale, to accommodate the whole profile on the screen without loosing the data points. This is done by a python script that reads the dataset and then bins it for the profile. This is followed by communicating this command with the Arduino and thus replicating the profile on the screen[110]. Example of this Na profiles are shown in Fig.5.26.

5.3.4 Old Screen vs New Screen

As we have already discussed , the old screen posed the limitation with setting different contrast to different pixels simultaneously, the new screen was brought and placed on the adjustable stage to resolve this issue. We could not directly replace the old screen with the new screen so we did some tests and calculated the flux and SNR (Signal to Noise Ratio) at the aligned position for a detailed comparison.

5.3.4.1 Alignment with Old and New Screen

If both the screens are to be compared, the first step would be to see if we are able to align the source on both the screens. But before alignment of the source, when we first kept the new screen on the setup, we observed some patterns on the transmitted pupil. While looking for the problem we found that there was some angular emission from the side of the new screen that was facing the ingot. To resolve this we placed a tape on that side which stopped the angular emission which can be seen in the fig.5.12

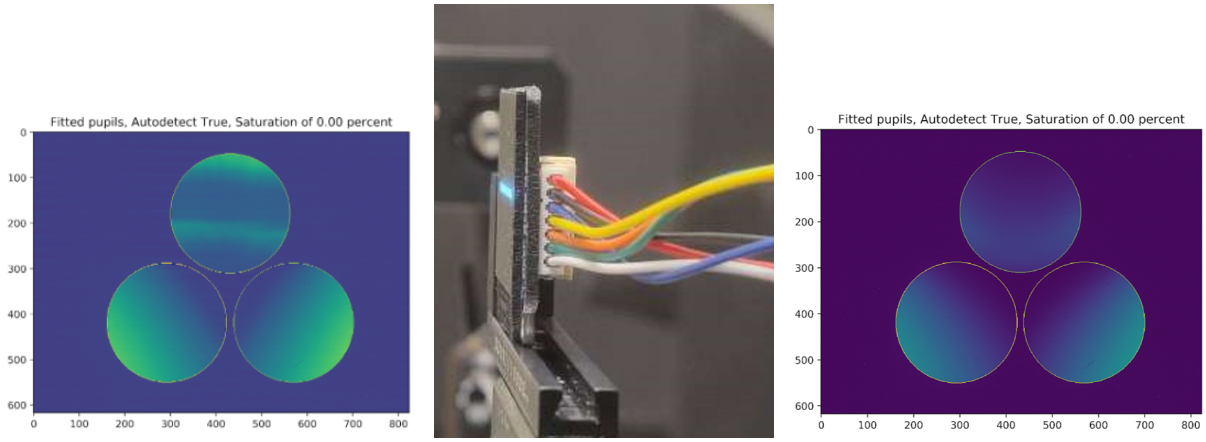

((a)) Three pupils before the tape was placed on the screen.

((b)) Tape placed on the side of the screen

((c)) Three pupils after the tape was placed.

Figure 5.12: These images show how the angular emission from the side of the New Screen is altered by the presence of tape.

To compare the alignment of sources on both screens, short sources with same characteristics were replicated on both screens. These uniform sources were made so that we could just move the linear stage and place both the sources at almost the same position on the bench, as shown in fig.5.11. Both the sources were made with similar dimensions Comparison can be seen on the Table 5.3.

Table 5.3: Comparison of Source Sizes and Illuminated Areas

	Short Source Old Screen	**Short Source New Screen**
Length (pixels)	72	58
Width (pixels)	9	7
Total Area of Source (mm^2)	14.58	14.66

This gave us proof that the sources on both the screens were similar in area. Now for the alignments, we calibrated and aligned the old screen using the short source. Then, we repeated the process with the short source new screen. For all the calibration and alignment during this test we used an exposure time of 500 ms.

The final alignment frames and final alignment position are shown in 5.13 and 5.4 respectively.

Table 5.4: Final Alignment Positions of Short Source on Old Screen and New Screen

Alignment Axis	**OLD Screen**	**New Screen**
X	0.016	0.779
Y	9.213	5.811
Z	0.087	0.863
U	0.240	0.236
V	-0.034	0.019
W	0.030	0.039

5.3.4.2 Background Emission

As a further test, it was crucial to determine if there was any emission from the other screen (if it was left switched on) and the unused pixels from the screen which was used to create the source, as this could interfere with the calculations. Such emissions are generally very low, but if they are high, they could interfere with the experiment by affecting pupil measurements and intensities. It could potentially introduce some errors in the data.

To conduct the background emission test, we completely disconnected the old screen from power supply and turned on the new screen without creating any kind of source on it. A total of 5 frames were taken with an exposure time of 2 seconds. The same test was conducted when the new screen was disconnected from power supply and old screen was connected but no source was replicated i.e. all the pixels were turned off. Also in this case, 5 frames with an exposure time of 2 seconds were taken. The test was repeated when none of the screens was given the power supply, again 5 frames were taken at an exposure time of 2 seconds.
To make the calculations, the 5 frames were averaged to create a master frame for all the three tests. Then on the master frame total counts in the frame were calculated, the

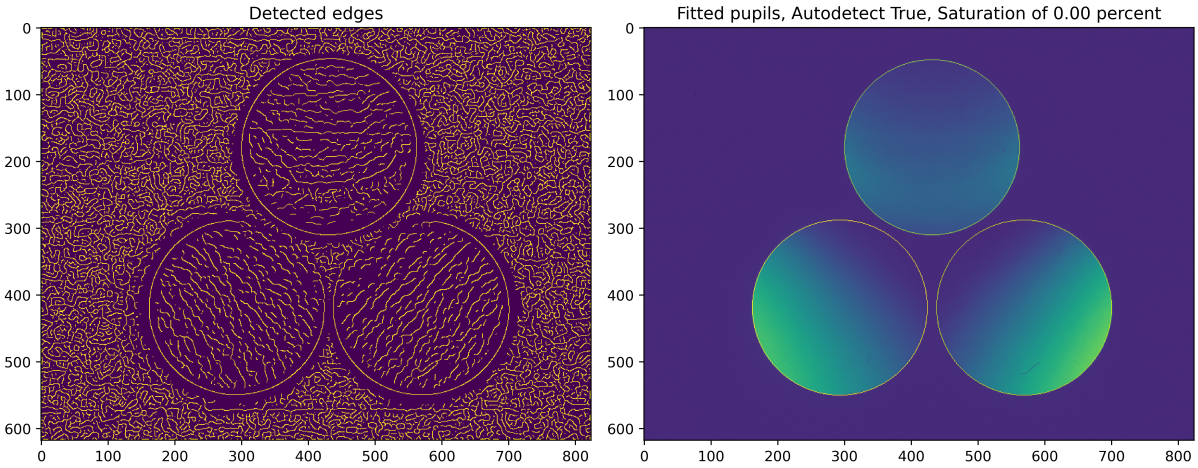

((a)) Detected pupils at the alignment position for old screen

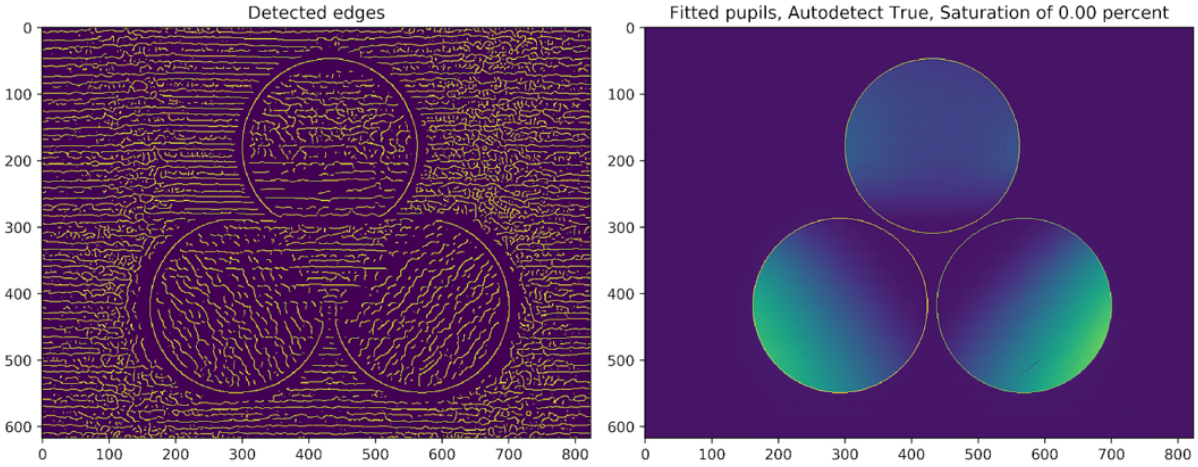

((b)) Detected pupils at the alignment position for old screen

Figure 5.13: Final Alignment frame for short source on both the screens

results were:

$$\text{Emission with no source on new screen and old screen not connected} = 9.39 \times 10^7$$
$$\text{Emission with no source on old screen and new screen not connected} = 9.37 \times 10^7$$
$$\text{Emission with no screen connected} = 9.32 \times 10^7$$

The results of emission when one of the screens was turned off was found to be similar and it was just 1.07% higher than emission calculated when none of the screen was connected. This gives us results that there is no significant background emission from any of the screens or the pixels that were not being used. So it can be said that there is very minimal emission from the OLED screen when it is turned on with no source on it.

5.3.4.3 Flux and SNR

For a good comparison between the screens the flux and SNR was calculated. Though the data collection was similar for both the screens, there is not a lot of data available for old screen for the comparison because a part of the screen suffered a damage during its

removal from the stage. The data collection and computations for both the screens were done as follows:

Old Screen: For the calculation of flux and SNR of the old screen, two frames taken at an aligned position with the short source were used. These frames were already dark-subtracted and binned (2,2) relative to the original frames captured by the camera. Two frames were captured with an exposure time of 500 ms each, then averaged to produce a master signal frame. To calculate the noise, 100 dark frames were captured using the same exposure time of 500 ms, and these were also averaged to create a master dark frame. The noise for each pixel is then given as the standard deviation of each pixel values across the 100 dark frames. The error associated to the SNR is computed as the standard deviation of the SNR across each pupil and is reported on Table 5.5. The master dark frame was then binned (2,2) to match the dimensions of the master signal frame.

Using the master signal and noise values, the SNR map was calculated using the following formula:

$$\mathrm{SNR} = \frac{\mathrm{Signal}}{\sqrt{\mathrm{Signal} + \mathrm{Noise}^2}} \tag{5.5}$$

From the SNR map, shown in fig.5.14(a), we determined the minimum SNR, maximum SNR, mean SNR, and standard deviation of SNR for each pupil. The results of these calculations are shown in Table 5.5. Additionally, we calculated the flux in each pupil from the total number of counts on the master signal frame. These flux results are mentioned and compared with the flux values for the new screen in Table 5.6.

New Screen: For the calculation of flux and SNR of the new screen, 100 signal frames were taken at an aligned position. The master dark was obtained in a similar manner as for the old screen, by capturing and averaging 100 dark frames. However, for the new screen, we subtracted the master dark from each signal frame individually before averaging all 100 dark-subtracted signal frames to create the master signal frame. Both the master dark and master signal frames were then binned to (2,2) because that is the dimension that we always use for all kind of tests. Using this master signal and the master dark, the SNR map was calculated using the formula 5.5.

The SNR map for new screen is shown in fig.5.14(b), and the SNR comparison with old screen is shown in Table 5.5. Also the flux was calculated in all the pupils on the binned master signal by summing up the total counts in the pupils. The flux results are shown and compared in the table 5.6.

Table 5.5: Comparison of SNR values between Old Screen and New Screen. We report the minimum SNR, maximum SNR, mean SNR, and standard deviation of SNR for each pupil.

	Old Screen			New Screen		
Pupil	Min SNR	Max SNR	Mean SNR	Min SNR	Max SNR	Mean SNR
Pupil A	0.92	31.28	21.00	4.69	47.40	31.07
Pupil B	0.00	45.97	25.70	3.25	49.64	31.82
Pupil C	0.00	47.47	25.72	1.69	53.81	32.52
Pupil	Old Screen Std SNR			New Screen Std SNR		
Pupil A	5.01			9.38		
Pupil B	12.28			11.43		
Pupil C	11.16			13.84		

Table 5.6: Comparison of Flux values between Old Screen and New Screen

	Old Screen	**New Screen**
Pupil A Flux	2.7×10^7	5.9×10^7
Pupil B Flux	4.4×10^7	6.4×10^7
Pupil C Flux	4.5×10^7	7.0×10^7
Total Flux in All Pupils	1.2×10^8	2.0×10^8

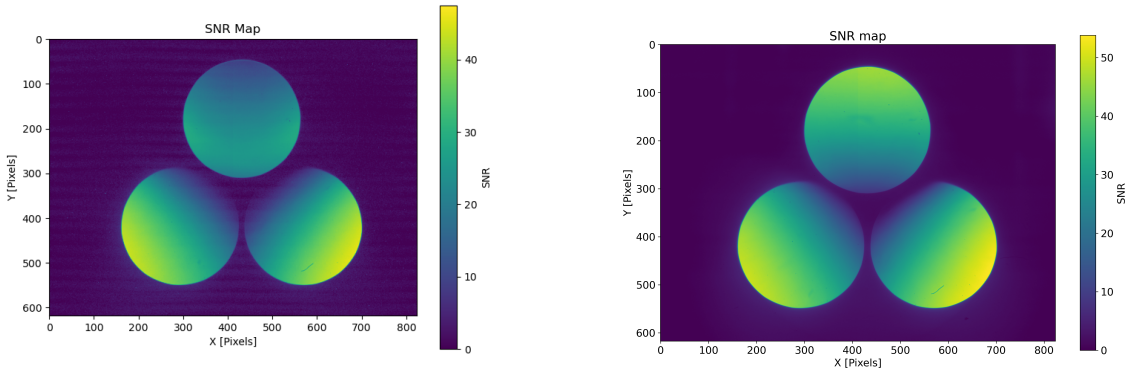

((a)) SNR map of Old Screen

((b)) SNR map of New Screen

Figure 5.14: Comparison of SNR maps between Old Screen and New Screen

5.3.4.4 Effective Brightness

Now we know that the new screen produces higher flux on the camera detector and gives higher SNR than old screen in our setup, but it does not give us the idea of how bright is the new screen compared to the old screen.

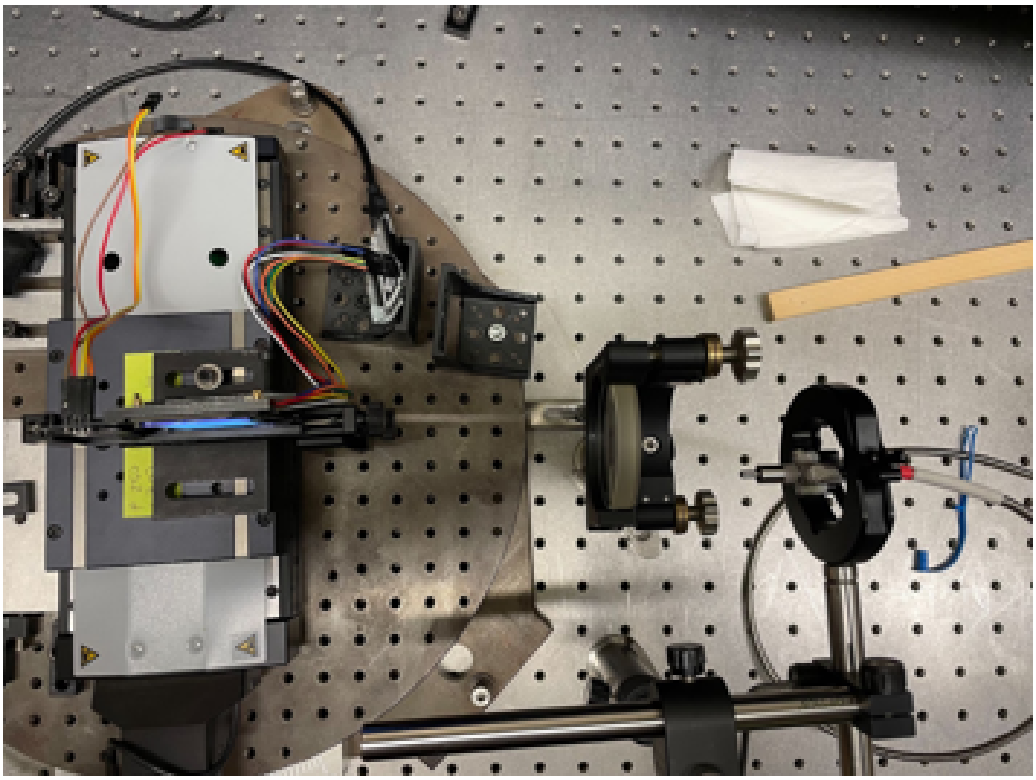

Figure 5.15: In this image, the OceanView Spectrometer can be seen in the optical path of the bench. It was used to collect the spectra of the screens.

To assess the brightness of the screens, we used the Oceanview HDX spectrometer, as shown in Fig.5.15 , which operates over a wavelength range of 200-1100 nm with an optical resolution of 1.1 nm. The spectrometer was placed in the optical path immediately after the collimating achromatic doublet lens. First, we captured dark frames for each screen by turning off all the pixels on the screen being measured, while the other screen was disconnected from the power supply. The same procedure was repeated for both screens. This was followed by capturing the spectra of the screens. During the whole process we ensured that each screen was placed at same position on the bench. During the measurement of one screen's spectrum, the other screen was turned off, and all pixels on the screens were illuminated.

For screen spectra data and dark spectrum, we set the integration times to 8 seconds for the new screen and 14 seconds for the old screen. Afterwards, the dark and spectra of new screen were re-scaled to an integration time of 14 seconds. Figures X and Y show both the raw spectra and the dark-subtracted spectra for each screen. To determine which screen is brighter, we utilized the quantum efficiency plot of the Prosilica GT3300[2] camera, shown in fig.5.15, which covers a range from 350 nm to 1050 nm. Since the tabular quantum efficiency data was not available, we employed WebPlotDigitizer[111] to trace the curve and extract the quantum efficiency values in tabular form. This process was repeated three times, and the average values were used as the quantum efficiency for

[2]The values have been taken from the Instrument Datasheet.

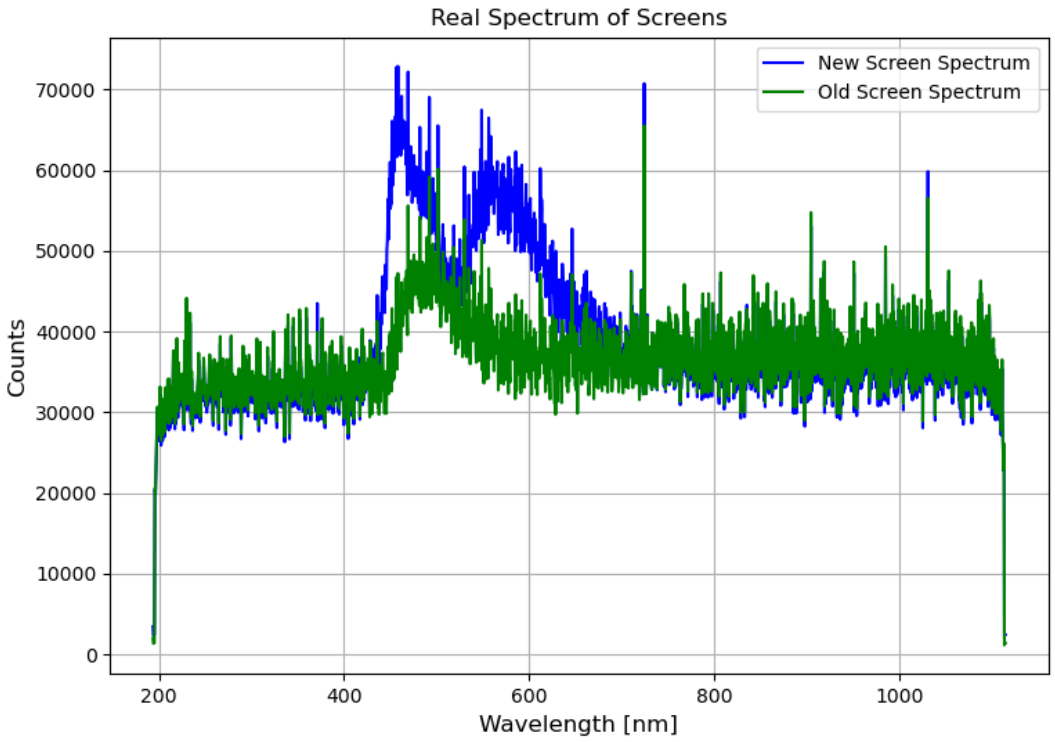

Figure 5.16: Raw Spectra of both old and new screen with all the pixels lighten-up.

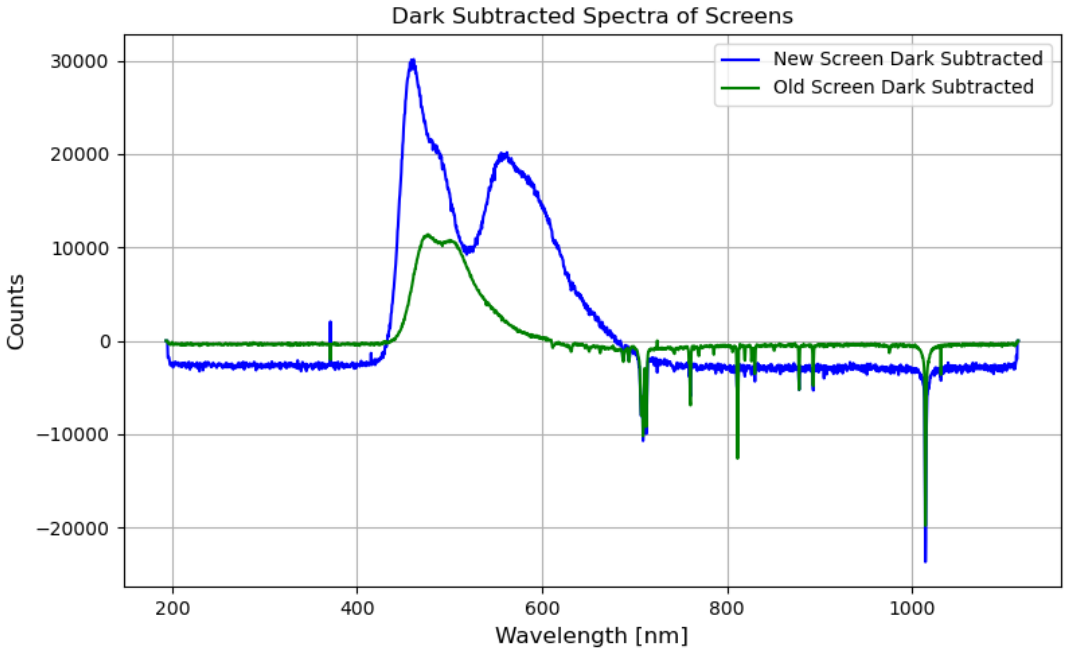

Figure 5.17: Dark Subtracted Spectra of both old and new screen.

each wavelength.

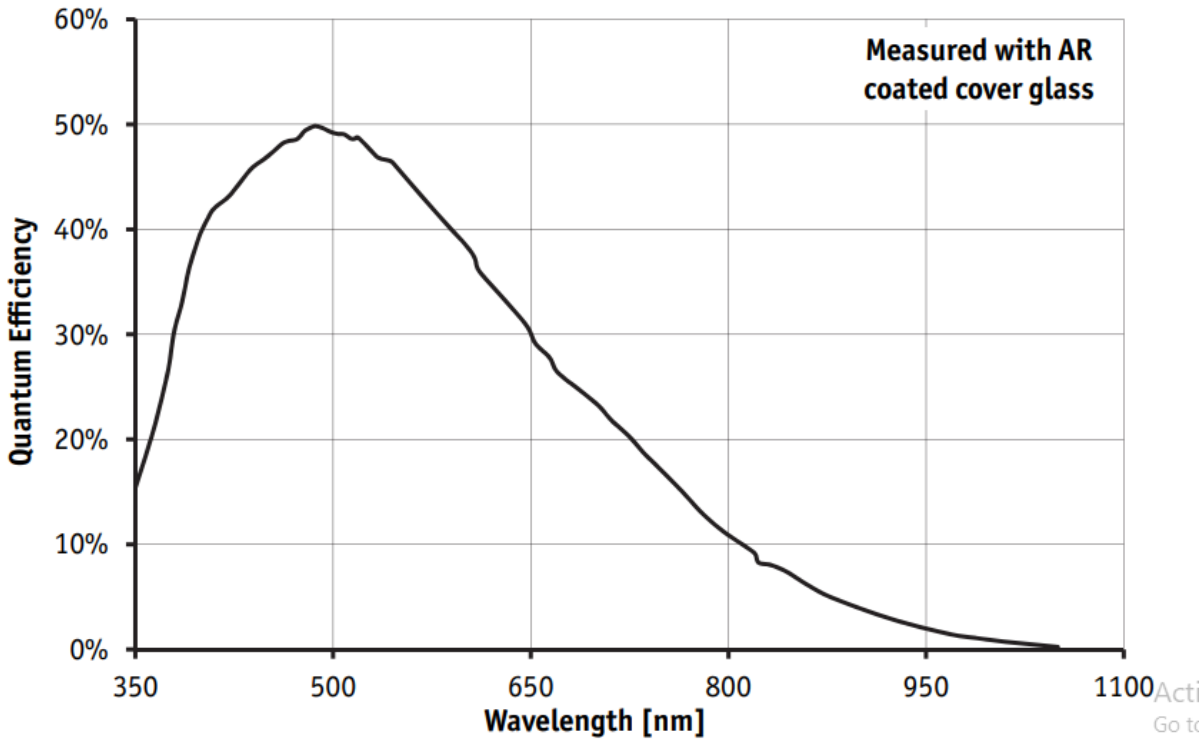

Figure 5.18: Quantum Efficiency Plot of Prosilica GT3300 from the

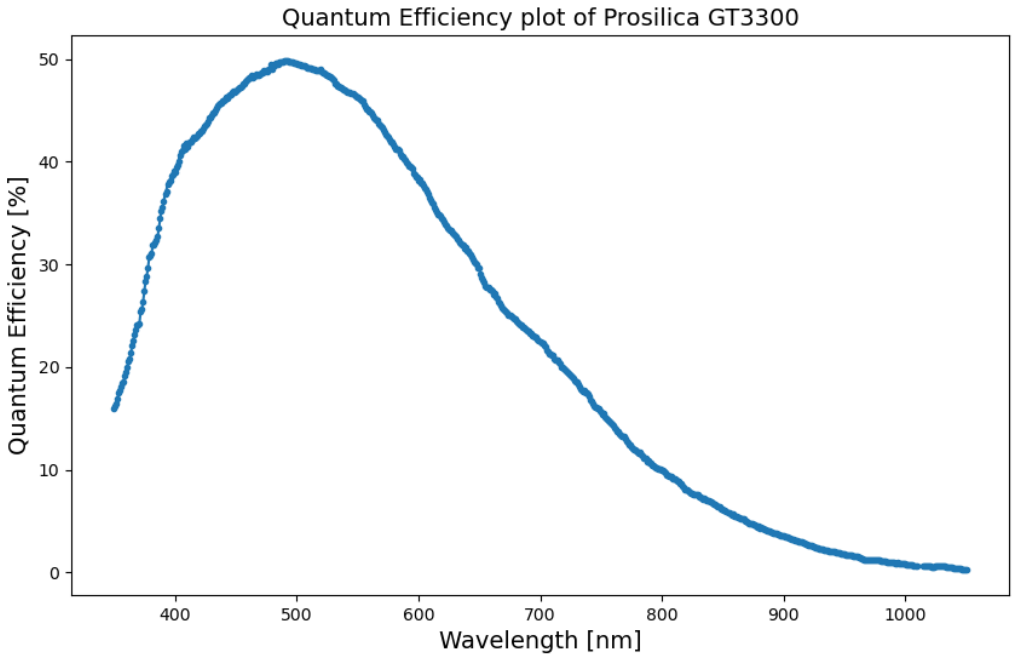

Figure 5.19: Quantum Efficiency Plot of Prosilica GT3300 retrieved using Webplotdigitizer.

During the spectral analysis of the screens, some intensity values turned negative after dark subtraction. For the calculation of effective counts, these negative values were set to zero. To find the effective flux recorded by the camera for each screen, we used the equation 5.6:

$$\text{Effective Flux} = \sum_i \left(I(\lambda_i) \times \frac{\text{QE}(\lambda_i)}{100} \right) \tag{5.6}$$

where:

- $I(\lambda_i)$ represents the intensity counts at wavelength λ_i,
- $\text{QE}(\lambda_i)$ represents the quantum efficiency of the camera at wavelength λ_i (given as a percentage).

The plots and the results for the computation of effective flux of both the screens:

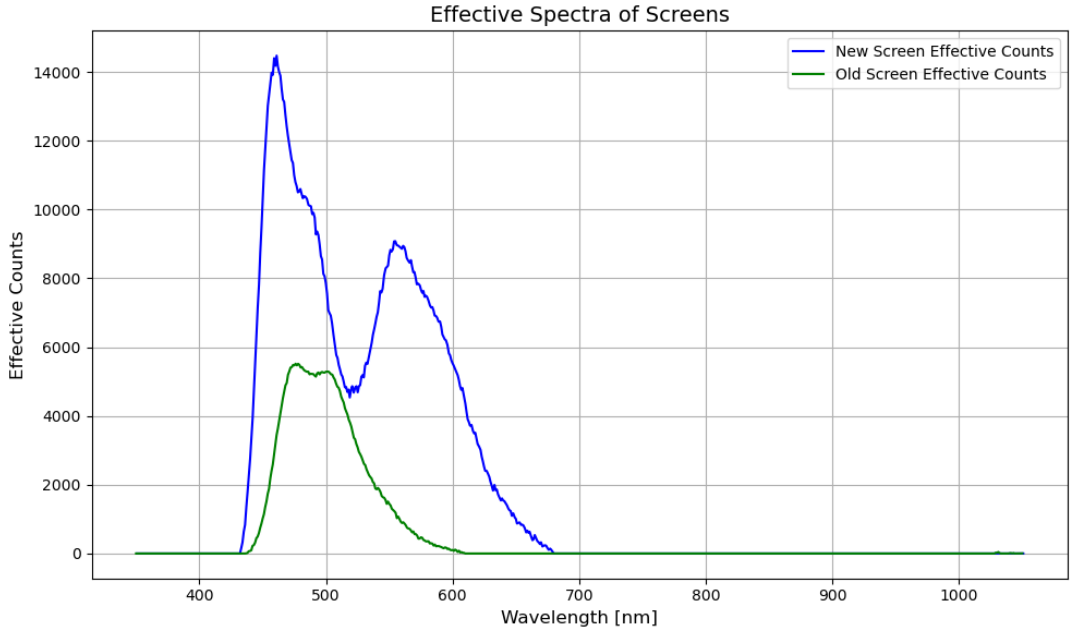

Figure 5.20: Effective spectra of screens as detected by the camera Prosilica GT3300.

$$\text{Effective Flux for New Screen: } = 1.5 \times 10^6 \text{counts*nm}$$
$$\text{Effective Flux for Old Screen: } = 4.1 \times 10^5 \text{counts*nm}$$

Brightness Ratio (New Screen / Old Screen): $= 3.54$

So it is evident from the results that the new screen is brighter than the old screen.

From all the results it was concluded that new screen, when compared to the old screen, has a higher effective flux and ability of replicating variation in source intensity, which enables better replication of the Na-LGS. So the old screen was completely removed from the stage and now only new screen is on the stage, as displayed in the figures below.

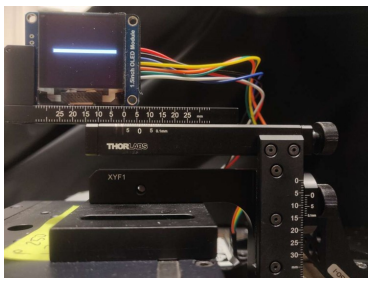

((a)) New Screen placed on the linear stage

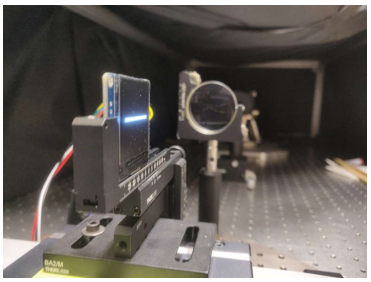

((b)) Ingot bench from the New Screen

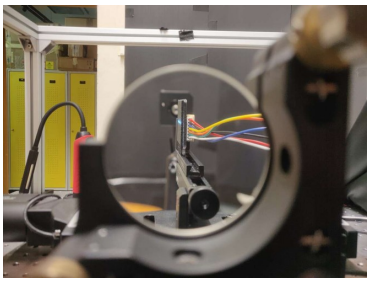

((c)) New Screen as seen from the pupil

Figure 5.21: The pictures after the old screen was removed from the bench and only new screen remains on the bench.

5.4 Vertical Shifts of LGS Source

On the Ingot bench, as discussed earlier, we follow specific defined alignment procedure. The alignment procedure starts with obtaining a calibration with the source when I-WFS is placed at a position close to the alignment position. This is followed by starting of the alignment process as explained in section 5.2.2. Following the same alignment procedure, we performed numerous tests with the standard source new screen and the ingot aligned successfully in different conditions. However, we also aimed to evaluate the accuracy of the I-WFS in detecting vertical movements of the source on the screen and to determine the maximum distance from the starting point at which it could effectively detect and properly align.

To perform this test, we first obtained a calibration using the standard source at an exposure time of 500 ms. Next, the source was aligned at various vertical positions based on the calibration data from the new screen of the standard source. The vertical displacements were measured in pixels relative to the initial position of the standard source. This approach allowed us to quantify the positional changes accurately and ensure consistent alignment across different vertical positions.

We chose a random sequence for the initial movements and then repeated the sequence three times. The series followed was as follows:

0 → +3 → +6 → +9 → +11 →+13→+12 →+10→+7→+5→+8→+4→+1→+2→ -1→ -4→ -6→ -7→ -5→ -2→ -3

For example, the initial alignment was performed at position 0. After this, the source was shifted upward by 3 pixels, and realignment was conducted at this new position. Subsequently, the source was moved up by another 3 pixels, reaching a position that was +6 pixels above the initial standard source position. This pattern of incremental shifts continued as outlined in the series, allowing for systematic alignment across varying vertical displacements.

We repeated the series three times and then plotted the movement in pixels on the screen against the alignment position of hexapod. We plotted the mean of three aligned position and for error also calculated the standard deviation at each position. The plots, as shown

in fig.5.22, 5.23 and 5.24, were only made for X, Y and Z alignment positions of the hexapod because there was almost no movement seen on the U, V and W axis. It is to be noted that due to an error in acquiring the data at +5 vertical position, only two aligned images are considered for plotting the data.

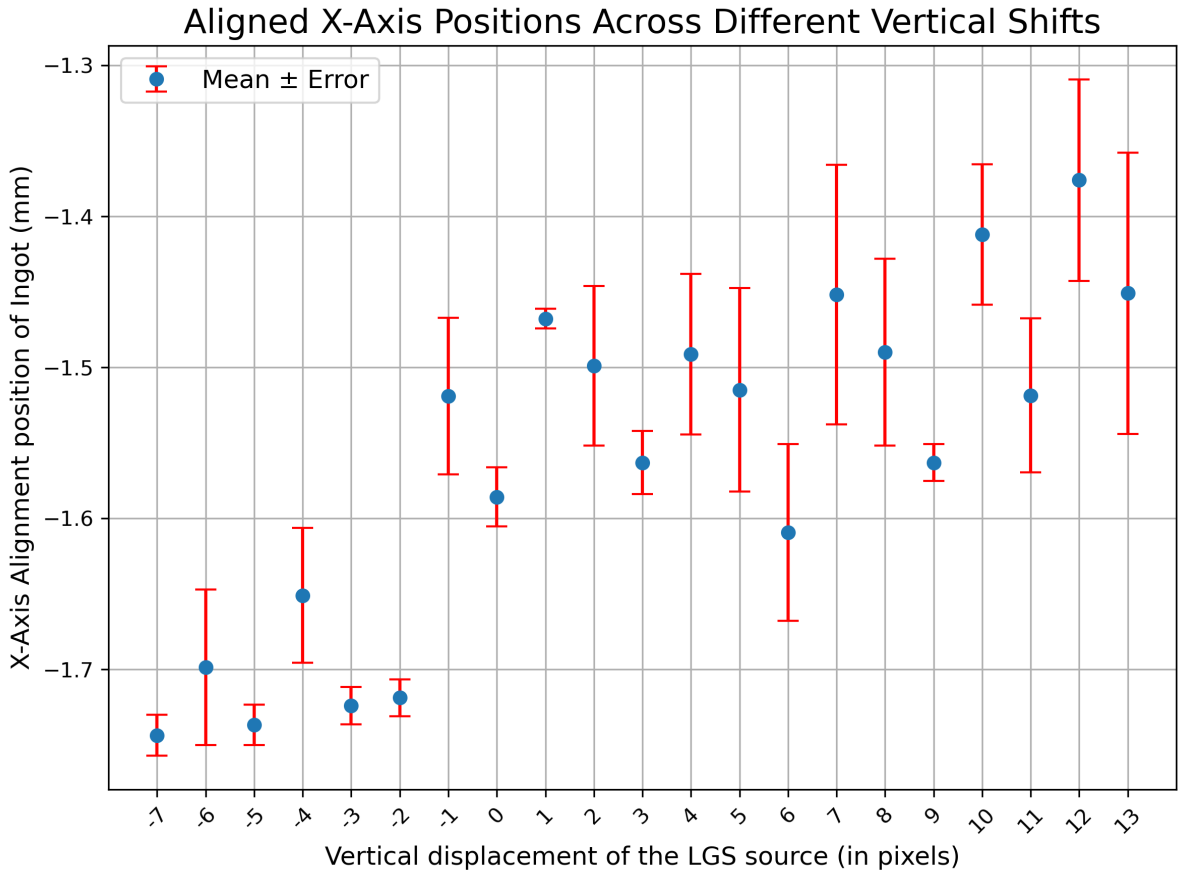

Figure 5.22: The x-axis shows the Vertical Position of the LGS source [in pixels = 0.21 mm], while the y-axis represents the mean X-axis position of the hexapod in millimeters after alignment, illustrating how the LGS source's vertical displacement affects the hexapod's final position.

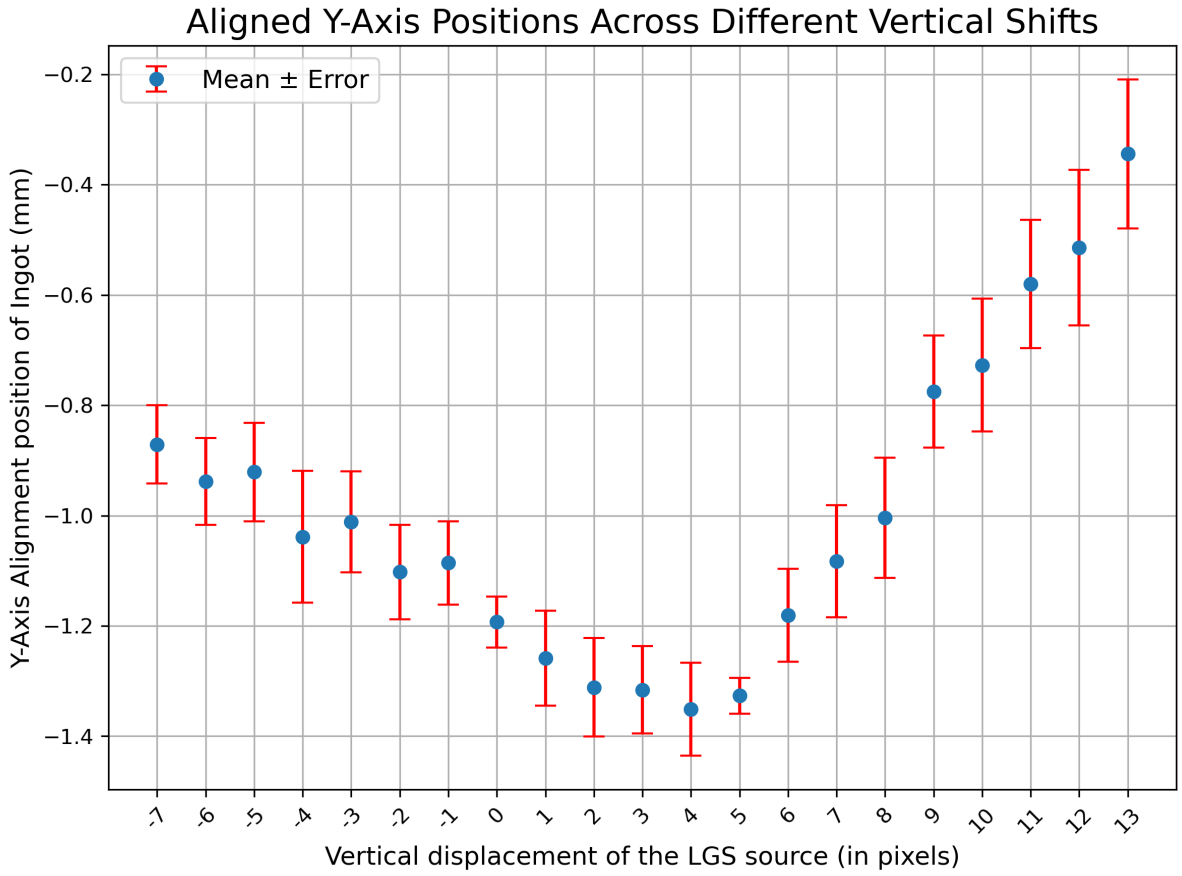

Figure 5.23: The x-axis shows the Vertical Position of the Laser Guide Star (LGS) source [in pixels = 0.21 mm], while the y-axis represents the mean Y-axis position of the hexapod in millimeters after alignment, illustrating how the LGS source's vertical displacement affects the hexapod's final position.

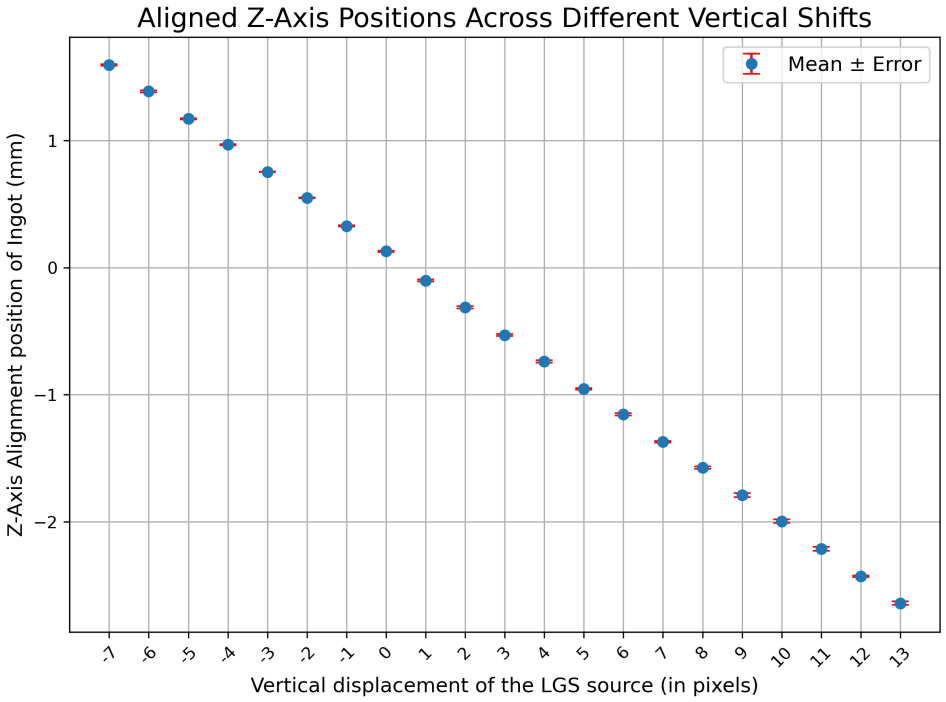

Figure 5.24: The x-axis shows the Vertical Position of the Laser Guide Star (LGS) source [in pixels = 0.21 mm], while the y-axis represents the mean Z-axis position of the hexapod in millimeters after alignment, illustrating how the LGS source's vertical displacement affects the hexapod's final position.

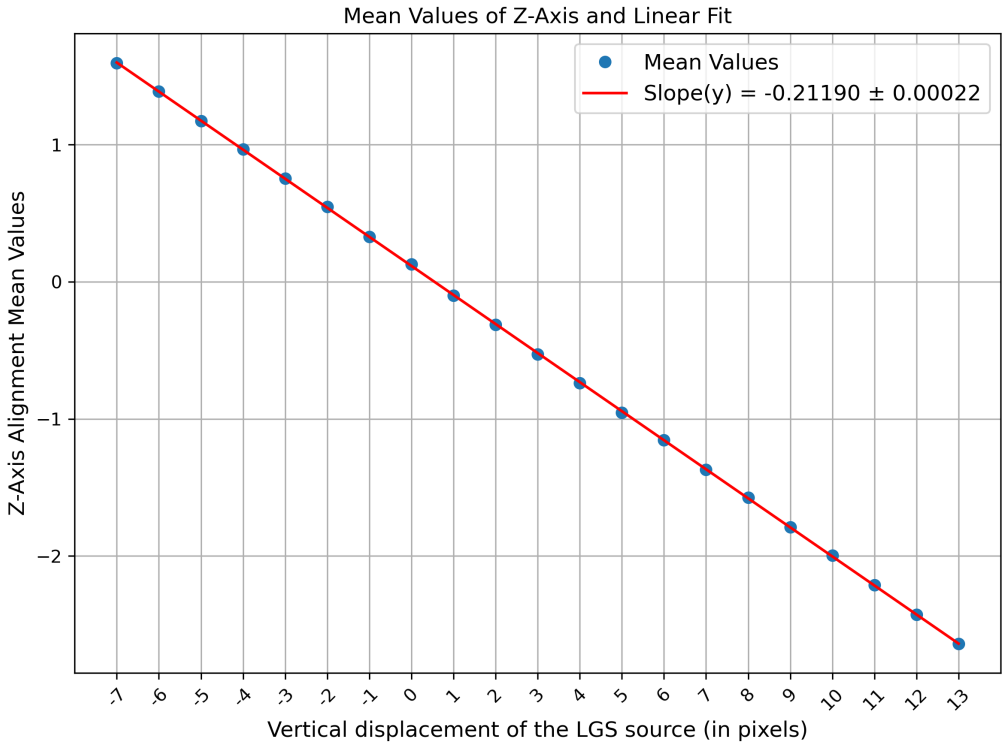

Figure 5.25: Linear fit performed on the Z-Axis Alignment Position

With this vertical movement, we were able to determine that using the same calibration we can align the source 13 pixels above and 7 pixels below the position where the calibration was taken.

When describing the ingot bench in section 5.1, it was noted that the optical bench features a 1:1 re-imaging relay.

When we conducted the tests of vertical movement of the source on the screen, the corresponding movement was observed on the Z-axis, this axis represents the vertical movement of the hexapod. We performed the linear fit on the mean values of Z-axis alignment position, visible in fig 5.25.

Slope of the Linear Fit: $= -0.21190\,\mathrm{mm/px}$

Error of Linear Fit: $\pm 0.00022\,\mathrm{mm/px}$

In section 5.3.2, we discussed that the pitch scale of New Screen is 0.21 mm. Therefore for this vertical position test, one position of the source and the following one is separated (vertical shift) by a distance of 0.21 mm. The results of linear fit also helped us determine if our test bench is 1:1 re-imaging relay as our designed one.
Since the slope of the linear fit and the pitch scale of the screen are equal, we can infer that a movement of 1 pixel will give us a similar movement of hexapod along z direction. This confirms that our optical bench has a value 1 magnification, as in its design. This information can be used in simulations of our test-bench.

5.5 Na Profiles

During the tests, we discovered that we could align the standard source on the new screen at any position under specific favorable conditions. Since the I-WFS is for Na-LGS, we needed to test if we could align I-WFS with a more realistic Na-LGS source on the screen, including profile variations.

To test this capability, we used the real sodium density profile data that was collected using the LIDAR (Laser Imaging Detection and Ranging) on the 6 meter Large Zenith Telescope in Canada. The specifications are more clearly discussed in the sec 5.3.3

Testing all the profiles in a loop would be a little complicated as the first test so we opted for 3 random profiles from the data that was collected on the night of 10^{th} July, 2010. We call the 3 Na-Profiles as Case1, Case2 and Case3, as shown in Fig.5.26.

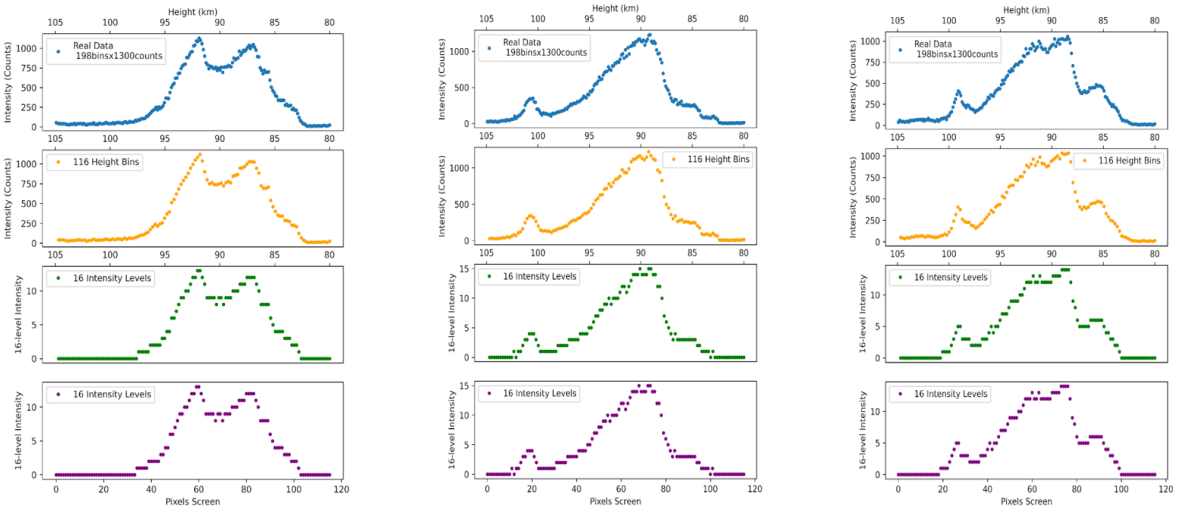

((a)) Na Profile Case 1 ((b)) Na Profile Case 2 ((c)) Na Profile Case 3

Figure 5.26: Different Na-Profiles from the data collected using the LIDAR (Laser Imaging Detection and Ranging) on the 6 meter Large Zenith Telescope in Canada. Also it can be seen here how the altitude and density of real profile is binned and accommodated to the standards of sources on the screen.

Once the Na profiles were binned, it was time to replicate them on the new screen. To perform this we used a python script that would read the profile from the files, bin it and then communicate it with Arduino. Using the python script we could control the brightness of all the pixels on the screen separately. The images of Na profiles when replicated on the screen are shown in fig.5.27.

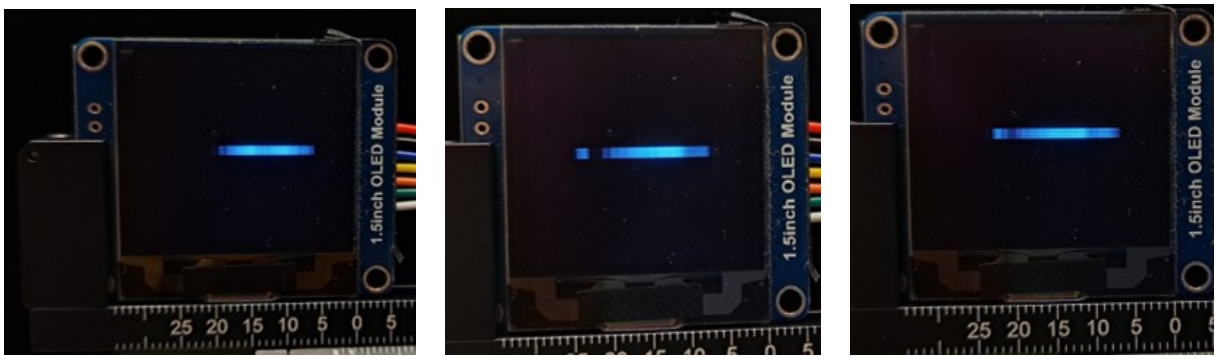

((a)) Na Profile Case 1 ((b)) Na Profile Case 2 ((c)) Na Profile Case 3

Figure 5.27: The 3 cases of the Na Profiles on the Screen

To align the Ingot-WFS with the Na-profiles we took a calibration with the standard source at an exposure time of 1250 ms. Then the standard source new screen, Case 1, Case 2 and Case 3 were put on the screen and aligned in a random order, keeping in mind not to run the alignment test for the same source simultaneously. The alignment data was collected three times for all the four sources. The mean and standard deviation was

then plotted for X, Y and Z axis alignment position of hexapod. The plots that we got are:

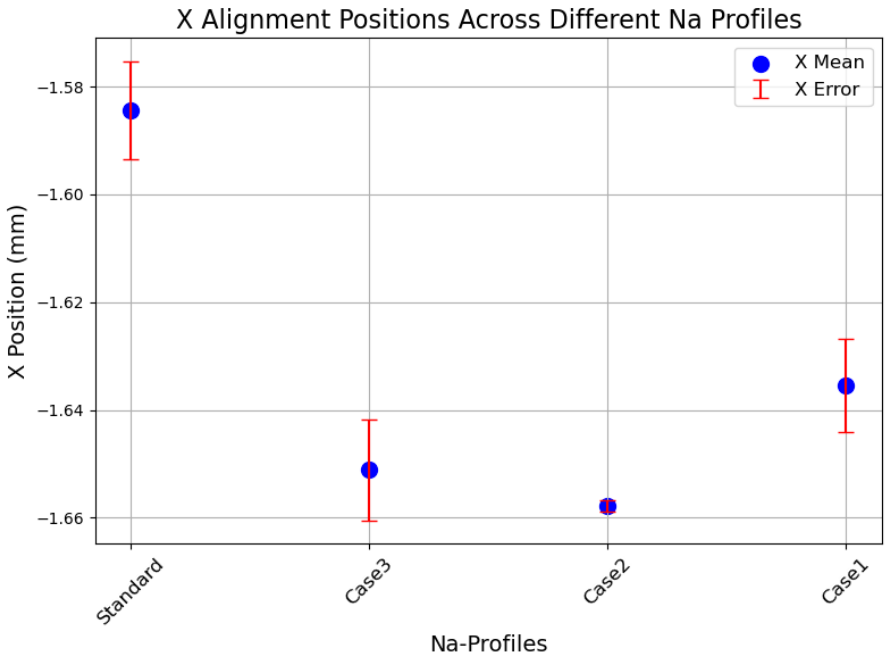

Figure 5.28: Mean and Standard Deviation on X-Axis Aligned Position for the Standard Source and the three Na-Profiles.

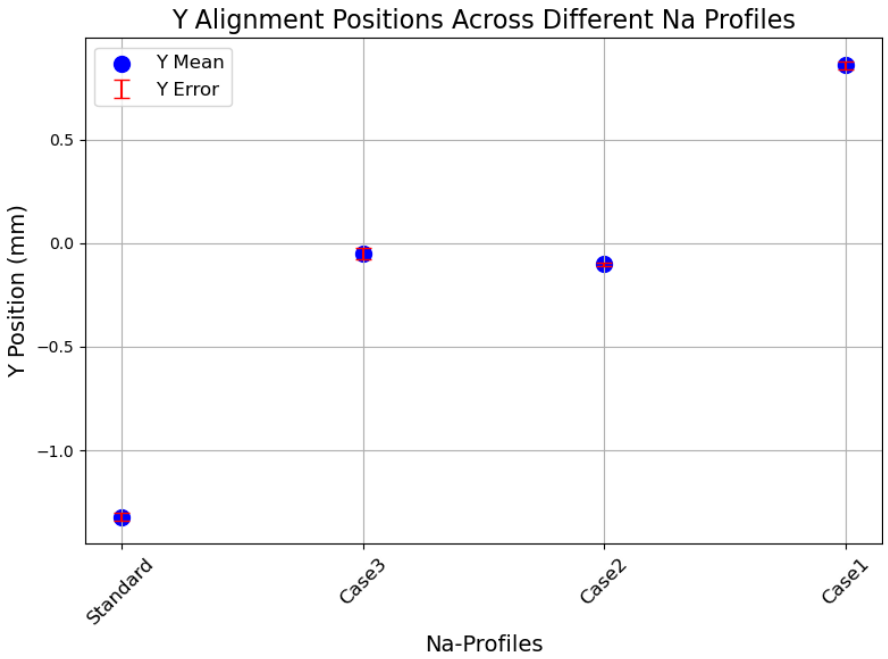

Figure 5.29: Mean and Standard Deviation on Y-Axis Aligned Position for the Standard Source and the three Na-Profiles.

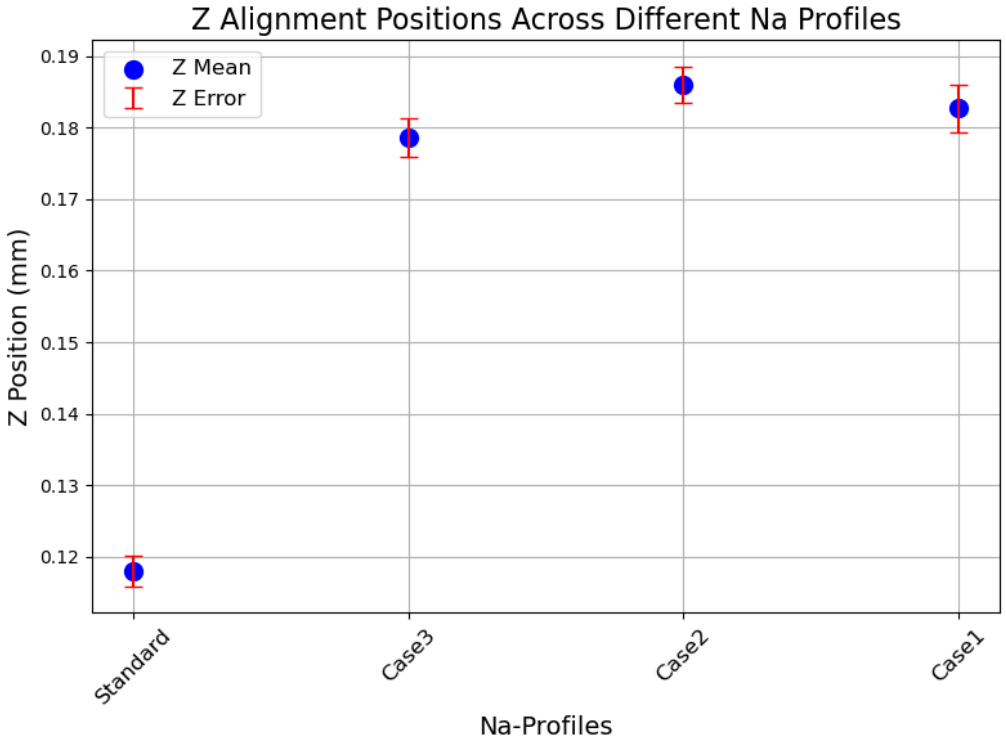

Figure 5.30: Mean and Standard Deviation on Z-Axis Aligned Position for the Standard Source and the three Na-Profiles.

Based on the results, it can be concluded that the I-WFS is able to align with various Na-profiles and detects the expected variations among them. The plots clearly show that changes in intensity at specific points in the source can influence the alignment position. The change in movement that we expect from the I-WFS is along the Y-axis, a clear movement can be noticed in the alignment position of Y-axis showing us a focus adjustment of the order of 1.8 mm from standard source to case 1. This shows that variations in intensity impact the Y-axis alignment, while having much smaller effect on the other axes (0.06 mm shift on Z-axis and 0.08 in X-axis).

Although the results show that the Ingot can detect small increases in intensity in all tested sources, the exact sensitivity to these changes are uncertain. To address this uncertainty and quantify the sensitivity more precisely, we conducted some sensitivity tests on the I-WFS. In these tests we focused on measuring the alignment position shifts as a response to varying intensity at one position on uniform profiles to establish a clearer understanding of how each axis responds to changes as the source changes. The results and analysis of these sensitivity tests are discussed in detail in the next section.

5.6 Sensitivity to LGS Profile Variation

Characterizing the sensitivity of the Ingot is very important information as it will help us say how small of a intensity variation along the LGS profile can be detected by it. To perform this test, we made user given profiles using a python code. There we by hand gave the input intensity for each pixel. This gave us a free hand to make simple profiles

and test them.

Using this python script, we created a total of 16 profiles based on four different uniform profiles. In our case, we took four uniform profiles with intensities of 8, 12, 13, and 14. For each of these uniform profiles, we introduced peaks rising from the uniform intensity to the highest intensity of 15 and then back to the uniform intensity, forming a gaussian of intensity rise. On each uniform profile, we created a peak on the right end (right peak), a peak in the center (central peak), and a peak on the left end (left peak). So for each intensity that we chose, we had a total of four profiles, which are as follows:

1. Uniform profile at that intensity

2. A right peak on the uniform profile.

3. A central peak on the uniform profile.

4. A left peak on the uniform profile.

The profiles have been named 6.03%, 1.50%, 0.66% and 0.18% based on the relative increase in intensity compared to uniform source of intensity 8, 12, 13 and 14. All the profiles that we created for the each uniform intensity level can be seen in the Fig.5.31. While making these profiles we kept in mind to keep the peaks centered on the same pixels. For example, the center on the right peak at intensity 8 and the center on the right peak at intensity 13, are at the same position. The same applies to all the other peaks and profiles. To test these profiles, we first obtained the calibration using all the uniform profiles. These calibrations was then used for the alignment procedure of the uniform source along with the three intensity peaks based on that uniform source. To ensure the reliability and consistency of our results, all the tests were repeated three times, each with an exposure time of 1250 ms.

The plots we made illustrate the left, central and right peaks on the x-axis and the alignment position relative to the alignment position of the uniform source of that intensity on the y-axis. For instance, the relative alignment position of right peak with intensity 6.03% was taken based on the uniform source with intensity 8. In the same way, the relative alignment position of right peak with intensity 0.18% was taken based on the uniform source with intensity 14.

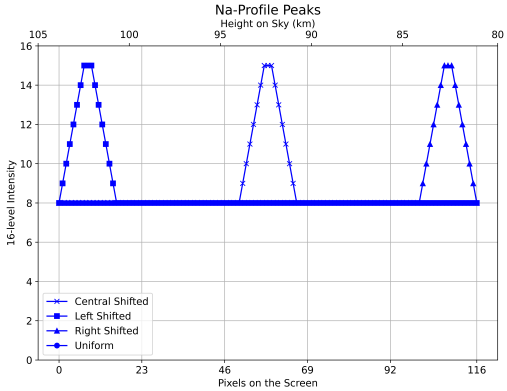

((a)) Uniform Source of intensity 8 with three 6.03% intensity peaks.

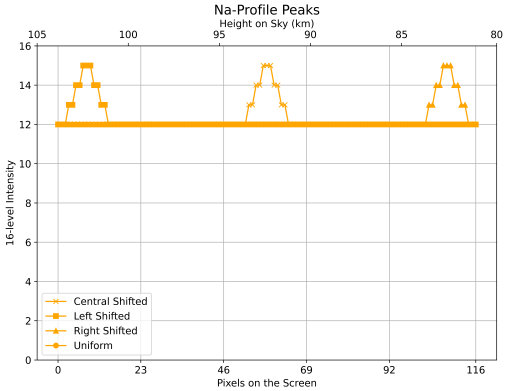

((b)) Uniform Source of intensity 12 with 3 1.50% intensity peaks.

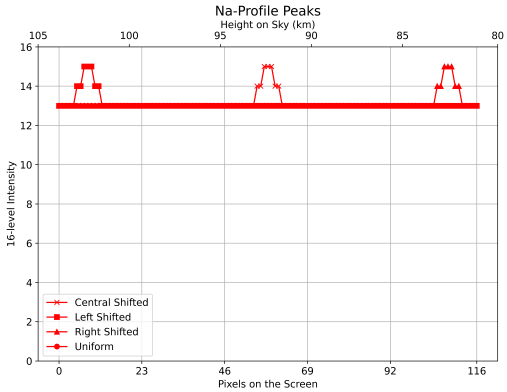

((c)) Uniform Source of intensity 13 with 3 0.66% intensity peaks.

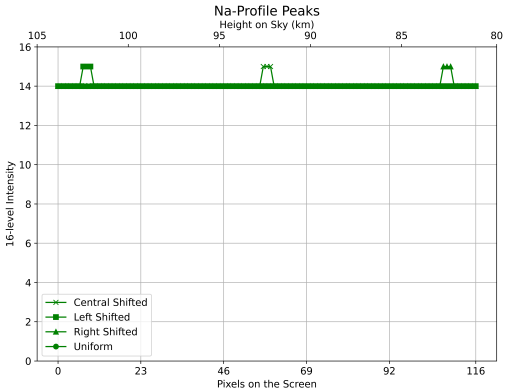

((d)) Uniform Source of intensity 14 with 3 0.18% intensity peaks.

Figure 5.31: In the plots above, the uniform sources and the intensity peaks on the uniform sources are shown. The bottom x-axis of all the plots shows the pixels on the screen, the x-axis on the top shows the height where this profile is expected on the sky, and on the y-axis we have the 16-level gray scale of the new screen. The gray scale goes from 0 to 15, thus giving 16 levels.

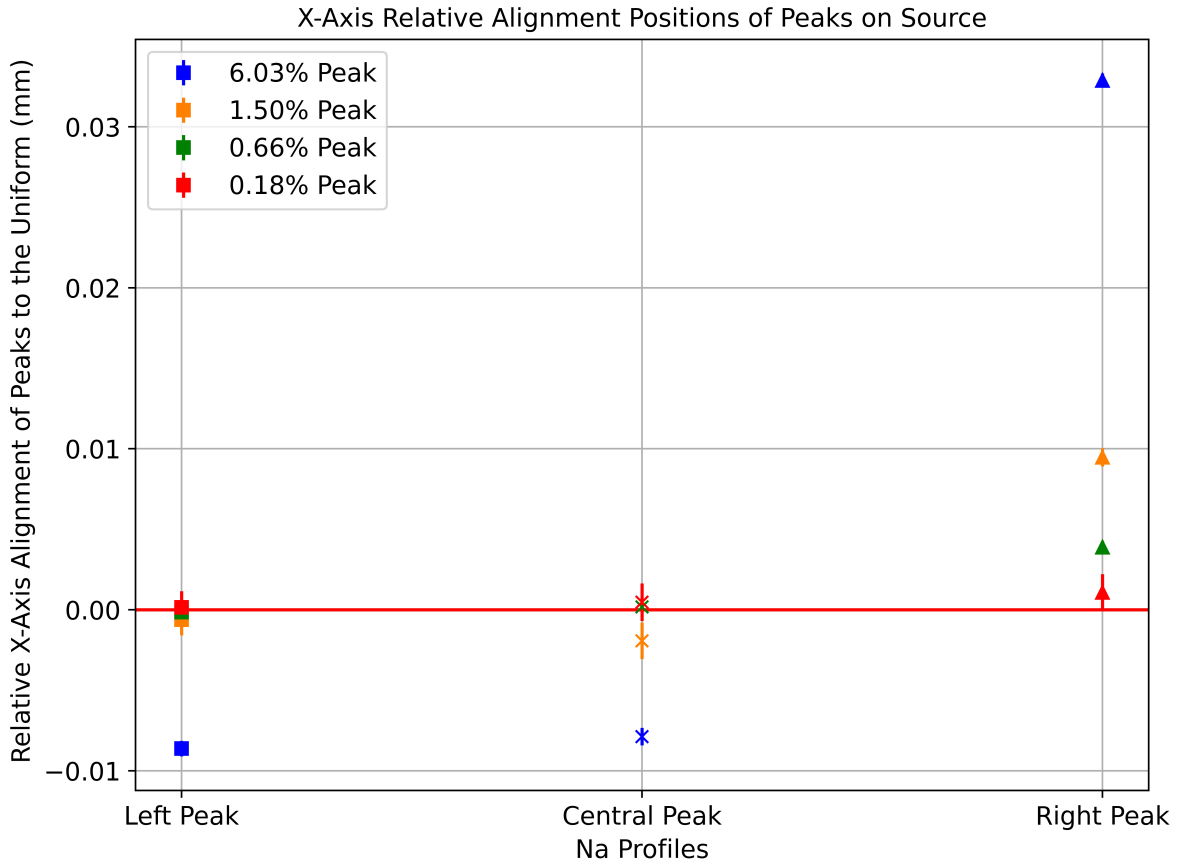

Figure 5.32: The plot shows the relative X-axis alignment positions of peaks on the source compared to the uniform sources for different intensity profiles. The x-axis represents the positions of the left, central, and right peaks. The y-axis shows the relative alignment positions in millimeters. The different colored markers correspond to the intensity profiles with peak increases of 6.03%, 1.50%, 0.66%, and 0.18%. The red line indicates the alignment position of the uniform source for reference.

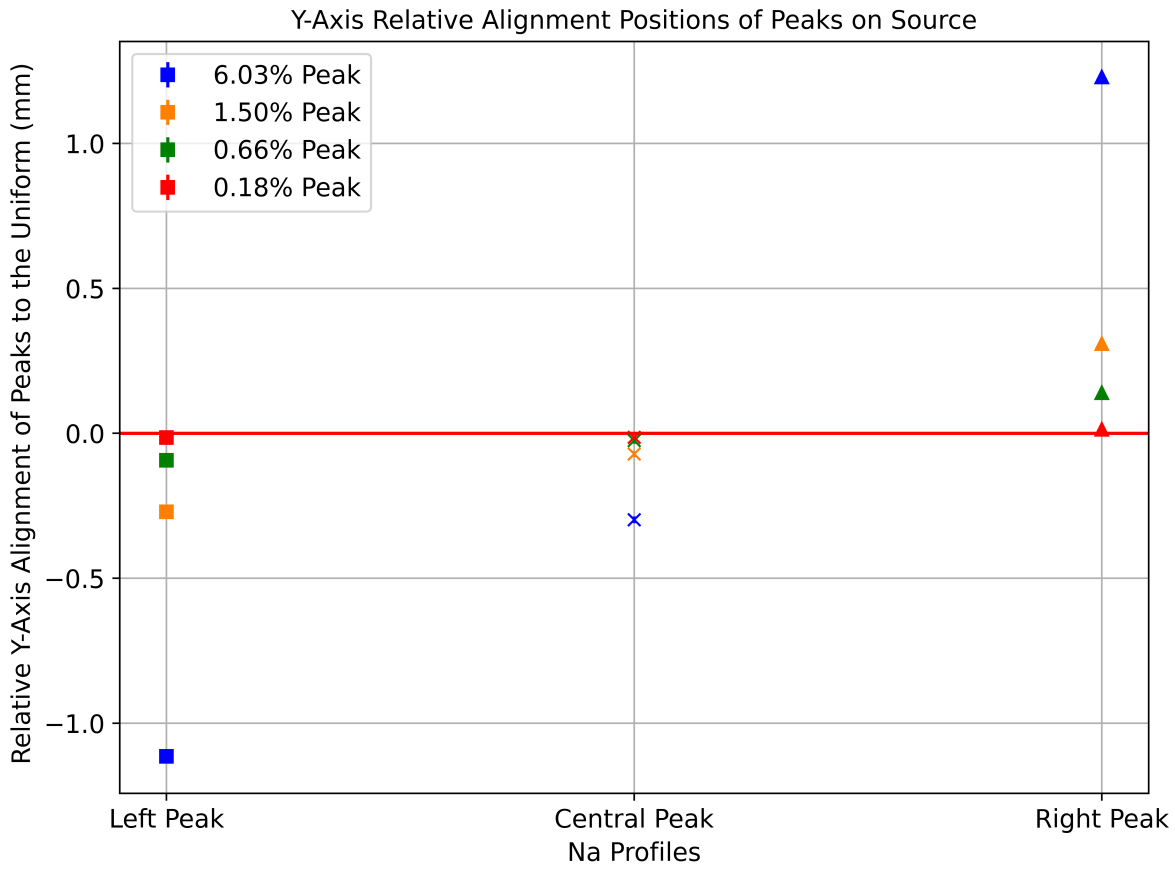

Figure 5.33: The plot shows the relative Y-axis alignment positions of peaks compared to uniform sources for different intensity profiles. The x-axis represents the left, central, and right peaks, while the y-axis shows the alignment positions in millimeters. Colored markers indicate intensity profiles with peak increases of 6.03%, 1.50%, 0.66%, and 0.18%. The red line represents the uniform source alignment position.

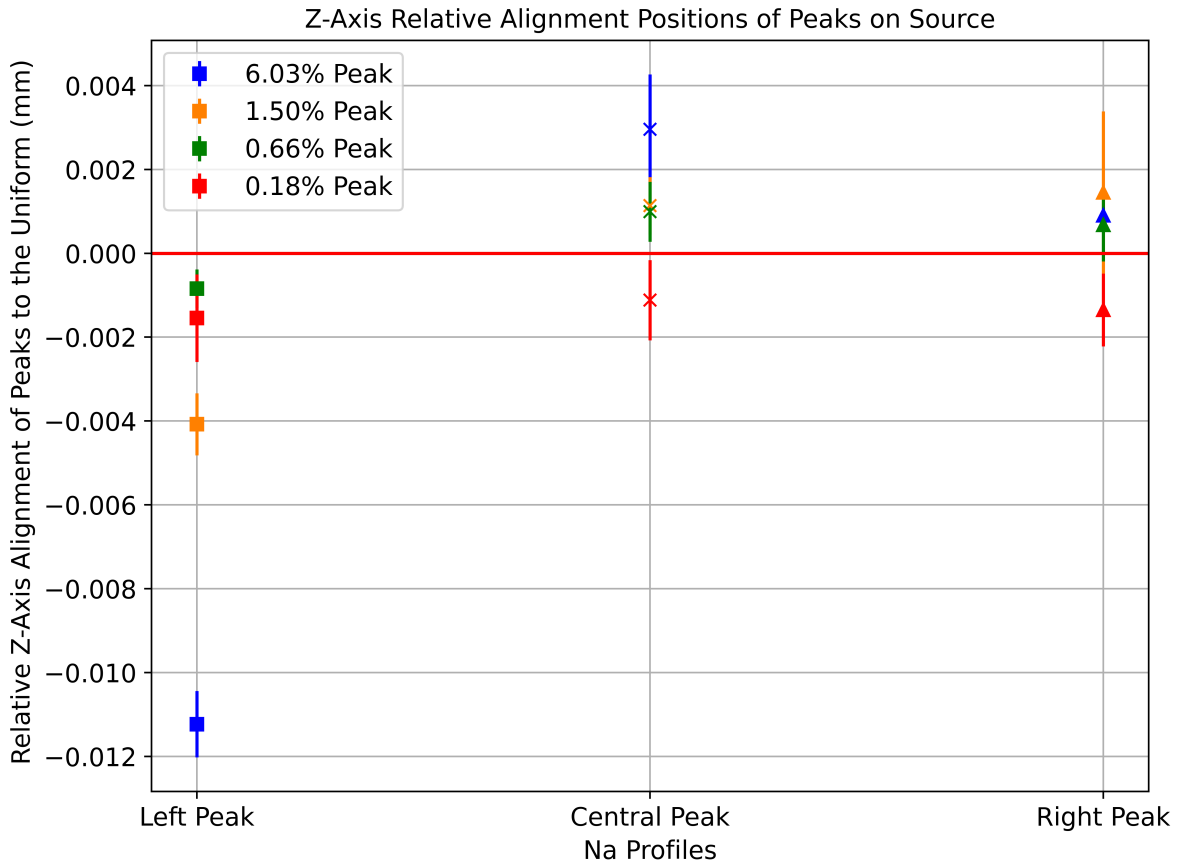

Figure 5.34: The plot shows the relative Y-axis alignment positions of peaks compared to uniform sources for different intensity profiles. The x-axis represents the left, central, and right peaks, while the y-axis shows the alignment positions in millimeters. Colored markers indicate intensity profiles with peak increases of 6.03%, 1.50%, 0.66%, and 0.18%. The red line represents the uniform source alignment position.

From the results, it is evident that changes in the X and Y-axis alignment positions are more consistent than changes in the Z-axis alignment. This consistency aligns with our expectations, as variations in peak intensities at the same positions should predominantly affect the X and Y axes.
We found that changes made around the center of the source produce minimal differences in the alignment position. This indicates that, with a uniform source, the alignment remains nearly the same as the source with a central peak, unless the rest of the source is very dim and a very bright peak is introduced, as seen with the 6.03% intensity increase. In contrast, the left and right peaks produce significant changes in alignment positions. Even a small intensity peak increase of 0.66% is easily detectable, demonstrating the sensitivity of the I-WFS to changes in peak intensity and position.

5.7 Next Steps

Currently, work is on-going to replicate realistic sky conditions on the Ingot bench, where the Na-profile on the screen changes continuously following realistic Na profiles and the

Ingot with subsequent iterations keeps itself aligned to these changing sources. Add-on to this will be to include mixed misalignments of the LGS source. Also there work in progress in order to introduce changes on the optical setup to accommodate a DM on optical path and get closer to the ELT parameters. The introduction of the DM will allow to simulate the atmospheric turbulence and close the loop on the bench, verifying the correction of distortion using the Ingot-WFS.
Other future plans also include conducting comparisons and evaluations with different WFSs, introducing a SH-WFS of the bench, providing valuable insights into the strengths and limitations of I-WFS.
Also, we are planning to introduce a custom ingot prism with enhanced characteristics in terms of material, optical quality, coating characteristics, geometrical properties. Finally the team plans to test it on a real medium-sized telescope, equipped with a side laser launcher, allowing us to evaluate its performance under real observational conditions.

6 Conclusions

The wavefront sensors are key element in an AO system and use reference sources to correct for atmospheric turbulence. When a bright star is available but at an angular distance from the target larger than the isoplanatic angle, the distortions in the wavefront can only be partially corrected. In such cases LGSs are used and in particular Na-LGS will be used on upcoming large telescopes. One of the main limitations with Na-LGS is due its elongated geometry originated by the thickness of the Sodium layer. This thesis work focuses on investigating and analysing and characterizing the I-WFS proposed by [15] to solve the problem of elongation, which is decreasing the WFS performance while using with Na-LGS with an extremely large telescope . Currently, a 3-pupil design of I-WFS is under testing at INAF-OAPd Ingot test-bench. It is an extended, roof-shaped prism designed to capture the entire 3D focal volume of the Na-LGS. The Ingot test-bench is designed to simulate the characteristics of ELT and includes an OLED screen to replicate the Na-LGS source, located on the edge of the telescope.

I started from existing calibration and alignment procedures and improved them for the purposes of this thesis work. As a first step, in order to test the I-WFS response to the Na-LGS in a more realistic way, we needed a new OLED screen providing more flexibility in operation and reproducing the Na-LGS. For this purpose, we introduced a new OLED screen, allowing to reproduce the intensity variability throughout the profile and change in time, according to real LGS profiles data acquired on-sky. As a first step I characterized this screen and found that the brightness, the SNR and Flux of the New screen was higher than the Old screen, avoiding to introduce any issues related to a lack of light reaching the I-WFS connected to the used screen. The brightness has been found to be 3.5 times brighter than the Old Screen. Afterwards, we focused in the I-WFS and found that if calibrated once with a uniform standard source the I-WFS is able to align even when the source is moved vertically on the screen. Collection of data for this tests also helped us prove that the Ingot optical bench has 1:1 re-imaging relay as it was designed and tested for in simulations. The New screen was chosen based on its ability that each pixel can be assigned a different brightness and during my work, we successfully reproduced Na-LGS on it using the sodium density profile data from LIDAR. We tested the I-WFS with randomly chosen sodium profiles on the screen and I-WFS successfully aligned in accordance with the theoretical predictions. Further, we aimed at characterizing the sensitivity to respond at small variations in the profile and we found that the I-WFS is able to respond to as small as 0.66% peak in intensity in any part of the source.

So far these results have helped us proving, understanding and characterizing the response of I-WFS to variable Na-LGS profiles on the test bench. In the next future, the

Ingot bench will be integrated with a DM which will help us test the system in closed-loop, with the DM used to apply and to correct the turbulence. Also, we are planning to introduce a SH-WFS on the bench for further comparison of performance. Final step of the experiment will be to have the I-WFS ready for on-sky testing.

Bibliography

[1] John W. Hardy. *Adaptive Optics for Astronomical Telescopes*. Oxford University Press, 1998.

[2] Galileo Galilei. *Sidereus nuncius magna, longeque admirabilia spectacula pandens lunae facie, fixis innumeris, lacteo circulo, stellis nebulosis, ... Galileo Galileo : nuper a se reperti beneficio sunt observata in apprime vero in quatuor planetis circa Iovis stellam disparibus intervallis, atque periodis, celeritate mirabili circumvolutis ... atque Medicea sidera nuncupandos decrevit*. 1610.

[3] Galileo Galilei, Marcus Welser, and Angelo de Filiis. *Istoria E dimostrazioni intorno alle macchie solari E loro accidenti comprese in tre lettere scritte all'illvstrissimo signor Marco Velseri ...* 1613.

[4] Mr. Newtons. Mr. Newtons Answer to the Foregoing Letter Further Explaining His Theory of Light and Colors, and Particularly That of Whiteness; together with His Continued Hopes of Perfecting Telescopes by Reflections Rather than Refractions. *Philosophical Transactions of the Royal Society of London Series I*, 8:6087–6092, January 1673.

[5] Kaj Aa. Strand. The 60-inch Astrometric Reflector of the U. S. Naval Observatory. , 65:502, January 1960.

[6] Lewis M. Rutherfurd. Astronomical Observations with the Spectroscope. *American Journal of Science and Arts*, 35:71–77, May 1863.

[7] Horace W. Babcock. An Automatic Guider for Astronomical Telescopes. *Review of Scientific Instruments*, 18:854–855, November 1947.

[8] Harold D. Babcock. The Derivation of Vacuum Wave Numbers and the Reduction of Measured Wave Lengths to Standard Atmospheric Conditions. , 111:60, January 1950.

[9] Harold W. Babcock. The Possibility of Compensating Astronomical Seeing. , 65(386):229, October 1953.

[10] Theodore H. Maiman. Stimulated Optical Radiation in Ruby. , 187(4736):493–494, August 1960.

[11] Ronald R. Parenti and Richard J. Sasiela. Laser-guide-star systems for astronomical applications. *J. Opt. Soc. Am. A*, 11(1):288–309, Jan 1994.

[12] V. P. Linnik. On the Possibility of Reducing the Influence of Atmospheric Seeing

on the Image Quality of Stars. In Fritz Merkle, editor, *European Southern Observatory Conference and Workshop Proceedings*, volume 48 of *European Southern Observatory Conference and Workshop Proceedings*, page 535, January 1994.

[13] Domenico Bonaccini Calia, Y. Feng, W. Hackenberg, R. Holzlöhner, L. Taylor, and S. Lewis. Laser Development for Sodium Laser Guide Stars at ESO. *The Messenger*, 139:12–19, March 2010.

[14] S. Kellner, R. Ragazzoni, W. Gässler, E. Diolaiti, J. Farinato, C. Adriciaco, R. Meyers, T. Morris, and A. Ghedina. Pigs - a new wavefront sensor concept for elts. In Wolfgang Brandner and Markus E. Kasper, editors, *Science with Adaptive Optics*, pages 31–34, Berlin, Heidelberg, 2005. Springer Berlin Heidelberg.

[15] Roberto Ragazzoni, Elisa Portaluri, Valentina Viotto, Marco Dima, Maria Bergomi, Federico Biondi, Jacopo Farinato, Elena Carolo, Simonetta Chinellato, Davide Greggio, Marco GUilleuszik, Demetrio Magrin, Luca Marafatto, and Daniele Vassallo. Ingot laser guide stars wavefront sensing. In *Proceedings of the Adaptive Optics for Extremely Large Telescopes 5*, AO4ELT5. Instituto de Astrofísica de Canarias (IAC), 2017.

[16] George B. Airy. On the Diffraction of an Object-glass with Circular Aperture. *Transactions of the Cambridge Philosophical Society*, 5:283, January 1835.

[17] Kalyan Kumar Radhakrishnan Santhakumari. *Maximising the Science Returns of the LINC-NIRVANA Multi-Conjugated Adaptive Optics System*. Ph.d. thesis, Max-Planck-Institut f¨ ur Astronomie / Universit¨ at Heidelberg, 2017.

[18] Tania Sofia Gomes Machado. *Characterisation of a new Laser Guide Star Wavefront Sensor*. Master's thesis, Padova, Italy, 2023.

[19] Osborne Reynolds. An Experimental Investigation of the Circumstances Which Determine Whether the Motion of Water Shall Be Direct or Sinuous, and of the Law of Resistance in Parallel Channels. *Philosophical Transactions of the Royal Society of London Series I*, 174:935–982, January 1883.

[20] Henry Abarbanel, Darryl Holm, Jerrold Marsden, and Tudor Ratiu. Richardson number criterion for the nonlinear stability of three-dimensional stratified flow. *Physical Review Letters*, 52, 06 1984.

[21] Katepalli R. Sreenivasan. The passive scalar spectrum and the Obukhov–Corrsin constant. *Physics of Fluids*, 8(1):189–196, 01 1996.

[22] Ferruccio Mosetti. *REYNOLD'S NUMBERReynold's number*, pages 686–688. Springer US, New York, NY, 1984.

[23] A. N. Kolmogorov. The local structure of turbulence in incompressible viscous fluid for very large reynolds numbers. *Proceedings: Mathematical and Physical Sciences*, 434(1890):9–13, 1991.

[24] Andrey Nikolaevich Kolmogorov. Dissipation of Energy in Locally Isotropic Turbulence. *Akademiia Nauk SSSR Doklady*, 32:16, April 1941.

[25] Frank D. Eaton and Gregory D. Nastrom. Preliminary estimates of the vertical

profiles of inner and outer scales from white sands missile range, new mexico, vhf radar observations. *Radio Science*, 33(4):895–903, 1998.

[26] R. Conan, R. Avila, L. J. Sánchez, A. Ziad, F. Martin, J. Borgnino, O. Harris, S. I. González, R. Michel, and D. Hiriart. Wavefront outer scale and seeing measurements at San Pedro Mártir Observatory. , 396:723–730, December 2002.

[27] J. Gordon Leishman. *Introduction to Aerospace Flight Vehicles*. None, 2022.

[28] V. I. Tatarski, R. A. Silverman, and Nicholas Chako. Wave Propagation in a Turbulent Medium. *Physics Today*, 14(12):46, January 1961.

[29] Sebastian E. Egner. *Multi-Conjugate Adaptive Optics for LINC-NIRVANA*. Ph.d. thesis, University of Heidelberg, Germany, 2006.

[30] C. E. Coulman, J. Vernin, Y. Coqueugniot, and J. L. Caccia. Outer scale of turbulence appropriate to modeling refractive-indexstructure profiles. *Appl. Opt.*, 27(1):155–160, Jan 1988.

[31] D. L. Fried. Optical Resolution Through a Randomly Inhomogeneous Medium for Very Long and Very Short Exposures. *Journal of the Optical Society of America (1917-1983)*, 56(10):1372, October 1966.

[32] Vik Dhillon. Adaptive optics overcome seeing, 2017. Accessed: 2024-09-16.

[33] David L. Fried. Anisoplanatism in adaptive optics. *Journal of the Optical Society of America (1917-1983)*, 72(1):52, January 1982.

[34] Francois Roddier. *Adaptive Optics in Astronomy*. Cambridge University Press, 1999.

[35] A. Buffington, F. S. Crawford, R. A. Muller, A. J. Schwemin, and R. G. Smits. Correction of atmospheric distortion with an image sharpening telescope. *Journal of the Optical Society of America (1917-1983)*, 67:298–303, March 1977.

[36] Roberto Biasi, Daniele Gallieni, Piero Salinari, Armando Riccardi, and Paolo Mantegazza. Contactless thin adaptive mirror technology: past, present, and future. In Brent L. Ellerbroek, Michael Hart, Norbert Hubin, and Peter L. Wizinowich, editors, *Adaptive Optics Systems II*, volume 7736, page 77362B. International Society for Optics and Photonics, SPIE, 2010.

[37] Alan T. Tokunaga. Chapter 51 - new generation ground-based optical/infrared telescopes. In Tilman Spohn, Doris Breuer, and Torrence V. Johnson, editors, *Encyclopedia of the Solar System (Third Edition)*, pages 1089–1105. Elsevier, Boston, third edition edition, 2014.

[38] Ben C Platt and Roland Shack. History and principles of shack-hartmann wavefront sensing. *Journal of Refractive Surgery*, 17(5):S573–S577, 2001.

[39] Weiyao Zou and Jannick Rolland. Differential wavefront curvature sensor. 08 2005.

[40] William Thompson, Darryl Gamroth, Christian Marois, and Olivier Lardière. Real-time adaptive optics control with a high level programming language, 2024.

[41] W.H. Southwell. Wave-front estimation from wave-front slope measurements. *J. Opt. Soc. Am.*, 70(8):998–1006, Aug 1980.

[42] von F. Zernike. Beugungstheorie des schneidenver-fahrens und seiner verbesserten form, der phasenkontrastmethode. *Physica*, 1(7):689–704, May 1934.

[43] Robert J. Noll. Zernike polynomials and atmospheric turbulence∗. *J. Opt. Soc. Am.*, 66(3):207–211, Mar 1976.

[44] Vladimir Toporovsky, Alexis Kudryashov, Arkadiy Skvortsov, Alexey Rukosuev, Vadim Samarkin, and Ilya Galaktionov. State-of-the-art technologies in piezoelectric deformable mirror design. *Photonics*, 9(5), 2022.

[45] Takuso Sato, Hiromi Ishikawa, Osamu Ikeda, Shoichiro Nomura, and Kenji Uchino. Deformable 2-d mirror using multilayered electrostrictors. *Appl. Opt.*, 21(20):3669–3672, Oct 1982.

[46] David Dayton, Steve Sandven, John Gonglewski, Steve Browne, Samuel Rogers, and Scot McDermott. Adaptive optics using a liquid crystal phase modulator in conjunction with a shack-hartmann wave-front sensor and zonal control algorithm. *Opt. Express*, 1(11):338–346, Nov 1997.

[47] Ryan Luder, Michael Hart, Krysta Pavlica, and Olivia Fehlberg. Voice-coil array development for a deformable mirror. 2019. Publisher Copyright: © 2019 AO4ELT 2019 - Proceedings 6th Adaptive Optics for Extremely Large Telescopes. All rights reserved.; 6th International Conference on Adaptive Optics for Extremely Large Telescopes, AO4ELT 2019 ; Conference date: 09-06-2019 Through 14-06-2019.

[48] Kai Sum Chan and H. F. Chau. Reducing the impact of adaptive optics lag on optical and quantum communications rates from rapidly moving sources, 2023.

[49] ESO. Ao modes, 2004. Accessed: 2024-09-18.

[50] Guido Agapito, Lorenzo Busoni, Cedric Plantet, Giulia Carla, Marco Bonaglia, and Paolo Ciliegi. Ngss acquisition in morfeo. 2023.

[51] Jacques M. Beckers. Adaptive Optics for Astronomy: Principles, Performance, and Applications. , 31:13–62, January 1993.

[52] Laird A. Thompson and Chester S. Gardner. Excimer Laser Guide Star Techniques For Adaptive Imaging In Astronomy. In Francois J. Roddier, editor, *Active Telescope Systems*, volume 1114, pages 184 – 190. International Society for Optics and Photonics, SPIE, 1989.

[53] Roberto Ragazzoni, Emiliano Diolaiti, and Massimiliano Tordi. Rayleigh laser guide star wavefront sensing. In Robert K. Tyson, Domenico Bonaccini, and Michael C. Roggemann, editors, *Adaptive Optics Systems and Technology II*, volume 4494 of *Society of Photo-Optical Instrumentation Engineers (SPIE) Conference Series*, pages 252–258, February 2002.

[54] Y. Li, T.-Y. Huang, J. Urbina, F. Vargas, and W. Feng. On the relationship between the mesospheric sodium layer and the meteoric input function. *Annales Geophysicae*, 42(1):285–299, 2024.

[55] Ronald Holzlohner, Simon Rochester, Thomas Pfrommer, Domenico Calia, Dmitry Budker, James Higbie, and Wolfgang Hackenberg. Laser guide star return flux simulations based on observed sodium density profiles. *Proceedings of SPIE - The International Society for Optical Engineering*, 7736, 07 2010.

[56] Roberto Ragazzoni and Francois Rigaut. Fixing the LGS tilt problem using tomography. , 338:L100–L102, October 1998.

[57] F. Rigaut and E. Gendron. Laser guide star in adaptive optics: the tilt determination problem. , 261:677–684, August 1992.

[58] S. J. Thomas, S. Adkins, D. Gavel, T. Fusco, and V. Michau. Study of optimal wavefront sensing with elongated laser guide stars. , 387(1):173–187, June 2008.

[59] Stefanie Milam, John Mather, Eliad Peretz, Isabel Kain, Richard Slonaker, John O'Meara, Sara Seager, and Tiffany Hoerbelt. Orbiting Configurable Artificial Star (ORCAS) for Visible Adaptive Optics from the Ground. In *Planets 2020, Ground and Space Observatories: a Joint Venture to Planetary Science*, page 16, March 2020.

[60] Dustin C. Johnston. *Increasing the corrected field of view of an adaptive optical telescope*. PhD thesis, Wright-Patterson Air Force Base, Ohio, December 1992.

[61] Norbert Hubin, Robin Arsenault, Ralf Conzelmann, Bernard Delabre, Miska Le Louarn, Stefan Stroebele, and Remko Stuik. Ground layer adaptive optics. *Comptes Rendus Physique*, 6(10):1099–1109, 2005. Multi-Conjugate Adaptive Optics for very large telescopes.

[62] B. L. Ellerbroek. Multi-Conjugate Adaptive Optics for Wide Field-of-View Atmospheric Turbulence Compensation. In Richard R. Radick, editor, *Real Time and Post Facto Solar Image Correction*, page 15, December 1993.

[63] Eric Tatulli and A. N. Ramaprakash. Laser tomography adaptive optics: a performance study. *Journal of the Optical Society of America A*, 30(12):2482, November 2013.

[64] Marco Xompero, Christophe Giordano, Marco Bonaglia, Gianluca Di Rico, Guido Agapito, Simone Esposito, Andrea Tozzi, Nicoletta Sanna, Ernesto Oliva, and Alessandro Marconi. ELT-HIRES the high resolution spectrograph for the ELT: implementing exoplanet atmosphere reflection detection with a SCAO module. In Laird M. Close, Laura Schreiber, and Dirk Schmidt, editors, *Adaptive Optics Systems VI*, volume 10703 of *Society of Photo-Optical Instrumentation Engineers (SPIE) Conference Series*, page 1070341, July 2018.

[65] J. M. Beckers. Increasing the Size of the Isoplanatic Patch with Multiconjugate Adaptive Optics. In M. H. Ulrich, editor, *Very Large Telescopes and their Instrumentation, Vol. 2*, volume 30 of *European Southern Observatory Conference and Workshop Proceedings*, page 693, October 1988.

[66] Andrei Tokovinin, Miska Le Louarn, and Marc Sarazin. Isoplanatism in a multiconjugate adaptive optics system. *Journal of the Optical Society of America A*, 17(10):1819–1827, October 2000.

[67] Roberto Ragazzoni, Jacopo Farinato, and Enrico Marchetti. Adaptive optics for 100-m-class telescopes: new challenges require new solutions. In Peter L. Wizinowich, editor, *Adaptive Optical Systems Technology*, volume 4007, pages 1076 – 1087. International Society for Optics and Photonics, SPIE, 2000.

[68] Robin Arsenault, Jaime Alonso, Henri Bonnet, Joar Brynnel, Bernard Delabre, Rachael Donaldson, Christophe Dupuy, Enrico Fedrigo, Jacopo Farinato, N. Hubin, Liviu Ivanescu, Markus Kasper, J. Paufique, S. Rossi, Sebastien Tordo, S. Ströbele, J.-L Lizon, Pierre Gigan, Francoise Delplancke, and Roland Reiss. Macao-vlti: an adaptive optics system for the eso interferometer. 02 2003.

[69] Maria Bergomi. *PYRAMID WAVEFRONT SENSORS FOR ASTRONOMY AND FOR THE HUMAN EYE*. Ph.d. thesis, Padova, Italy, 2012.

[70] J. Vallerga, Jason McPhate, Anton Tremsin, Oswald Siegmund, Bettina Mikulec, and Allan Clark. Optically sensitive medipix2 detector for adaptive optics wavefront sensing. *Nuclear Instruments and Methods in Physics Research Section A: Accelerators, Spectrometers, Detectors and Associated Equipment*, 546:263–269, 07 2005.

[71] L. Schreiber, E. Diolaiti, C. Arcidiacono, T. Pfrommer, R. Holzlöhner, M. Lombini, and P. Hickson. Impact of sodium layer variations on the performance of the E-ELT MCAO module. In Enrico Marchetti, Laird M. Close, and Jean-Pierre Véran, editors, *Adaptive Optics Systems IV*, volume 9148, page 91486Q. International Society for Optics and Photonics, SPIE, 2014.

[72] Matteo Lombini, Laura Schreiber, Emiliano Diolaiti, and Fausto Cortecchia. Optical solution to spot elongation in laser guide stars wavefront sensors for Extremely Large Telescopes. *Monthly Notices of the Royal Astronomical Society*, 510(3):3876–3884, 12 2021.

[73] Laura Schreiber, Matteo Lombini, Italo Foppiani, Emiliano Diolaiti, Jean-Marc Conan, and Enrico Marchetti. An optical solution to the LGS spot elongation problem. In Norbert Hubin, Claire E. Max, and Peter L. Wizinowich, editors, *Adaptive Optics Systems*, volume 7015, page 70151O. International Society for Optics and Photonics, SPIE, 2008.

[74] F. Roddier, F. Forbes, S. Shaklan, and C. Pinches. Curvature sensing and compensation. *LEST Foundation, Technical Report*, 28:169–178, January 1987.

[75] Simone Di Filippo, Davide Greggio, Maria Bergomi, Kalyan Kumar Radhakrishnan Santhakumari, Elisa Portaluri, Carmelo Arcidiacono, Valentina Viotto, Roberto Ragazzoni, Marco Dima, Luca Marafatto, Jacopo Farinato, and Demetrio Magrin. Laboratory testing of the ingot wfs, 2022.

[76] Roberto Ragazzoni. Pupil plane wavefront sensing with an oscillating prism. *Journal of Modern Optics*, 43(2):289–293, 1996.

[77] S. Esposito and A. Riccardi. Pyramid Wavefront Sensor behavior in partial correction Adaptive Optic systems. , 369:L9–L12, April 2001.

[78] A. Meduri, L. Bergandi, P. Perroni, F. Silvagno, and P. Aragona. Oral l-cysteine supplementation enhances the long term-effect of topical basic fibroblast growth fac-

tor (bfgf) in reducing the corneal haze after photorefractive keratectomy in myopic patients. *Pharmaceuticals*, 13:67, 2020.

[79] Valentina Viotto, Elisa Portaluri, Carmelo Arcidiacono, Roberto Ragazzoni, Maria Bergomi, Simone Di Filippo, Marco Dima, Jacopo Farinato, Davide Greggio, Demetrio Magrin, and Luca Marafatto. Dealing with the cigar: preliminary performance estimation of an INGOT WFS. In Laird M. Close, Laura Schreiber, and Dirk Schmidt, editors, *Adaptive Optics Systems VI*, volume 10703, page 107030V. International Society for Optics and Photonics, SPIE, 2018.

[80] Roberto Ragazzoni, Valentina Viotto, Elisa Portaluri, Maria Bergomi, Davide Greggio, Simone Di Filippo, Kalyan Radhakrishnan, Gabriele Umbriaco, Marco Dima, Demetrio Magrin, Jacopo Farinato, Luca Marafatto, Carmelo Arcidiacono, and Federico Biondi. Pupil plane wavefront sensing for extended and 3d sources, 2020.

[81] Elisa Portaluri, Valentina Viotto, Roberto Ragazzoni, Carmelo Arcidiacono, Davide Greggio, Kalyan Kumar Radhakrishnan Santhakumari, Maria Bergomi, Simone Di Filippo, Jacopo Farinato, and Demetrio Magrin. Evaluating the performance of an ingot wavefront sensor for the elt: good news from simulations. page 194, 12 2020.

[82] Simone Di Filippo, Davide Greggio, Maria Bergomi, Kalyan Kumar Radhakrishnan Santhakumari, Elisa Portaluri, Carmelo Arcidiacono, Valentina Viotto, Roberto Ragazzoni, Marco Dima, Luca Marafatto, Jacopo Farinato, and Demetrio Magrin. Laboratory testing of the Ingot WFS. In Laura Schreiber, Dirk Schmidt, and Elise Vernet, editors, *Adaptive Optics Systems VIII*, volume 12185 of *Society of Photo-Optical Instrumentation Engineers (SPIE) Conference Series*, page 121854V, August 2022.

[83] Kalyan Kumar Radhakrishnan Santhakumari, Davide Greggio, Maria Bergomi, Simone Di Filippo, Valentina Viotto, Elisa Portaluri, Carmelo Arcidiacono, Marco Dima, Luigi Lessio, Luca Marafatto, Tommaso Furieri, S. Bonora, and Roberto Ragazzoni. Aligning and testing the ingot wavefront sensor in the lab. page 241, 12 2020.

[84] Carmelo Arcidiacono, Simone Di Filippo, Davide Greggio, Kalyan Kumar Radhakrishnan Santakumari, Elisa Portaluri, Maria Bergomi, Valentina Viotto, Demetrio Magrin, Roberto Ragazzoni, Luca Marafatto, Marco Dima, Jacopo Farinato, Pierre Janin-Potiron, Thierry Fusco, Benoit Neichel, Olivier Fauvarque, and Lauren Schatz. Ingot wavefront sensor: from the Fourier End2End numerical simulation to the LOOPS test bench. In Laura Schreiber, Dirk Schmidt, and Elise Vernet, editors, *Adaptive Optics Systems VII*, volume 11448 of *Society of Photo-Optical Instrumentation Engineers (SPIE) Conference Series*, page 1144868, December 2020.

[85] Carmelo Arcidiacono, Simone Di Filippo, Davide Greggio, Kalyan Kumar Radhakrishnan Santhakumari, Elisa Portaluri, Maria Bergomi, Valentina Viotto, Demetrio Magrin, Roberto Ragazzoni, Luca Marafatto, Marco Dima, Jacopo Farinato, Pierre Janin-Potiron, Thierry Fusco, Benoit Neichel, Olivier Fauvarque, and Lauren Schatz. Ingot wavefront sensor: from the fourier end2end numerical simulation to the loops test bench. page 250, 12 2020.

[86] Marín, Julio C., Pozo, Diana, and Curé, Michel. Estimating and forecasting the precipitable water vapor from goes satellite data at high altitude sites. *AA*, 573:A41, 2015.

[87] ESO. Elt eso, 2018. Accessed: 2024-10-04.

[88] Lorenzo Busoni, Guido Agapito, Alessandro Ballone, Alfio Puglisi, Alexander Goncharov, Amedeo Petrella, Amico Di Cianno, Andrea Balestra, Andrea Baruffolo, Andrea Bianco, Andrea Di Dato, Angelo Valentini, Benedetta Di, Benoit Sassolas, Bernardo Salasnich, Sylvain Arcidiacono, Tommaso Lapucci, Ugo Di Giammatteo, Vincenzo Cianniello, Vincenzo de Caprio, and Zoltan et al. Hubert. MORFEO enters final design phase. In *Adaptive Optics for Extremely Large Telescopes (AO4ELT7)*, page 129, June 2023.

[89] Yann Clénet, Tristan Buey, Eric Gendron, Sonia Karkar, Fabrice Vidal, Mathieu Cohen, Frédéric Chapron, Arnaud Sevin, Simone Thijs, Sylvestre Taburet, Bruno Borgo, Jean-Michel Huet, Alexandre Blin, Olivier Dupuis, Julien Gaudemard, Florian Ferreira, Jordan Raffard, Fanny Chemla, Vincent Lapeyrère, Vincent Deo, Arielle Bertrou-Cantou, Nicolas Galland, Sylvain Guieu, Eric Meyer, Nicolas Gautherot, Emmanuel Tisserand, Hervé Locatelli, François Meyer, Amal Zidi, Caroline Kulcsár, Henri-François Raynaud, Benoit Sassolas, Laurent Pinard, Christophe Michel, Damien Gratadour, Bertrand Le Ruyet, Roderick Dembet, Manuel Ortiz, Claude Collin, Vartan Arslanyan, Bosko Doncic, Lahoucine Ghouchou, Issan Ibn Taïeb, Pierre Baudoz, Elsa Huby, Gérard Rousset, Sebastian Rabien, Veronika Hörmann, Eckhard Sturm, and Richard Davies. The MICADO first light imager for the ELT: overview of the SCAO module at its final design. In Laura Schreiber, Dirk Schmidt, and Elise Vernet, editors, *Adaptive Optics Systems VIII*, volume 12185, page 121854S. International Society for Optics and Photonics, SPIE, 2022.

[90] Richard Davies, Veronika Hörmann, Sebastian Rabien, Eckhard Sturm, João Alves, Yann Clénet, Jari Kotilainen, Florian Lang-Bardl, Harald Nicklas, Jörg-Uwe Pott, Eline Tolstoy, Benedetta Vulcani, and The MICADO Consortium. Micado: The multi-adaptive optics camera for deep observations. *Published in The Messenger vol. 182*, pp. 17-21:March 2021., 2021.

[91] Niranjan Thatte, Matthias Tecza, Hermine Schnetler, Benoit Neichel, Dave Melotte, Thierry Fusco, Vanessa Ferraro-Wood, Fraser Clarke, Ian Bryson, Kieran O'Brien, Mario Mateo, Begoña Garcia Lorenzo, Chris Evans, Nicolas Bouché, Santiago Arribas, and The HARMONI Consortium. Harmoni: the elt's first-light near-infrared and visible integral field spectrograph. *Published in The Messenger vol. 182*, pp. 7-12:March 2021., 2021.

[92] A. Marconi, M. Abreu, V. Adibekyan, V. Alberti, S. Albrecht, J. Alcaniz, M. Aliverti, C. Allende Prieto, J. D. Alvarado Gómez, C. S. Alves, P. J. Amado, M. Amate, M. I. Andersen, S. Antoniucci, E. Artigau, C. Bailet, C. Baker, V. Baldini, A. Balestra, S. A. Barnes, and F. Baron et al. Andes, the high resolution spectrograph for the elt: science goals, project overview and future developments, 2024.

[93] Bernhard Brandl. Status, Observing Modes, and expected Performance of the Mid-Infrared ELT Imager and Spectrograph METIS. In *EAS2024*, page 2554, July 2024.

[94] Paolo Ciliegi, Guido Agapito, Matteo Aliverti, Francesca Annibali, Carmelo Arcidiacono, Nicolò Azzaroli, Andrea Balestra, Ivano Baronchelli, Andrea Baruffolo, Maria Bergomi, Andrea Bianco, Marco Bonaglia, Runa Briguglio, Lorenzo Busoni, Michele Cantiello, Giulio Capasso, Giulia Carlà, Elena Carolo, Enrico Cascone, Simonetta Chinellato, Vincenzo Cianniello, Mirko Colapietro, Jean-Jacques Correia, Giuseppe Cosentino, Domenico D'Auria, Vincenzo De Caprio, Nicholas Devaney, Ivan Di Antonio, Amico Di Cianno, Andrea Di Dato, Ugo Di Giammatteo, Gianluca Di Rico, Mauro Dolci, Christian Eredia, Simone Esposito, Daniela Fantinel, Jacopo Farinato, Philippe Feautrier, Italo Foppiani, Matteo Genoni, Enrico Giro, Laurence Gluck, Alexander Goncharov, Paolo Grani, Davide Greggio, Sylvain Guieu, Marco Gullieuszik, Pierre Haguenauer, Zoltan Hubert, Tommaso Lapucci, Fulvio Laudisio, Miska Le Louarn, Demetrio Magrin, Deborah Malone, Luca Marafatto, Matteo Munari, Sylvain Oberti, Giorgio Pariani, Lorenzo Pettazzi, Cedric Plantet, Elisa Portaluri, Alfio Puglisi, Patrick Rabou, Roberto Ragazzoni, Edoardo Redaelli, Marco Riva, Sylvain Rochat, Gabriele Rodeghiero, Bernardo Salasnich, Salvatore Savarese, Marcello Scalera, Pietro Schipani, Rosanna Sordo, Marie-Helene Sztefek, Angelo Valentini, and Marco Xompero. MAORY/MORFEO at ELT: general overview up to the preliminary design and a look towards the final design. In Laura Schreiber, Dirk Schmidt, and Elise Vernet, editors, *Adaptive Optics Systems VIII*, volume 12185, page 1218514. International Society for Optics and Photonics, SPIE, 2022.

[95] G. Fiorentino, M. Bellazzini, P. Ciliegi, G. Chauvin, S. Douté, V. D'Orazi, E. Maiorano, F. Mannucci, M. Mapelli, L. Podio, P. Saracco, and M. Spavone. MAORY science cases white book. *arXiv e-prints*, page arXiv:1712.04222, December 2017.

[96] E. Portaluri, V. Viotto, R. Ragazzoni, C. Arcidiacono, M. Bergomi, M. Dima, D. Greggio, J. Farinato, and D. Magrin. Simulations of ELT-GMCAO Performance for Deep Field Observations. , 132(1014):084502, August 2020.

[97] L. Girardi, M. A. T. Groenewegen, E. Hatziminaoglou, and L. da Costa. Star counts in the Galaxy. Simulating from very deep to very shallow photometric surveys with the TRILEGAL code. , 436(3):895–915, June 2005.

[98] B. T. Jannuzi and A. Dey. The NOAO Deep Wide-Field Survey. In Ray Weymann, Lisa Storrie-Lombardi, Marcin Sawicki, and Robert Brunner, editors, *Photometric Redshifts and the Detection of High Redshift Galaxies*, volume 191 of *Astronomical Society of the Pacific Conference Series*, page 111, January 1999.

[99] R. Giacconi, P. Rosati, P. Tozzi, M. Nonino, G. Hasinger, C. Norman, J. Bergeron, S. Borgani, R. Gilli, R. Gilmozzi, and W. Zheng. First results from the x-ray and optical survey of the chandra deep field south*. *The Astrophysical Journal*, 551(2):624, apr 2001.

[100] M. Giavalisco, H. C. Ferguson, A. M. Koekemoer, M. Dickinson, D. M. Alexander, F. E. Bauer, J. Bergeron, C. Biagetti, W. N. Brandt, S. Casertano, C. Cesarsky, E. Chatzichristou, C. Conselice, S. Cristiani, L. da Costa, T. Dahlen, D. de Mello, P. Eisenhardt, T. Erben, S. M. Fall, C. Fassnacht, R. Fosbury, A. Fruchter, J. P. Gardner, N. Grogin, R. N. Hook, A. E. Hornschemeier, R. Idzi, S. Jogee, C. Kretchmer, V. Laidler, K. S. Lee, M. Livio, R. Lucas, P. Madau, B. Mobasher, L. A. Moustakas, M. Nonino, P. Padovani, C. Papovich, Y. Park, S. Ravindranath, A. Renzini,

M. Richardson, A. Riess, P. Rosati, M. Schirmer, E. Schreier, R. S. Somerville, H. Spinrad, D. Stern, M. Stiavelli, L. Strolger, C. M. Urry, B. Vandame, R. Williams, and C. Wolf. The Great Observatories Origins Deep Survey: Initial Results from Optical and Near-Infrared Imaging. *The Astrophysical Journal*, 600:L93–L98, 2004.

[101] Nobunari Kashikawa, Kazuhiro Shimasaku, Naoki Yasuda, Masaru Ajiki, Masayuki Akiyama, Hiroyasu Ando, Kentaro Aoki, Mamoru Doi, Shinobu S. Fujita, Hisanori Furusawa, Tomoki Hayashino, Fumihide Iwamuro, Masanori Iye, Hiroshi Karoji, Naoto Kobayashi, Keiichi Kodaira, Tadayuki Kodama, Yutaka Komiyama, Yuichi Matsuda, Satoshi Miyazaki, Yoshihiko Mizumoto, Tomoki Morokuma, Kentaro Motohara, Takashi Murayama, Tohru Nagao, Kyoji Nariai, Kouji Ohta, Sadanori Okamura, Masami Ouchi, Toshiyuki Sasaki, Yasunori Sato, Kazuhiro Sekiguchi, Yasunori Shioya, Hajime Tamura, Yoshiaki Taniguchi, Masayuki Umemura, Toru Yamada, and Makiko Yoshida. The Subaru Deep Field: The Optical Imaging Data*. *Publications of the Astronomical Society of Japan*, 56(6):1011–1023, 12 2004.

[102] N. Scoville and COSMOS Team. COSMOS – Cosmic Evolution Survey. In *American Astronomical Society Meeting Abstracts*, volume 205 of *American Astronomical Society Meeting Abstracts*, page 72.01, December 2004.

[103] Steven V. W. Beckwith, Massimo Stiavelli, Anton M. Koekemoer, John A. R. Caldwell, Henry C. Ferguson, Richard Hook, Ray A. Lucas, Louis E. Bergeron, Michael Corbin, Shardha Jogee, Nino Panagia, Massimo Robberto, Patricia Royle, Rachel S. Somerville, and Megan Sosey. The Hubble Ultra Deep Field. , 132(5):1729–1755, November 2006.

[104] J.-C Cuillandre and E. Bertin. Cfht legacy survey (cfhtls) : a rich data set. 01 2006.

[105] John Canny. A computational approach to edge detection. *IEEE Transactions on pattern analysis and machine intelligence*, (6):679–698, 1986.

[106] Richard O Duda and Peter E Hart. Use of the hough transformation to detect lines and curves in pictures. *Communications of the ACM*, 15(1):11–15, 1972.

[107] Kalyan Kumar Radhakrishnan Santhakumari, Davide Greggio, Maria Bergomi, Simone Di Filippo, Valentina Viotto, Elisa Portaluri, Carmelo Arcidiacono, Marco Dima, Luigi Lessio, Luca Marafatto, Tommaso Furieri, Stefano Bonora, and Roberto Ragazzoni. Aligning and testing the ingot wavefront sensor in the lab. In Laura Schreiber, Dirk Schmidt, and Elise Vernet, editors, *Adaptive Optics Systems VII*, volume 11448 of *Society of Photo-Optical Instrumentation Engineers (SPIE) Conference Series*, page 1144860, December 2020.

[108] Simone Di Filippo. *The Ingot Wavefront Sensor: Dealing with extended sources in Astronomy*. Ph.d. thesis, Padova, Italy, 2022.

[109] Thomas Pfrommer and Paul Hickson. High-resolution mesospheric sodium observations for extremely large telescopes. In Brent L. Ellerbroek, Michael Hart, Norbert Hubin, and Peter L. Wizinowich, editors, *Adaptive Optics Systems II*, volume 7736 of *Society of Photo-Optical Instrumentation Engineers (SPIE) Conference Series*, page 773620, July 2010.

[110] Tania S. G. Machado, Simone Di Filippo, Kalyan K. R. Santhakumari, Maria

Bergomi, Davide Greggio, Elisa Portaluri, Dheeraj Malik, Cesar Nesme, Carmelo Arcidiacono, Alessandro Ballone, Federico Battaini, Valentina Viotto, Roberto Ragazzoni, Marco Dima, Luca Marafatto, Jacopo Farinato, Demetrio Magrin, Luigi Lessio, and Gabriele Umbriaco. New developments on the Ingot WFS laboratory testing. In Kathryn J. Jackson, Dirk Schmidt, and Elise Vernet, editors, *Adaptive Optics Systems IX*, volume 13097, page 130973K. International Society for Optics and Photonics, SPIE, 2024.

[111] F. Marin, A. Rohatgi, and S. Charlot. Webplotdigitizer, a polyvalent and free software to extract spectra from old astronomical publications: application to ultraviolet spectropolarimetry, 2017.